

Ultrafast dynamics of interfacial water

Cho-Shuen Hsieh

© C.-S. Hsieh, 2013

Cover design © Chungwen Liang and Cho-Shuen Hsieh, 2013

ISBN/EAN: 978-90-8891-786-8

Printed by: Proefschriftmaken.nl || Uitgeverij BOXPress

Published by: Uitgeverij BOXPress, 's-Hertogenbosch

A digital version of this thesis is available at www.amolf.nl/publications/theses. Printed copies can be obtained by request to the library at FOM Institute AMOLF, library@amolf.nl.

Ultrafast dynamics of interfacial water

ACADEMISCH PROEFSCHRIFT

ter verkrijging van de graad van doctor
aan de Universiteit van Amsterdam
op gezag van de Rector Magnificus
prof. dr. D. C. van den Boom
ten overstaan van een door het college voor promoties
ingestelde commissie
in het openbaar te verdedigen in de Agnietenkapel
op vrijdag 17 januari 2014 te 14:00 uur

door

Cho-Shuen Hsieh

geboren te Taiwan

Promotiecommissie

Promotor:

Prof. dr. M. Bonn

Overige leden:

Prof. dr. H.J. Bakker

Prof. dr. P. Schall

Prof. dr. A.W. Kleijn

Dr. R.K. Campen

Dr. H. Arnolds

Prof. dr. J.L. Skinner

Prof. dr. M.H.M. Janssen

Faculteit der Natuurwetenschappen, Wiskunde en Informatica



The work described in this thesis was performed at the FOM Institute AMOLF, Science Park 104, 1098 XG Amsterdam, The Netherlands and Department of Molecular Spectroscopy, Max Planck Institute for Polymer Research, 55128 Mainz, Germany. This work is part of the research programme of the Foundation for Fundamental Research on Matter (FOM), which is financially supported by the Netherlands Organisation for Scientific Research (NWO).

Publications covered in this thesis:

C.-S. Hsieh, R. K. Campen, M. Okuno, E. H. G. Backus, Y. Nagata, and M. Bonn, “Mechanism of vibrational energy dissipation of free OH groups at the air–water interface,” *Proceedings of the National Academy of Sciences of the United States of America*, Vol. 110, 18780-18785, 2013.

Y. Nagata, **C.-S. Hsieh**, T. Hasegawa, J. Voll, E. H. G. Backus, and M. Bonn, “Water Bending Mode at the Water–Vapor Interface Probed by Sum-Frequency Generation Spectroscopy: A Combined Molecular Dynamics Simulation and Experimental Study,” *The Journal of Physical Chemistry Letters*, Vol. 4, 1872-1877, 2013.

C.-S. Hsieh, R. K. Campen, A. C. Vila Verde, P. Bolhuis, H.-K. Nienhuys, and M. Bonn, “Ultrafast Reorientation of Dangling OH Groups at the Air-Water Interface Using Femtosecond Vibrational Spectroscopy,” *Physical Review Letters*, Vol. 107, 116102, 2011.

C.-S. Hsieh, H. Bakker, L. Piatkowski, and M. Bonn (Manuscript in preparation) “Extremely strong modulation of time-resolved surface SFG due to thermal shock waves”.

C.-S. Hsieh*, M. Okuno*, J. Hunger, E. H. G. Backus, and M. Bonn (Manuscript in preparation) “Ultrafast vibrational energy transfer of hydrogen-bonded OHs at the air-water interface revealed by two-dimension phase-specific surface vibrational spectroscopy”.

Other publications by the same author:

C.-Y. Ko, M.-Y. Tsai, W.-F. Tseng, C.-H. Cheng, C.-R. Huang, J.-S. Wu, H.-Y. Chung, **C.-S. Hsieh**, C.-K. Sun, S.-P.L. Hwang, C.-H. Yuh, C.-J. Huang, T.-W. Pai, W.-S. Tzou, and C.-H. Hu, “Integration of CNS survival and differentiation by HIF2 α ,” *Cell Death and Differentiation*, Vol.18, 1757-1770, 2011.

C.-S. Hsieh, C.-Y. Ko, S.-Y. Chen, T.-M. Liu, J.-S. Wu, C.-H. Hu, and C.-K. Sun, “In vivo long-term continuous observation of gene expression in zebrafish embryo nerve systems by

using harmonic generation microscopy and morphant technology,” *Journal of Biomedical Optics*, Vol. 13, 064041, 2008.

C.-S. Hsieh, S.-U. Chen, Y.-W. Lee, Y.-S. Yang, and C.-K. Sun, "Higher harmonic generation microscopy of in vitro cultured mammal oocytes and embryos," *Optics Express*, Vol. 16, 11574-11588, 2008.

S.-Y. Chen, **C.-S. Hsieh**, S.-W. Chu, C.-Y. Lin, C.-Y. Ko, Y.-C. Chen, H.-J. Tsai, C.-H. Hu, and C.-K. Sun, “Noninvasive harmonics optical microscopy for long-term observation of embryonic nervous system development in vivo,” *Journal of Biomedical Optics*, Vol. 11, 054022, 2006.

Table of Contents

Chapter 1 Introduction	1
1.1 Interfaces.....	1
1.2 Vibrational Sum-Frequency Generation (SFG) Spectroscopy	3
1.3 Time-Resolved SFG Spectroscopy (TR-SFG).....	8
1.4 Time- and Polarization-Resolved SFG Spectroscopy (TPR-SFG).....	10
1.5 Two-Dimensional Phase-Sensitive SFG Spectroscopy (2D-PS-SFG)	14
1.6 Thesis Outline	18
Chapter 2 Experimental Techniques	19
2.1 Introduction.....	19
2.2 TR-SFG setup	20
2.2.1 One-color experiments.....	20
2.2.2 Two-color experiments	21
2.2.3 SFG generation and detection	22
2.3 Data analysis	25
Chapter 3 Ultrafast Reorientation of Dangling OH Groups at the Air/Water Interface	29
3.1 Introduction.....	29
3.2 Experimental section.....	31
3.3 Simulation Details.....	31
3.3.1 Coordinate system.....	32
3.3.2 Definition of the interface	33
3.4 Results and Discussion	34
3.5 Conclusion	42
Chapter 4 Mechanism of Vibrational Energy Dissipation of Free OH Groups at the Air/Water Interface	43
4.1 Introduction.....	43
4.2 Experimental section.....	48
4.3 Results and discussion	48
4.4 Conclusion	56
Chapter 5 Ultrafast Vibrational Energy Transfer between Hydrogen-bonded OH groups at the Air/Water Interface Revealed by Two-Dimensional Phase-sensitive Surface Vibrational Spectroscopy	57

5.1 Introduction.....	58
5.2 Experimental section.....	60
5.3 Results and discussion	61
5.3.1 Differential $\text{Im}[\chi^{(2)}]$ spectra	61
5.3.2 2D-PS-SFG spectra.....	63
5.3.3 Vibrational relaxation of H-bonded OH groups	65
5.4 Conclusion	68
Chapter 6 Probing the Generation and Propagation of Shock Waves at the Air/Liquid Interface Using Sum Frequency Generation Spectroscopy	69
6.1 Introduction.....	69
6.2 Experimental section.....	71
6.3 Results and discussion	71
6.4 Conclusion	77
Bibliography	79
Summary	87
Samenvatting.....	91
Acknowledgement	95

Chapter 1

Introduction

1.1 Interfaces

Interfaces are very familiar to our daily life; the air/water interface covers 70% of our planet, the liquid/solid interface is ubiquitous in, for example, any container holding liquids, and solid/solid interfaces are critical for P/N junctions in semiconductors used in IC chips. Due to the termination of the covalent bonds or the intermolecular forces (such as hydrogen bonds or Van der Waals interactions) of the bulk materials, the structures of these interfaces are modified compared with the bulk structure. The structures of these interfaces are determined by delicate balance between the binding energy of atoms and molecules in the different bulk materials and the entropic and enthalpic contributions to the free energy originating from the presence of the surface. Therefore studying the structure of the interfaces enables us to understand the molecular interaction between two materials. Among the techniques that allow molecular level insights into the interface structures, vibrational spectroscopic approaches have demonstrated to be a key tool to study the orientation of interfacial molecules, the local environment of the molecules, and the intermolecular bonding strength [1,2].

Historically, much effort has been put into trying to elucidate gas/metal and air/semiconductor interfaces, on which many useful catalytic reactions occur such as the water splitting on the titanium oxide interface [3] and the reaction occurring in car exhaust catalysts: $2 \text{CO} + 2 \text{NO} \rightarrow 2 \text{CO}_2 + \text{N}_2$, taking place on the platinum/rhodium surface [4]. From infrared (IR) transient absorption spectroscopy and first-principles calculations, it has been shown that the structural arrangement of the atoms composing the solid surface can change due to chemisorption and/or physisorption of the molecules on the surface, and this rearrangement of the surface structure can lower the activation energy of the transition state, thus driving the catalytic reactions [5–7]. These effects can be explained solely in terms of the enthalpic contributions to the free energy, because the decrease in the entropy due to the chemi/physi-sorption of the molecule onto the solid surface is negligible for the solid surface.

In contrast to the gas/solid interface, for soft interfaces such as gas/liquid and liquid/liquid interfaces, the decrease in entropy at the interface contributes significantly, sometimes even dominating the free energy contributions. For instance, the ensemble average of the molecular orientation is zero (i.e. isotropic) in the bulk of most liquids, while from the

bulk liquid to the vapor or solid regions the density of liquid molecules decreases continuously and the preferential orientation of molecules near the interfaces can minimize the entropy increase compared with the bulk material. This gives rise to the non-centrosymmetric orientation of the liquid molecules near the solid/liquid or gas/liquid interfaces. The challenge is to probe this non-centrosymmetric structure with a noninvasive technique.

Even-order optical techniques are very suitable to noninvasively probe the liquid interface, because the even-order optical response is finite only for non-centrosymmetric systems, or non-centrosymmetric regions of the system such as a surface. Among them, sum-frequency generation (SFG) spectroscopy has been widely used, because of its capability to probe the molecular response selectively at the interface through the vibrational states of interfacial molecules [8]. For instance, the water OH stretching mode frequency shifts due to variations of the hydrogen bond strength, indicating that this mode can be used as a reporter for the microscopic structures around the water molecules. With SFG, the vibrational spectrum of specifically the interfacial water molecules can be recorded. Thus, this SFG technique has been important in gaining microscopic insights of the molecular structure of aqueous interfaces [8,9]. In recent years, this technique has further been proven very useful for investigating protein structures at the lipid/water interface [10,11] as well as probing chemical reactions [12]. Probably, one of the most interesting insights obtained using SFG is that at the conceptually simple air/water interface, a significant fraction of water molecules has an OH bond pointing up toward the air [13].

The static picture of the interfaces such as that of the water air interface, with water OH groups pointing up or down, originates from the time-averaging of the fluctuations of the interfacial structures of water. These interfacial structures vary due to the ultrafast dynamics of the liquid molecules such as the librational and rotational motion occurring on picosecond and femtosecond timescales, which may differ from that in the bulk. Thus, the time averaged picture of water is insufficient for a true understanding of the surface; understanding the structural and energetic dynamics of interfacial molecules is required. For example, although the water molecules are expected to be mobile even at the air/water interface, a challenge is to address the extent to which the water dynamics at the interfaces are faster or slower compared with the bulk water dynamics. To be able to follow, in real time, the motions of molecules at the surface would greatly help to understand that surface.

Pump-probe techniques have been used mainly in bulk systems to experimentally investigate molecular dynamics [14–16], and elucidate contributions of the homogeneous broadening and inhomogeneous broadening to the vibrational spectra. To selectively probe the interfacial molecules and track their ultrafast dynamics, SFG spectroscopy needs to be combined with pump probe techniques. This can be achieved by using the fourth-order optical technique, in which the fourth-order signal is generated by the IR pump and IR + visible probe pulses. This technique allows us to follow the structural dynamics of interfacial molecules, distinguish different contributions to SFG vibrational line shapes, and elucidate the mechanism and rate of interfacial vibrational energy relaxation.

In this thesis, we focus on one of the simplest and ubiquitous, yet arguably most interesting liquid interfaces: the aqueous interface with air. Since the air/water interface is composed of only water-water interactions, this interface is ideal to highlight the interfacial water interactions and study the structure and dynamics of interfacial water with interruption of the hydrogen bonds. A big puzzle is how mobile these water molecules are and how the dynamics of water can be connected with the interfacial water structure, and the macroscopic properties of the interface. Hereafter, we will reveal the structure and dynamics of interfacial water molecules using SFG and extended SFG techniques to give a complete microscopic picture of the air/water interface.

1.2 Vibrational Sum-Frequency Generation (SFG) Spectroscopy

The section introduces some basic concepts of the vibrational SFG spectroscopy technique and its surface specificity. Vibrational SFG spectroscopy is a nonlinear optical technique. The response of a material to an incident optical field is nonlinear, when the optical properties of the material are being modified as a result of the strength of the optical field. This happens when the response of the material to the electromagnetic field is no longer simply proportional to the field, but depends in a nonlinear manner on the strength of the field. By detecting this response, we can understand how the optical electrical field interacts with the material, which in turn is determined by the physical properties of the material such as the structure and the binding strength. Specifically, vibrational SFG spectroscopy can be used to study the properties of the few top most layers of the interfacial molecules. In the following, I will describe how the SFG field is generated from the surface.

In conventional (i.e. linear) optics, the induced polarization ($\vec{P}(\vec{r}, t)$) of a material system depends linearly on the externally applied electrical field strength ($\vec{E}(\vec{r}, t)$):

$$\vec{P}(\vec{r}, t) = \vec{P}^{(1)}(\vec{r}, t) = \varepsilon_0 \chi^{(1)} \vec{E}(\vec{r}, t) \quad (1.1)$$

where the constant of proportionality, $\chi^{(1)}$, is known as the linear susceptibility and ε_0 is the permittivity of vacuum. Microscopically, the field $\vec{E}(\vec{r}, t)$ acts upon dipoles in the material, causing them to oscillate. The collective oscillation of individual dipoles gives rise to the macroscopic polarization $\vec{P}(\vec{r}, t)$. In the regime of linear response, the induced polarization is proportional to the externally applied field. However, for sufficiently strong electric fields, the nonlinear responses of the material can contribute significantly to the polarization. These effects can be taken into account by expanding the polarization $\vec{P}(\vec{r}, t)$ as a power series in $\vec{E}(\vec{r}, t)$:

$$\begin{aligned} \vec{P}(\vec{r}, t) &= \varepsilon_0 [\chi^{(1)} \vec{E}(\vec{r}, t) + \chi^{(2)} \vec{E}^2(\vec{r}, t) + \chi^{(3)} \vec{E}^3(\vec{r}, t) + \dots] \\ &\equiv \vec{P}^{(1)}(\vec{r}, t) + \vec{P}^{(2)}(\vec{r}, t) + \vec{P}^{(3)}(\vec{r}, t) + \dots \equiv \vec{P}^{(1)}(\vec{r}, t) + \vec{P}^{NL}(\vec{r}, t) \end{aligned} \quad (1.2)$$

where $\chi^{(n)}$ denotes the n^{th} -order nonlinear susceptibility, and $\vec{P}^{(n)}(\vec{r}, t)$ denotes the n^{th} -order nonlinear polarization.

The polarization induced by the external field, in turn, serves as a source term for the emission of radiation. The manner in which the induced polarization in the material generates new electrical fields is described by the Maxwell equations, which enables us to understand the optical response of the material due to the irradiation of the incoming fields. Here, we consider a material with no free charges and currents and assume that it is nonmagnetic. Then, the Maxwell equations read:

$$\nabla \cdot \vec{D} = 0 \quad (1.3)$$

$$\nabla \cdot \vec{B} = 0 \quad (1.4)$$

$$\nabla \times \vec{E} = -\frac{\partial \vec{B}}{\partial t} \quad (1.5)$$

$$\nabla \times \frac{\vec{B}}{\mu_0} = \frac{\partial \vec{D}}{\partial t} \quad (1.6)$$

where μ_0 is the permeability of free space, \vec{B} is the magnetic field, and \vec{D} is the dielectric displacement and can be expressed as:

$$\vec{D}(\vec{r}, t) = \varepsilon_0 \vec{E}(\vec{r}, t) + \vec{P}(\vec{r}, t) \quad (1.7)$$

By taking the curl of Eq. (1.5), replacing $\nabla \times \vec{B}$ with Eq. (1.6), \vec{D} with Eq. (1.7), and μ_0 by $1/\varepsilon_0 c^2$ we obtain:

$$\nabla \times \nabla \times \vec{E}' + \frac{1}{c^2} \frac{\partial^2}{\partial t^2} \vec{E}' = -\frac{1}{\varepsilon_0 c^2} \frac{\partial^2}{\partial t^2} \vec{P} \quad (1.8)$$

which is the most general form for retrieving the optical electric field (\vec{E}') generated by the induced polarization in a material, independent of whether the polarization is linear or nonlinear. Note here that the optical field generated from the material (\vec{E}') is different from the optical field applied to the material (\vec{E} in Eq. (1.1)). The induced polarization $\vec{P}(\vec{r}, t)$ can be split into linear and nonlinear terms as shown in Eq. (1.2). As the SFG light per definition originates from the nonlinear polarization, we only have to consider that part of the wave equation containing the induced nonlinear response of the medium acting as a source term, which can be expressed as:

$$\nabla \times \nabla \times \vec{E}' + \frac{1}{c^2} \frac{\partial^2}{\partial t^2} \vec{E}' = -\frac{1}{\varepsilon_0 c^2} \frac{\partial^2}{\partial t^2} \vec{P}^{NL} \quad (1.9)$$

In our second-order SFG experiments, the polarization generated by the incident electric fields holds a frequency which is the sum of the two applied fields, the fixed near-infrared (VIS, $\lambda_{VIS} \sim 800$ nm) and tunable mid-infrared (IR, $\lambda_{IR} \sim 3000$ nm) beams. To simplify the discussion, we assume that the electric field which contains two frequencies ω_{VIS} and ω_{IR} propagates in the same direction \hat{e} , where $\vec{E}(\vec{r}, t) = E(t)\hat{e}$. So $E(t)$ can be expressed as:

$$E(t) = \frac{1}{2} (E_{VIS} e^{-i\omega_{VIS} t} + E_{IR} e^{-i\omega_{IR} t} + c.c.) \quad (1.10)$$

The second-order contribution to the nonlinear polarization is of the form:

$$P^{(2)}(t) = \varepsilon_0 \chi^{(2)} E^2(t) \quad (1.11)$$

which leads to:

$$P^{(2)}(t) = \frac{1}{2} \varepsilon_0 \chi^{(2)} [E_{VIS}^2 e^{-2i\omega_{VIS} t} + E_{IR}^2 e^{-2i\omega_{IR} t} + 2E_{VIS} E_{IR} e^{-i(\omega_{VIS} + \omega_{IR})t} + 2E_{VIS} E_{IR}^* e^{-i(\omega_{VIS} - \omega_{IR})t} + E_{VIS} E_{VIS}^* + E_{IR} E_{IR}^* + c.c.] \quad (1.12)$$

The sum-frequency response is thus given by :

$$P_{\omega_{SFG}=\omega_{VIS}+\omega_{IR}}^{(2)}(t) = \varepsilon_0 \chi^{(2)} E_{VIS} E_{IR} e^{-i(\omega_{VIS}+\omega_{IR})t} + c.c. \quad (1.13)$$

In our experiments, the vibrational SFG signal is generated at a visible frequency ($\lambda_{\text{SFG}} \sim 630$ nm). Normally in a SFG experiment the VIS and IR beams are not co-linear but overlap on the sample surface temporally and spatially, i.e.,

$$\vec{E}(\vec{r}, t) = \frac{1}{2} (\vec{E}_{\text{VIS}} e^{-i(\omega_{\text{VIS}} t - \vec{k}_{\text{VIS}} \vec{r})} + \vec{E}_{\text{IR}} e^{-i(\omega_{\text{IR}} t - \vec{k}_{\text{IR}} \vec{r})} + c.c.) \quad (1.14)$$

where \vec{k}_{VIS} and \vec{k}_{IR} are the wavevectors of the VIS and IR beams, respectively. The sum-frequency response reads:

$$\vec{P}_{\text{SFG}}^{(2)}(\vec{r}, t) = \varepsilon_0 \chi^{(2)} \vec{E}_{\text{VIS}} \vec{E}_{\text{IR}} e^{-i[(\omega_{\text{VIS}} + \omega_{\text{IR}})t - (\vec{k}_{\text{VIS}} + \vec{k}_{\text{IR}}) \vec{r}]} + c.c. \quad (1.15)$$

where $\vec{k}_{\text{SFG}} = \vec{k}_{\text{VIS}} + \vec{k}_{\text{IR}}$ is the phase matching condition. For the SFG process, $\hbar\omega_{\text{SFG}} = \hbar\omega_{\text{VIS}} + \hbar\omega_{\text{IR}}$ and $\hbar\vec{k}_{\text{SFG}} = \hbar\vec{k}_{\text{VIS}} + \hbar\vec{k}_{\text{IR}}$, which indicate that both energy and momentum are conserved during the SFG process. Since $\vec{P}_{\text{SFG}}^{(2)}$, \vec{E}_{VIS} , and \vec{E}_{IR} are vectors in three dimensions, $\chi^{(2)}$ is a $3 \times 3 \times 3$ tensor with 27 elements. $\vec{P}_{\text{SFG}}^{(2)}$ in the Cartesian coordinates of the lab frame is given by

$$P_{i,\text{SFG}}^{(2)} = \varepsilon_0 \chi_{ijk}^{(2)} E_{j,\text{VIS}} E_{k,\text{IR}} \quad (1.16)$$

where i, j , and k denote the indices that correspond to the Cartesian coordinates x, y , and z . Equation (1.16) shows that the incident VIS electrical field in the j^{th} direction and the IR field in the k^{th} direction induce the polarization of SFG in the i^{th} direction in the material. For materials that possess inversion symmetry, $\chi_{ijk}^{(2)} = \chi_{-i-j-k}^{(2)} = -\chi_{ijk}^{(2)}$ [17], which proves that the second-order susceptibility $\chi_{ijk}^{(2)} = 0$ for any system that possesses inversion symmetry. The orientation of molecules in the bulk of liquids is generally randomized, which means that $\chi_{ijk}^{(2)} = 0$ for such a bulk liquid and that it does not contribute to the SFG response. On the other hand, at the surface the inversion symmetry is broken, making the response of interfacial molecules SFG-active. Therefore the SFG signals generated at the liquid interface mainly originate from the interfacial molecules and hardly contain contributions from the bulk molecules.

The non-zero elements of $\chi_{ijk}^{(2)}$ contain information on the macroscopic orientation of the interfacial molecules. In this thesis, we mainly focus on the air/water interface (Fig. 1.1), which holds $C_{\infty v}$ symmetry. This symmetry leads to only four distinct different non-zero sets among the 27 elements: $\chi_{zxx}^{(2)} = \chi_{zyy}^{(2)}, \chi_{xzx}^{(2)} = \chi_{yzy}^{(2)}, \chi_{xxz}^{(2)} = \chi_{yyz}^{(2)}, \chi_{zzz}^{(2)}$ [18], where the z -axis is

parallel to the surface normal and the xy -plane is parallel to the surface. With different polarizations of the incident VIS and IR beams, the magnitudes of these elements can be determined. For the air/water interface, the polarization combination of ssp (SFG, VIS, IR) is used throughout the thesis since it contains the contribution solely from $\chi_{xxz}^{(2)}$ ($\chi_{xy}^{(2)} = 0$), which is larger than $\chi_{zxx}^{(2)}$ and $\chi_{xzx}^{(2)}$ at the air/water interface. Note that although the contribution of $\chi_{zzz}^{(2)}$ is contained in the SFG signal of the ppp polarization, the ppp -SFG signal also contains the contribution from $\chi_{zxx}^{(2)}$, $\chi_{xzx}^{(2)}$, and $\chi_{xxz}^{(2)}$, which complicates the analysis of the spectra [18].

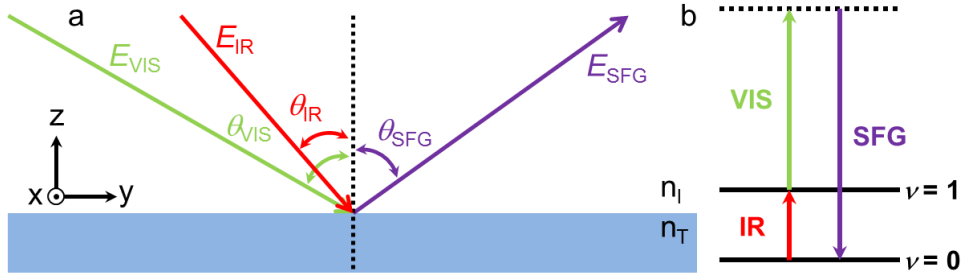


Fig. 1.1 (a) Geometry of the SFG experiment for the air/water interface. The incident angles of the VIS and IR beams are θ_{VIS} and θ_{IR} , respectively. The reflective angle of the SFG beam is θ_{SFG} . The z axis of the lab coordinates is along the surface normal. (b) The energy level diagram. The IR frequency is resonant with the $0 \rightarrow 1$ transition and the VIS upconverts the $0 \rightarrow 1$ transition to generate SFG signal.

According to Eqs. (1.9b) and (1.13), under the electric-dipole approximation, the SFG signal generated at the air/water interface I_{SFG} is: [19]

$$I_{SFG} = \frac{8\pi^3 \omega_{SFG}^2 \sec^2 \theta_{SFG}}{c^3 n_I(\omega_{SFG}) n_I(\omega_{VIS}) n_I(\omega_{IR})} |\chi^{(2)}|^2 I_{VIS} I_{IR} \quad (1.17)$$

where $n_I(\omega_i)$ is the refractive index of the incident medium at frequency ω_i . I_{VIS} and I_{IR} are the intensities of the VIS and IR beams. In SFG spectroscopy, the SFG intensity is recorded as a function of frequency to map out interfacial vibrational resonances and, accordingly, $\chi^{(2)}$ can be expressed as a function of ω_{IR} [20]:

$$\chi^{(2)} = A_{NR} e^{i\phi_{NR}} + \sum_n \frac{A_n}{\omega_{IR} - \omega_n + i\Gamma_n} \quad (1.18)$$

where A_{NR} is the amplitude of the non-resonant susceptibility, ϕ_{NR} is its phase, A_n is the amplitude of the n^{th} vibrational mode with the resonant frequency ω_n , and Γ_n is the

linewidth of the transition. One can see from Eq. (1.18) that $\chi^{(2)}$ is enhanced when the IR frequency is resonant with the vibrational modes (Fig. 1.1b), i.e., $\omega_{IR} = \omega_n$.

The macroscopic SFG susceptibility $\chi^{(2)}$ of a sample is related to the interfacial molecular structure through the third-rank molecular hyperpolarizability tensor β with the relation:

$$\chi^{(2)} = N_S \langle \beta \rangle \quad (1.19)$$

where N_S is the surface density of molecules and $\langle \dots \rangle$ denotes the thermal averaging over the molecules. Analogous to $\chi^{(2)}$, the molecular hyperpolarizability can be written as a sum of a nonresonant and a resonant term:

$$\beta = a_{NR} e^{i\phi_{NR}} + \sum_n \frac{a_n}{\omega_{IR} - \omega_n + i\Gamma_n} \quad (1.20)$$

where the microscopic amplitude a_n is related to A_n in the slow motion limit [21] by:

$$A_{n,ijk} = N_S \sum_{opq} \langle (\hat{i} \cdot \hat{o})(\hat{j} \cdot \hat{p})(\hat{k} \cdot \hat{q}) \rangle a_{n,opq} \quad (1.21)$$

$(\hat{i}, \hat{j}, \hat{k})$ is the unit vector in the lab frame and $(\hat{o}, \hat{p}, \hat{q})$ are the unit vector in the molecular frame. Equation (1.21) connects the thermal average of the molecular orientations with the macroscopic SFG signals.

1.3 Time-Resolved SFG Spectroscopy (TR-SFG)

Conventional SFG spectroscopy provides us with one-dimensional spectra, where the dynamical information of structure changing and energy coupling is contained in the resonant frequency (ω) and the linewidth (Γ) in Eq. (1.20). Barring inhomogeneous broadening resulting from different oscillators having different vibrational frequencies, Γ is related to the decay rate ($1/T_2$) of the macroscopic polarization (induced by the IR pulse), $2\pi\Gamma = 1/T_2$, where T_2 is the homogeneous dephasing time. The decaying of the macroscopic polarization can be caused by two reasons: (i) the amplitude decay of the polarization of each individual molecule and (ii) the polarization of different molecules will run out of phase and no longer interfere constructively after a certain amount of time. Therefore this homogenous dephasing time can be decomposed into two contributions, $1/T_2 = 1/(2T_1) + 1/T_2^*$, where T_1 is the population lifetime and T_2^* is the pure dephasing time. These two time constants correspond to the decay of the polarization cause by the reason (i) and (ii). Since it is impossible to

separately estimate the contributions of the vibrational energy relaxation and the pure-dephasing processes from the one-dimensional SFG spectra, we extract the vibrational energy relaxation rates of the interfacial molecules combining SFG spectroscopy with time-resolved techniques [22–24]. In this section, the basic principles of time-resolved SFG spectroscopy are briefly introduced.

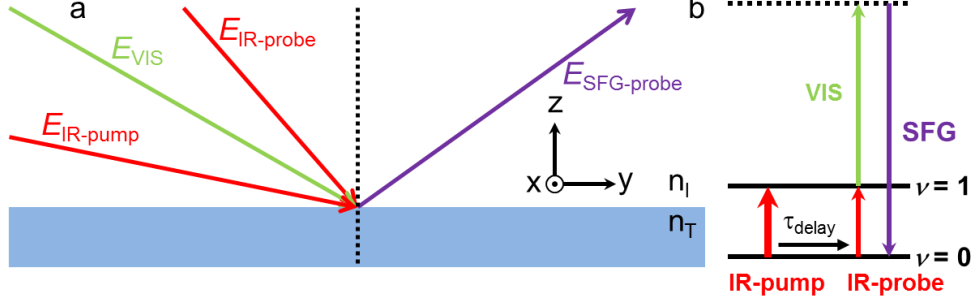


Fig. 1.2 (a) Geometry of the TR-SFG experiment for the air/water interface. The z axis of the lab coordinates is along the surface normal. (b) Energy level diagram of the TR-SFG experiment. The intense IR-pump pulse excites the vibrations from the ground state to the first excited state. The probe pulse pair which generates the SFG signal scans in time τ_{delay} respect to the pump pulse. The evolution of the system can be monitored by the modulation of the SFG signal.

The experimental geometry and energy diagram of time-resolved SFG spectroscopy (TR-SFG) are shown in Fig. 1.2. The information on the population densities of the ground state and excited states is contained in the time-dependent fourth-order signal. As seen in Eqs. (1.17) and (1.19), the SFG intensity is proportional to the square of the population difference of the ground state ($N_0(t)$) and the excited state ($N_1(t)$) of the interfacial molecules $I_{SFG} \propto [N_0(t) - N_1(t)]^2$, where t denotes the time interval between the pumping and probing pulses. $t = 0$ means that the pump and probe pulses overlap with each other. Before the system is subject to the pump pulse ($t \ll 0$), $N_0(t \ll 0) = N_0$, since $\hbar\omega \gg k_B T$ at room temperature, where ω is the $0 \rightarrow 1$ transition frequency of the vibrational states ($\sim 3300 \text{ cm}^{-1}$), and the thermal excitation of the vibrational excited state is therefore negligible ($N_1(t \ll 0) \sim 0$). By exciting the vibrations with the intense pump pulses, part of the ground state population (ΔN) is transferred to the first excited state, leading to a ground state population of $N_0 - \Delta N$ and an excited state population of ΔN . Due to the anharmonicity of the OH stretching mode, the $1 \rightarrow 2$ transition is $\sim 250 \text{ cm}^{-1}$ lower than the $0 \rightarrow 1$ transition [25]. So if the probe frequency is resonant with the $0 \rightarrow 1$ transition, the corresponding SFG signal ($0 \rightarrow 1$) becomes:

$$I_{SFG}^{0 \rightarrow 1} \propto [N_0(t) - N_1(t)]^2 = (N_0 - 2\Delta N)^2 = (N_0)^2 - 4N_0\Delta N + 4(\Delta N)^2 \quad (1.22a)$$

If the probe frequency is resonant with the 1 \rightarrow 2 transition, and realizing that $N_2(t) \sim 0$ for all times t , the corresponding SFG signal (1 \rightarrow 2) becomes:

$$I_{SFG}^{1 \rightarrow 2} \propto [N_1(t) - N_2(t)]^2 = (\Delta N)^2 \quad (1.22b)$$

The population difference induced by the pump pulse is typically 5-10% of N_0 with our experimental geometry, so the third term of Eq. (1.22a), which is the quadratic term in ΔN , can be neglected. The pump-probe TR-SFG signal of the 0 \rightarrow 1 transition, normalized to the steady-state signal, can then be approximated as:

$$I_{SFG}^{N(0 \rightarrow 1)} \propto (N_0 - \Delta N)^2 / (N_0)^2 \sim 1 - 4\Delta N / N_0 \quad (1.23)$$

If the pump pulses excites 10% of the ground state molecules to the excited state at $t = 0$, the SFG signal of the 0 \rightarrow 1 transition is then reduced to $(0.8)^2 = 0.64$ times the original signal, which leads to a reduction of the signal of 36%. This bleach will decay, reflecting the vibrational relaxation of the excited chromophore with its lifetime T_1 , which is a significant indicator of structural and energetic dynamics of the molecules.

1.4 Time- and Polarization-Resolved SFG Spectroscopy (TPR-SFG)

In section 1.3 we described the surface-specific vibrational technique to monitor vibrational energy relaxation. To understand the reorientation of the interfacial molecules, polarization-resolved experiments should be performed. Since the IR-probe pulses are p -polarized in our experiments, if the pump pulses are p - (s -) polarized, which is parallel (perpendicular) to the probe, the excited OH stretching modes will rotate out of (into) our probing window, leading to a faster (slower) recovery of the SFG signal. Therefore, if the rate of the reorientational motion is comparable with the vibrational relaxation of the molecule, the recovery of the bleach of the signal stems from both mechanisms.

Here we introduce time- and polarization-resolved SFG spectroscopy (TPR-SFG) to extract the reorientational motion of the molecules by changing the polarization of the pump pulse with respect to the probe pulse [26]. The experimental geometry of a TPR-SFG spectroscopy is depicted in Fig. 1.3. In the following, I will follow the formalism as described in reference [27].

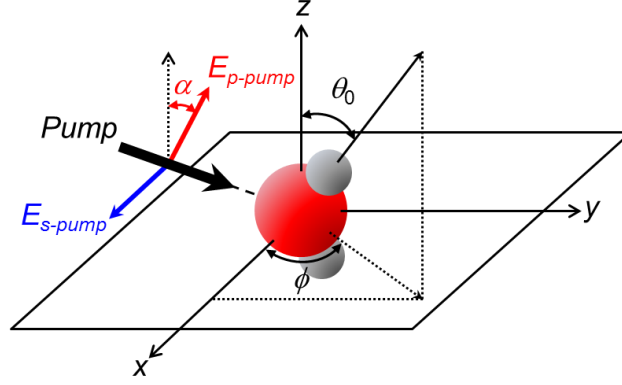


Fig. 1.3 Geometry of the TPR-SFG experiment for the air/water interface. The dipole of the OH points at an angle θ_0 related to the surface normal (z). The orientational distribution of the ensemble is invariant under rotations (ϕ) around the surface normal (in-plane reorientation). α is the angle of the electric field of the p -polarized pump pulse with respect to the surface normal.

Here we consider the optical response of the s - and p -pumped pulses [27]. Assume that the molecules have an orientation distribution $\rho(\phi)$ along the azimuthal angle ϕ . The reorientation of this distribution follows the diffusion equation:

$$\frac{\partial}{\partial t} \rho(\phi, t) = D \frac{\partial^2 \rho(\phi, t)}{\partial^2 \phi} \quad (1.24)$$

where D is the in-plane rotational diffusion constant for the molecules in units of (rad^2/s). The generic solution for Eq. (1.24) reads:

$$\rho(\phi, t) = a_0 + \sum_{m \geq 1} [a_m \cos(m\phi) + b_m \sin(m\phi)] e^{-m^2 D t} \quad (1.25)$$

where a_0 , $\cos(m\phi)$, and $\sin(m\phi)$ are eigenfunctions of Eq. (1.24). In the experiment, the pump pulses with different polarizations create an anisotropic population, because the probability of the molecules excited by the electric field is proportional to $|\vec{\mu} \cdot \vec{E}|^2$. The unit factor of the transition dipole $\vec{\mu} = (\mu_x, \mu_y, \mu_z) = (\cos\phi \sin\theta_0, \sin\phi \sin\theta_0, \cos\theta_0)$, where θ_0 is the angle of the vibrational dipole moment of the molecules with respect to the surface normal. The unit factor of the excited electrical fields are $\vec{E}_s = E_s(1, 0, 0)$ and $\vec{E}_p = E_p(0, \sin\alpha, \cos\alpha)$, where α is the angle of the electric field of the p -polarized pump pulse with respect to the surface normal. The excitation efficiencies for the s - and p -polarized pump pulses are:

$$|\vec{\mu} \cdot \vec{E}_s|^2 = (E_s \cos\phi \sin\theta_0)^2 = \frac{1}{2} I_s \sin^2 \theta_0 (1 + \cos 2\phi) \quad (1.26)$$

$$\begin{aligned}
|\vec{\mu} \cdot \vec{E}_p|^2 &= E_p^2 (\sin \phi \sin \theta_0 \sin \alpha + \cos \theta_0 \cos \alpha)^2 \\
&= I_p \left[\frac{1}{2} \sin^2 \theta_0 \sin^2 \alpha + \cos^2 \theta_0 \cos^2 \alpha \right. \\
&\quad \left. + \left(\frac{1}{2} \sin 2\theta_0 \sin 2\alpha \right) \sin \phi + \left(-\frac{1}{2} \sin^2 \theta_0 \sin^2 \alpha \right) \cos 2\phi \right]
\end{aligned} \tag{1.27}$$

Therefore with the initial conditions,

$$\begin{aligned}
\rho_s(\phi, 0) &= \rho_{s0} \\
\rho_p(\phi, 0) &= \rho_{p0}
\end{aligned} \tag{1.28}$$

where ρ_{s0} and ρ_{p0} are proportional to I_s and I_p , respectively, the time-dependent population distributions of the excited molecules following an s - and p -polarized pump are:

$$\begin{aligned}
\rho_s(\phi, t) &= A_s [1 + \cos(2\phi) e^{-4Dt}] \\
\rho_p(\phi, t) &= A_{p0} + A_{p1} \sin \phi e^{-Dt} + A_{p2} \cos(2\phi) e^{-4Dt}
\end{aligned} \tag{1.29}$$

where

$$\begin{aligned}
A_s &= \frac{1}{2} \rho_{s0} \sin^2 \theta_0 \\
A_{p0} &= \rho_{p0} \left(\frac{1}{2} \sin^2 \theta_0 \sin^2 \alpha + \cos^2 \theta_0 \cos^2 \alpha \right) \\
A_{p1} &= \frac{1}{2} \rho_{p0} \sin 2\theta_0 \sin 2\alpha \\
A_{p2} &= -\frac{1}{2} \rho_{p0} \sin^2 \theta_0 \sin^2 \alpha
\end{aligned} \tag{1.30}$$

Here, we focus on the reorientational dynamics; the vibrational relaxation effect is not included. Incorporating vibrational relaxation simply means that all population distributions are multiplied by a factor of $\exp(-t/T_1)$, where T_1 is the lifetime of the vibrations of the molecules. Equation (1.29) shows that the linearly polarized pump pulses excite the population with the angular distributions having a limited number of eigenfunctions of the diffusion equation with a corresponding small number of decay time constants, which is illustrated in Fig. 1.4, with parameters ($\alpha, \theta_0, \rho_{s0}$, and ρ_{p0}) relevant to the experiment performed in Chapter 3.

For Eq. (1.28), the initial states ρ_{s0} and ρ_{p0} are proportional to the incident pump intensities I_s and I_p . At the interface, the intensity of the local electrical field can be derived as follows. The electric field of every electromagnetic wave incident on a planar surface (\vec{E})

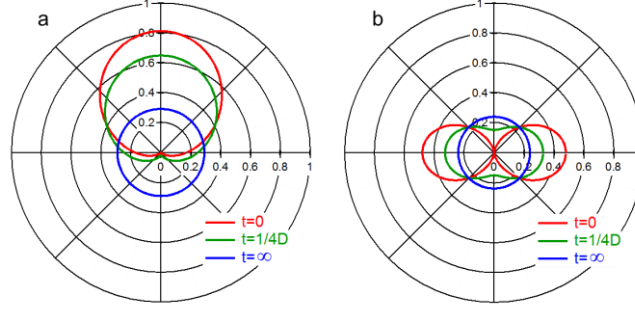


Fig. 1.4 Orientation distribution of a subensemble of molecules that are excited by the pump pulse [27]. (a) Orientation distribution after p -polarized excitation at $t = 0$ (red), $t = 1/(4D)$ (green), $t = \infty$ (blue), where D is the rotational diffusion constant. (b) Orientation distribution after s -polarized excitation. Note that, as time progresses, the initially anisotropic distribution becomes isotropic as a result of diffusional motion. This model is calculated based on reference [27].

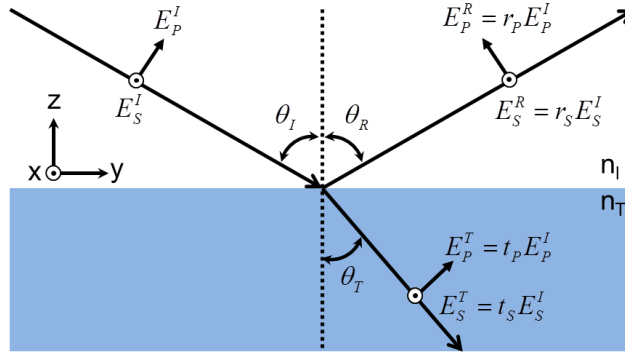


Fig. 1.5 The geometry of incident, reflected, and transmitted beams for s - and p -polarized light at the interface.

can be decomposed into two components, which are parallel (E_p^I) and perpendicular (E_s^I) to the plane of incidence, which is schematically shown in Fig. 1.5. The surface based x , y , and z components of the incident optical field are given by:

$$\vec{E}_x^I = E_s^I \hat{x} \quad (1.31a)$$

$$\vec{E}_y^I = E_p^I \cos \theta_I \hat{y} \quad (1.31b)$$

$$\vec{E}_z^I = E_p^I \sin \theta_I \hat{z} \quad (1.31c)$$

where θ_I is the angle of incidence. The Fresnel amplitude coefficients for reflection are then given by:

$$r_s = \frac{E_s^R}{E_s^I} = \frac{n_I \cos \theta_I - n_T \cos \theta_T}{n_I \cos \theta_I + n_T \cos \theta_T} \quad (1.32a)$$

$$r_p = \frac{E_p^R}{E_p^I} = \frac{n_T \cos\theta_I - n_I \cos\theta_T}{n_T \cos\theta_I + n_I \cos\theta_T} \quad (1.32b)$$

where E_S^R and E_p^R are the reflective \vec{E} fields for s and p polarized light, n_T is the refractive index of the material, and θ_T is angle of the transmission beam, respectively. θ_T follows the relation $n_I \sin\theta_I = n_T \sin\theta_T$. The magnitudes of the interfacial electric field components are therefore:

$$E_x = E_x^I + E_x^R = E_x^I + r_s E_x^I = E_S^I + r_s E_S^I \quad (1.33a)$$

$$E_y = E_y^I + E_y^R = E_y^I + r_p E_y^I = E_p^I \cos\theta_I - r_p E_p^I \cos\theta_I \quad (1.33b)$$

$$E_z = E_z^I + E_z^R = E_z^I + r_p E_z^I = E_p^I \sin\theta_I + r_p E_p^I \sin\theta_I \quad (1.33c)$$

The total intensities of the electric field present in the interfacial region for s and p polarized light are:

$$I_s = E_x^2 = (1+r_s)^2 (E_S^I)^2 = (1+r_s)^2 I_S^I \quad (1.34a)$$

$$\begin{aligned} I_p &= E_y^2 + E_z^2 = [(1-r_p)^2 \cos^2\theta_I + (1+r_p)^2 \sin^2\theta_I] (E_p^I)^2 \\ &= (1+r_p^2 - 2r_p \cos 2\theta_I) I_p^I \end{aligned} \quad (1.34b)$$

From Eq (1.29), by integrating ϕ from 0 to 2π , we can see that at $t = 0$, the total populations excited by the pump pulses are $\rho_s(t=0) = A_s$ and $\rho_p(t=0) = A_{p0}$. By using our experimental geometry, where $\alpha = 34^\circ$, $\theta_0 = 59^\circ$, $\rho_{s0}/\rho_{p0} = I_s/I_p = 0.67$, we obtain $\rho_s(t=0)/\rho_p(t=0) = A_s/A_{p0} = 0.82$, indicating that population excited by the p -polarized pump is larger than that excited by the s -polarized pump, given this geometry. The different amounts and distributions of the molecular populations excited by different polarized pump pulses (Fig. 1.4) result in different depths of modulation and recovery time of the TR-SFG signals, which will be further discussed in chapter 3.

1.5 Two-Dimensional Phase-Sensitive SFG Spectroscopy (2D-PS-SFG)

Although the conventional TR-SFG [24,28–30] is suitable for measuring the vibrational relaxation of molecules vibrating at a certain frequency as described in section 1.3, the coupling between modes with different frequencies cannot be revealed. Two-dimensional techniques, where one specific vibrational mode is excited with a narrow band pump pulse while the responses of other modes are detected with a broad band probe pulse, can be used to understand the coupling between modes. Therefore, 2D-SFG [31–33] has been carried out

to study the mode coupling of interfacial molecules. However, it is very difficult to use 2D-SFG to probe the 1→2 transition response and the peak position and lineshape are distorted, which will be discussed below. The two-dimensional phase-sensitive SFG spectroscopy (2D-PS-SFG) is able to overcome these difficulties. The first 2D-PS-SFG experiment was reported by Zanni and coworkers [34], and subsequently Tahara and coworkers conducted the 2D-PS-SFG experiment at the air/water interface with a positively charged surfactant [35]. In this section, I will present the basic principles of 2D-PS-SFG.

To simplify the discussion, here we neglect the Fresnel factors. The second-order electric field generated in an SFG process at the surface is given by:

$$E^{(2)}(\omega_{SFG}) \propto P^{(2)}(\omega_{SFG}) = \varepsilon_0 \chi^{(2)} E(\omega_{VIS}) E(\omega_{IR}) \quad (1.35)$$

while the fourth-order electric field modulated by the IR pump pulses in a 2D pump-probe SFG experiment is given by:

$$\begin{aligned} E^{(4)}(\omega_{SFG}) &\propto P^{(4)}(\omega_{SFG}) \\ &= \varepsilon_0 \chi^{(4)} E(\omega_{IR-pump}) E^*(\omega_{IR-pump}) E(\omega_{VIS}) E(\omega_{IR-probe}) \end{aligned} \quad (1.36)$$

The SFG intensity probed in a 2D pump-probe SFG experiment is thus

$$\begin{aligned} I_{2D-SFG} &= |E_{2D-SFG}(\omega_{SFG})|^2 = |E_{sample}^{(2)}(\omega_{SFG}) + E_{sample}^{(4)}(\omega_{SFG})|^2 \\ &= |E_{sample}^{(2)}(\omega_{SFG})|^2 + |E_{sample}^{(4)}(\omega_{SFG})|^2 + 2\text{Re}[E_{sample}^{(2)}(\omega_{SFG}) E_{sample}^{(4)*}(\omega_{SFG})] \end{aligned} \quad (1.37)$$

Since $|E_{sample}^{(2)}(\omega_{SFG})| \gg |E_{sample}^{(4)}(\omega_{SFG})|$, the second term, which is the quadratic term of $E_{sample}^{(4)}(\omega_{SFG})$, can be neglected. Therefore, the differential 2D-SFG signal with and without the excitation of the pump pulse is:

$$\Delta I_{2D-SFG} = I_{2D-SFG} - |E_{sample}^{(2)}(\omega_{SFG})|^2 = 2\text{Re}[E_{sample}^{(2)}(\omega_{SFG}) E_{sample}^{(4)*}(\omega_{SFG})] \quad (1.38)$$

which can be recast as:

$$\Delta I_{2D-SFG} \propto \text{Re} \chi_{sample}^{(2)} \text{Re} \chi_{sample}^{(4)*} + \text{Im} \chi_{sample}^{(2)} \text{Im} \chi_{sample}^{(4)*} \quad (1.39)$$

Eq. (1.39) shows that the conventional 2D-SFG intensity ΔI_{2D-SFG} is proportional to the interference between $\chi_{sample}^{(2)}$ and $\chi_{sample}^{(4)}$, therefore it is hard to disentangle the contributions of these two factors. Furthermore, it is very interesting to be able to observe the dynamics of the 1→2 transition response of $\chi_{sample}^{(4)}$. The 1→2 transition frequency is lowered by $\sim 250 \text{ cm}^{-1}$ compared to the 0→1 transition, because of the anharmonic potential of the normal mode. In conventional 2D-SFG, the 1→2 transition response is weak for both $\chi_{sample}^{(2)}$ and

$\chi_{sample}^{(4)}$, leading to a weak ΔI_{2D-SFG} signal [34]. Therefore it is very difficult to use 2D-SFG to probe the 1→2 transition response of $\chi_{sample}^{(4)}$. To extract the pure contribution of $\chi_{sample}^{(4)}$, the PS technique should be incorporated in the fourth-order optical process.

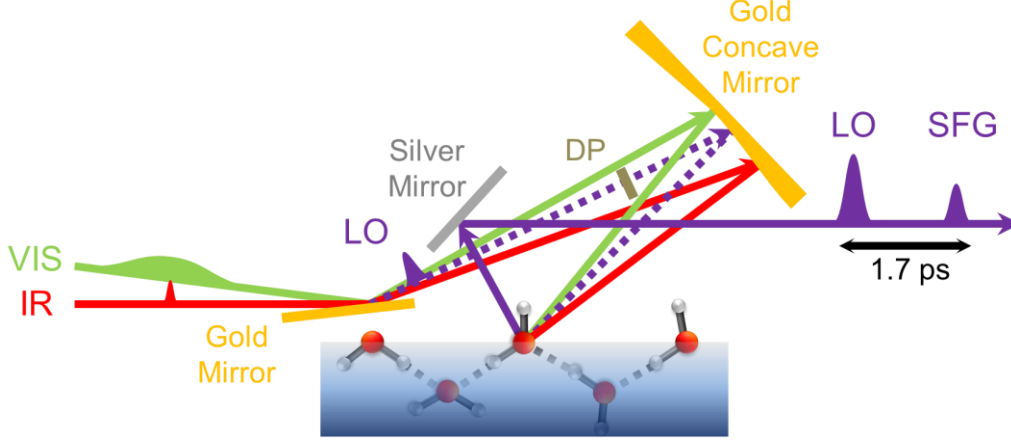


Fig. 1.6 Geometry of the PS-SFG experiment at the air/water interface.

The optical geometry of the PS-SFG experiments is depicted in Fig. 1.6. In this optical process, the SFG signal generated from the sample is mixed with a local oscillator (LO) with an independent phase. The detected field E_{det} is thus given by the sum of the contribution of the LO ($E_{LO}^{(2)}$) generated at the gold mirror and that of the sample ($E_{sample}^{(2)}$):

$$E_{det}(\omega_{SFG}) = r_{sample}(\omega_{SFG})E_{LO}^{(2)}(\omega_{SFG}) + E_{sample}^{(2)}(\omega_{SFG}) \quad (1.40)$$

where r_{sample} is the reflection coefficient of the sample at the SFG frequency. After introducing a delay plate (DP) in the LO beam path, the detected field reads:

$$E_{det}(\omega_{SFG}) = r_{sample}(\omega_{SFG})E_{LO}^{(2)}(\omega_{SFG})e^{i\omega_{SFG}\Delta t} + E_{sample}^{(2)}(\omega_{SFG}) \quad (1.41)$$

With this delay, the intensity spectrum detected on the CCD camera is given by:

$$\begin{aligned} I_{det} &= |E_{det}(\omega_{SFG})|^2 = |r_{sample}(\omega_{SFG})E_{LO}^{(2)}(\omega_{SFG})e^{i\omega_{SFG}\Delta t} + E_{sample}^{(2)}(\omega_{SFG})|^2 \\ &= |r_{sample}(\omega_{SFG})E_{LO}^{(2)}(\omega_{SFG})|^2 + |E_{sample}^{(2)}(\omega_{SFG})|^2 \\ &\quad + r_{sample}(\omega_{SFG})E_{LO}^{(2)}(\omega_{SFG})E_{sample}^{(2)*}(\omega_{SFG})e^{i\omega_{SFG}\Delta t} \\ &\quad + r_{sample}^*(\omega_{SFG})E_{LO}^{(2)*}(\omega_{SFG})E_{sample}^{(2)}(\omega_{SFG})e^{-i\omega_{SFG}\Delta t} \end{aligned} \quad (1.42)$$

By performing an inverse Fourier transform, eliminating the contribution around zero frequency (only the local oscillator, or only the sample contributions to the signal, the first two terms) and the contribution at negative frequencies (the last term), and performing the

Fourier transform back to the frequency domain, we obtain the complex cross term with the positive frequency:

$$I_{\text{det}} = r_{\text{sample}}(\omega_{\text{SFG}})E_{\text{LO}}^{(2)}(\omega_{\text{SFG}})E_{\text{sample}}^{(2)*}(\omega_{\text{SFG}})e^{i\omega_{\text{SFG}}\Delta t} \quad (1.43)$$

We take quartz as a reference, since the SFG signals generated at our VIS and IR frequencies on the quartz are purely nonresonant. By dividing the signals detected from the sample and from the quartz reference, we obtain:

$$I_{\text{PS-SFG}} \equiv \frac{r_{\text{sample}}(\omega_{\text{SFG}})E_{\text{LO}}^{(2)}(\omega_{\text{SFG}})E_{\text{sample}}^{(2)*}(\omega_{\text{SFG}})}{r_{\text{quartz}}(\omega_{\text{SFG}})E_{\text{LO}}^{(2)}(\omega_{\text{SFG}})iE_{\text{quartz}}^{(2)*}(\omega_{\text{SFG}})} = \frac{r_{\text{sample}}(\omega_{\text{SFG}})E_{\text{sample}}^{(2)*}(\omega_{\text{SFG}})}{r_{\text{quartz}}(\omega_{\text{SFG}})iE_{\text{quartz}}^{(2)*}(\omega_{\text{SFG}})} \quad (1.44)$$

Note here that we insert a factor i in the denominator to account for the 90° phase difference between the SFG response of the aqueous interface of the sample and the quartz crystal [36,37]. In this thesis, the sample is water, whose refractive index is constant (~ 1.33) in the range of the SFG frequency (~ 630 nm), and the same situation holds for quartz (~ 1.54). Substituting Eq. (1.35) into Eq. (1.44) results in:

$$I_{\text{PS-SFG}} \equiv \frac{r_{\text{sample}}(\omega_{\text{SFG}})E_{\text{sample}}^{(2)*}(\omega_{\text{SFG}})}{r_{\text{quartz}}(\omega_{\text{SFG}})iE_{\text{quartz}}^{(2)*}(\omega_{\text{SFG}})} = \frac{0.86\chi_{\text{sample}}^{(2)*}(\omega_{\text{SFG}})}{i\chi_{\text{quartz}}^{(2)*}(\omega_{\text{SFG}})} \quad (1.45)$$

Since SFG signals generated at the quartz surface are nonresonant, $\chi_{\text{quartz}}^{(2)}(\omega_{\text{SFG}})$ is constant (i.e. frequency independent), and $\chi_{\text{sample}}^{(2)}(\omega_{\text{SFG}})$ can be extracted from this equation without losing information of the real and imaginary parts.

For 2D-PS-SFG experiments, the fourth order terms also contribute to the electric field of the detected signals which then equal:

$$E_{\text{det}}(\omega_{\text{SFG}}) = r_{\text{H}_2\text{O}}(\omega_{\text{SFG}})E_{\text{LO}}^{(2)}(\omega_{\text{SFG}})e^{i\omega_{\text{SFG}}\Delta t} + E_{\text{sample}}^{(2)}(\omega_{\text{SFG}}) + E_{\text{sample}}^{(4)}(\omega_{\text{SFG}}) \quad (1.46)$$

and the intensity spectrum detected on the CCD camera is given by:

$$\begin{aligned} I_{\text{det}} &= |E_{\text{det}}(\omega_{\text{SFG}})|^2 = \left| r_{\text{H}_2\text{O}}(\omega_{\text{SFG}})E_{\text{LO}}^{(2)}(\omega_{\text{SFG}})e^{i\omega_{\text{SFG}}\Delta t} + E_{\text{sample}}^{(2)}(\omega_{\text{SFG}}) + E_{\text{sample}}^{(4)}(\omega_{\text{SFG}}) \right|^2 \\ &= \left| r_{\text{H}_2\text{O}}(\omega_{\text{SFG}})E_{\text{LO}}^{(2)}(\omega_{\text{SFG}}) \right|^2 + \left| E_{\text{sample}}^{(2)}(\omega_{\text{SFG}}) \right|^2 + \left| E_{\text{sample}}^{(4)}(\omega_{\text{SFG}}) \right|^2 \\ &\quad + r_{\text{H}_2\text{O}}(\omega_{\text{SFG}})E_{\text{LO}}^{(2)}(\omega_{\text{SFG}})E_{\text{sample}}^{(2)*}(\omega_{\text{SFG}})e^{i\omega_{\text{SFG}}\Delta t} \\ &\quad + r_{\text{H}_2\text{O}}^*(\omega_{\text{SFG}})E_{\text{LO}}^{(2)*}(\omega_{\text{SFG}})E_{\text{sample}}^{(2)}(\omega_{\text{SFG}})e^{-i\omega_{\text{SFG}}\Delta t} \\ &\quad + r_{\text{H}_2\text{O}}(\omega_{\text{SFG}})E_{\text{LO}}^{(2)}(\omega_{\text{SFG}})E_{\text{sample}}^{(4)*}(\omega_{\text{SFG}})e^{i\omega_{\text{SFG}}\Delta t} \\ &\quad + r_{\text{H}_2\text{O}}^*(\omega_{\text{SFG}})E_{\text{LO}}^{(2)*}(\omega_{\text{SFG}})E_{\text{sample}}^{(4)}(\omega_{\text{SFG}})e^{-i\omega_{\text{SFG}}\Delta t} \\ &\quad + E_{\text{sample}}^{(2)}(\omega_{\text{SFG}})E_{\text{sample}}^{(4)*}(\omega_{\text{SFG}}) + E_{\text{sample}}^{(2)*}(\omega_{\text{SFG}})E_{\text{sample}}^{(4)}(\omega_{\text{SFG}}) \end{aligned} \quad (1.47)$$

With the same procedure of obtaining Eq. (1.44), we get:

$$\begin{aligned}
I_{2D-PS-SFG} &\equiv \frac{r_{H_2O}(\omega_{SFG})E_{LO}^{(2)}(\omega_{SFG})E_{sample}^{(2)*}(\omega_{SFG}) + r_{H_2O}(\omega_{SFG})E_{LO}^{(2)}(\omega_{SFG})E_{sample}^{(4)*}(\omega_{SFG})}{r_{quartz}(\omega_{SFG})E_{LO}^{(2)}(\omega_{SFG})iE_{quartz}^{(2)*}(\omega_{SFG})} \\
&= \frac{r_{H_2O}(\omega_{SFG})[E_{sample}^{(2)*}(\omega_{SFG}) + E_{sample}^{(4)*}(\omega_{SFG})]}{r_{quartz}(\omega_{SFG})iE_{quartz}^{(2)*}(\omega_{SFG})}
\end{aligned} \tag{1.48}$$

Therefore the expression for the differential 2D-PS-SFG signal reads:

$$\Delta I_{2D-PS-SFG} = I_{2D-PS-SFG} - I_{PS-SFG} = \frac{r_{H_2O}(\omega_{SFG})E_{sample}^{(4)*}(\omega_{SFG})}{r_{quartz}(\omega_{SFG})iE_{quartz}^{(2)*}(\omega_{SFG})} \tag{1.49}$$

Substituting Eq. (1.35) and Eq. (1.36) into this expression results in:

$$\begin{aligned}
\Delta I_{2D-PS-SFG} &= \frac{0.86\chi_{sample}^{(4)*}(\omega_{SFG})}{i\chi_{quartz}^{(2)*}(\omega_{SFG})} E(\omega_{IR-pump})E^*(\omega_{IR-pump}) \\
&= \frac{0.86\chi_{sample}^{(4)*}(\omega_{SFG})}{i\chi_{quartz}^{(2)*}(\omega_{SFG})} I(\omega_{IR-pump})
\end{aligned} \tag{1.50}$$

Two observations can be made from Eq. (1.50). First, the intensity of the differential 2D-PS-SFG signal is proportional to the intensity of the pump pulse. Second, and more importantly, compared with Eq. (1.39), the differential 2D-PS-SFG signal eliminates the contribution of $\chi_{sample}^{(2)}(\omega_{SFG})$, and $\chi_{sample}^{(4)}(\omega_{SFG})$ can be extracted from the signal. Therefore, with the 2D-PS technique, we can estimate the spectral diffusion more accurately from the 2D plot, since the signal is not mixed with the steady-state signal. Details of the experiment will be described in chapter 5.

1.6 Thesis Outline

This thesis discusses measurements of the ultrafast dynamics of water molecules at the air/water interface. Chapter 2 provides an introduction to the various spectroscopic experimental setups performed in this thesis. Chapter 3 shows the ultrafast reorientation motion of dangling OH groups using TPR-SFG. In chapter 4 we study the mechanisms of the vibrational relaxation of the dangling OH groups with two-color TR-SFG. The 2D-PS-SFG experiment revealing the ultrafast dynamics of the hydrogen-bonded OHs at the air/water interface is presented in chapter 5. Chapter 6 deals with laser-induced shock wave propagation probed by SFG.

Chapter 2

Experimental Techniques

In setups employed in conventional sum-frequency generation (SFG) spectroscopy, a visible (VIS) and a frequency-tunable infrared (IR) beam are temporally and spatially overlapped on the sample surface [13,18,38,39]. For water surfaces, when the IR frequency is tuned into resonance with the frequency of the OH stretching mode of water molecules, the SFG signals are strongly, resonantly enhanced. This one-dimensional spectral signal, the SFG intensity as a function of IR frequency, provides us with information on the structure and hydrogen-bonding strength of interfacial water molecules. To understand the structural and energetic dynamics of specifically surface molecules, time-resolved SFG approaches are required [23,24,29,40,41].

Here we present novel setups for IR-pump/SFG-probe time- and polarization-resolved vibration spectroscopy [26] and phase-sensitive time-resolved vibrational spectroscopy. These setups allow for experiments aimed at elucidating the energetic and structural dynamics of specifically interfacial water molecules. In the experiments, interfacial water molecules are excited with an intense IR-pump pulse which is resonant with the molecular O-H stretch vibrations. The excitation of the water molecules and the subsequent relaxation of the excess vibrational energy are monitored by probing the same vibration with an IR/VIS-probe pulse pair, which generates sum-frequency signals from the interface. The reorientational motion and vibrational relaxation of the interfacial water molecules are determined in one-color polarization-resolved SFG spectroscopy, while the vibrational coupling between different modes is determined in two-color SFG spectroscopy. The homogeneity and heterogeneity of interfacial water molecules can be addressed using two-dimensional (2D) time-resolved phase-sensitive SFG spectroscopy.

2.1 Introduction

In this chapter, the experimental setups for time- and polarization-resolved vibrational sum-frequency generation (TPR-SFG) spectroscopy and two-dimensional phase-sensitive time-resolved vibrational sum-frequency generation (2D-PS-SFG) spectroscopy are described in detail. The first section focuses on the one- and two-color experimental setups, the sample part where the SFG signals are generated, and the detection optics and electronics. In the

second section the data analysis is discussed. The setup is built based on reference [32]. The notation of optics and optomechanics in the figures is as follows: B: Beam splitter, DB: Dichroic beam splitter, F: Filter, P: Polarizer, $\lambda/2$: Half-wave plate, L: Lens, TS: translation stage, MTS: Motorized translation stage, C: Chopper, DP: Delay plate, CL: Cylindrical lens, M1: Dielectric mirror for 800 nm, M2: Dielectric mirror for 1100 nm, M3: Gold mirror, M4: Dielectric mirror for SFG signals, and M5: Gold concave mirror with focal length $f = 50$ mm.

2.2 TR-SFG setup

The experimental setups are composed of three different parts; the first part consists of the laser system and the corresponding optical components used to generate the intense IR pump, IR probe, and VIS probe pulses. The second part consists of a rotating trough and a motorized stage to alleviate the effects of the heat generated by the intense IR beam and to compensate evaporation of the samples from which the SFG signals are generated. The last is the detection part which consists of collimated optics, a galvano mirror, and a monochromator with a CCD.

2.2.1 One-color experiments

For one-color experiments, shown in Fig. 2.1, a Ti:sapphire oscillator (Mira 900; Coherent Inc.) pumped by a CW laser (Verdi; Coherent Inc.) is used to seed a regenerative/multipass amplifier (Titan; Quantronix) which is pumped by a high energy (18 W, 100 ns) Nd:YLF laser (DQ-527, Quantronix). The amplifier output is centered at 806 nm with full width half maximum of 12 nm and is 120 fs long. The repetition rate is 1 kHz and the energy is 3.5 mJ/pulse. 1.1 mJ of this pulse energy is used to pump a commercial optical parametric amplification unit (TOPAS; Light Conversion, Vilnius, Lithuania) to produce ~ 300 μJ of signal (~ 1260 nm) and idler (~ 2200 nm) fields. The idler field is then frequency-doubled in a β -barium borate (BBO; $7 \times 7 \times 3$ mm³, $\phi = 90^\circ$, $\theta = 22.2^\circ$) crystal to generate ~ 30 μJ of ~ 1100 nm pulses. This doubled idler beam is then mixed with the remaining 2.3 mJ of the 806 nm Ti:sapphire output to generate the difference frequency in a KTiOPO_4 (KTP; $10 \times 10 \times 3$ mm³, $\phi = 0^\circ$, $\theta = 41.8^\circ$) crystal, leading to the production of pulses at a wavelength of ~ 3 μm , of 150 fs length, full width half maximum of 100 cm⁻¹ and 100 μJ IR pulse energy. The generated IR is split, using an 80:20 beam splitter, with the larger portion used for the IR pump and the smaller for the IR probe, so we can only pump and probe with the same

are arranged such that they are in a plane orthogonal to the air/water interface and have incident angles of $\sim 55^\circ$, 46° , and 53° , respectively, with respect to the surface normal. At the interface, two SFG signals are generated: one is the IR pump/VIS SFG signal and the other is the IR probe/VIS SFG signal. If the IR pump and IR probe are both 3300 cm^{-1} and the VIS beam is 806 nm , the IR pump/VIS (dashed purple line) and IR probe/VIS SFG (solid purple line) signals reflect from the interface are $\sim 53.4^\circ$ and 51.6° , respectively, with respect to the surface normal. Therefore the IR pump/VIS SFG signal can be spatially filtered out with a pin hole centered on the IR probe/VIS SFG signal. The band-pass filter after the collimating lens filters out other signals which have different wavelength from the SFG signals. The pulse energies of the IR pump, IR probe, and VIS probe at the sample for the one-color experiment are 24 , 6 , and $4\text{ }\mu\text{J/pulse}$, respectively, while for the two-color experiment they are 40 , 1 , and $4\text{ }\mu\text{J/pulse}$, respectively. The sample is distilled Millipore filtered water ($18\text{ M}\Omega\cdot\text{cm}$ resistivity) in a homemade Teflon trough, which is rotated at 7.5 rpm to suppress the effect of heat from successive laser shots. To perform an experiment, the infrared pump pulse is variably delayed with respect to the probe pulse (τ) using a mechanical delay line.

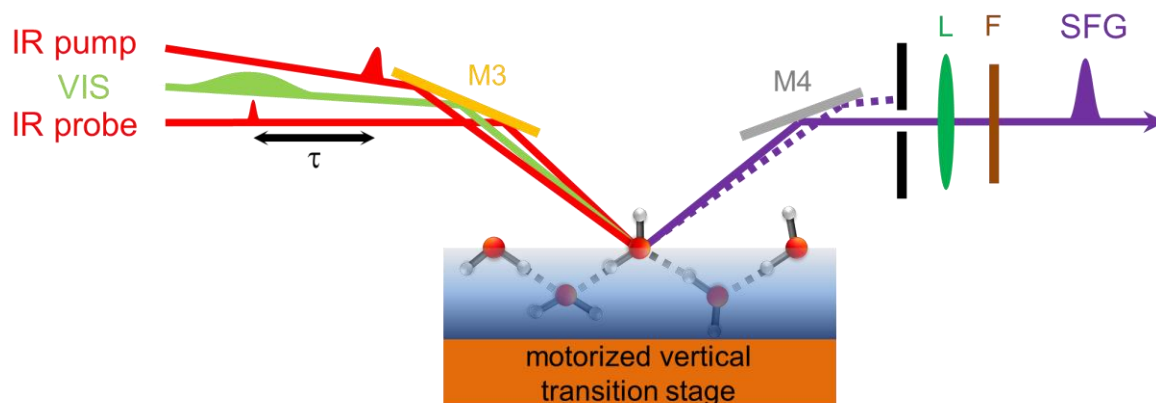


Fig. 2.3 Experimental geometry of time-resolved SFG setup at the sample.

For the 2D-PS-SFG, as shown in Fig. 2.4, the IR/VIS probe pair is first focused onto a gold mirror to generate a non-resonant SFG signal, which is used as the local oscillator (LO). After passing through a 1-mm thick fused silica plate, which causes a delay of 1.7 ps relative to the IR/VIS probe pair, the LO is then refocused, together with the remaining IR/VIS probe pair, onto the sample by means of a gold-coated spherical mirror with a focal length of 50 mm . The incident angles of the IR pump, IR probe, and VIS probe beams are $\sim 31^\circ$, 51° , and 40° , respectively, with respect to the surface normal. The sample signal and LO are collimated by a spherical lens. A height sensor (LK-G85, Keyence) with resolution of 200 nm

which is synchronized with a motorized z-direction translation stage (8MVT40-13-1, Standa) is used to compensate the height change caused by the evaporation of the water.

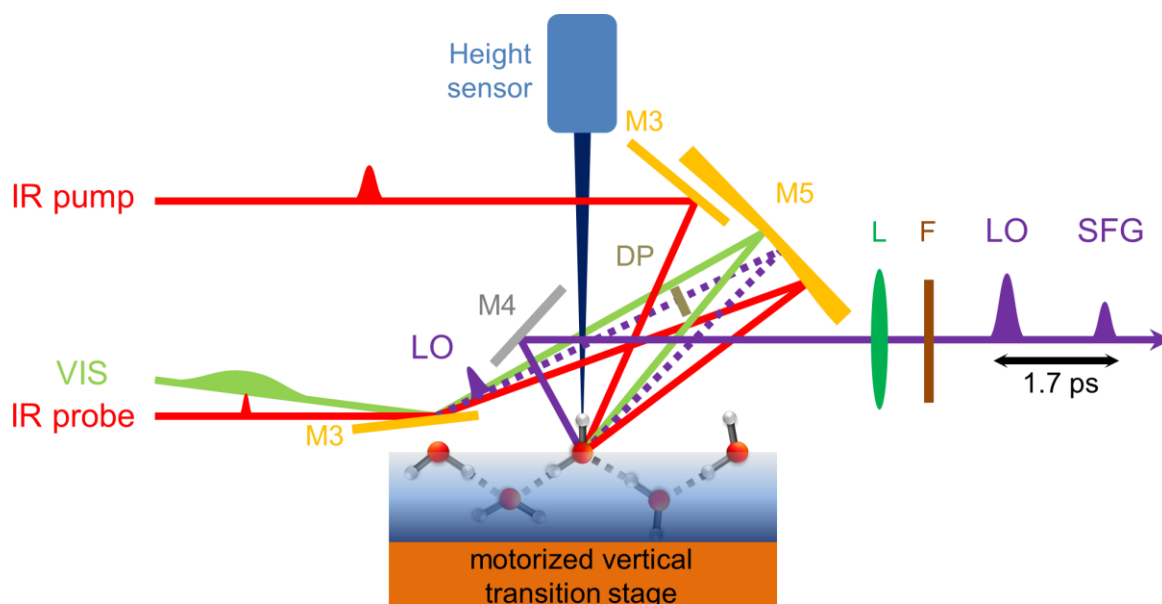


Fig. 2.4 Phase-sensitive time-resolved SFG setup at the sample.

The SFG signals generated at the interface are collected and collimated by a 200 mm positive lens, as shown in Fig. 2.5. The signals are then focused into the monochromator with two cylindrical lenses. The first cylindrical lens (CL1) with a focal length of 300 mm is used to focus the signal in the vertical while the second one (CL2) with a focal length of 50 mm is used to focus the signal in the horizontal. With this geometry, the SFG signal is loosely focused vertically and tightly focused horizontally. Combined with the galvano mirror inserted after CL1, we can spatially separate different SFG signals vertically on the CCD chip. If the galvano mirror is synchronized (500 Hz) and phase-locked with the chopper, i.e., the angle of the galvano mirror is related to chopping of the IR pump pulse, we can see two spectra in the spectrometer. One of the spectra includes the effect of the IR pump excitation and one is recorded without the pump pulse. For each delay time point, four spectra are recorded - a spectrum following excitation with a *p*-polarized pump pulse, followed by a spectrum without the pump pulse present, followed by an *s*-polarized pumped spectrum, followed by an unpumped spectrum. The polarization of the IR pump pulse is controlled by a $\lambda/2$ plate mounted in a motorized rotation stage. If the polarization-resolved experiment is not performed, only the *p*-pumped and unpumped signals are recorded. The normalized (differential) IR-pump/VSF-probe signals are computed as the ratio (difference) between the signals with and without the pump for each pump polarization independently. For TR-SFG

experiments, the SFG signals are detected by an electron-multiplied charge coupled device camera (EMCCD, iXon 897, Andor) in the monochromator. For phase-sensitive experiments, the SFG signals interfere with the LO in the monochromator and are then detected by the EMCCD (Newton 971, Andor).

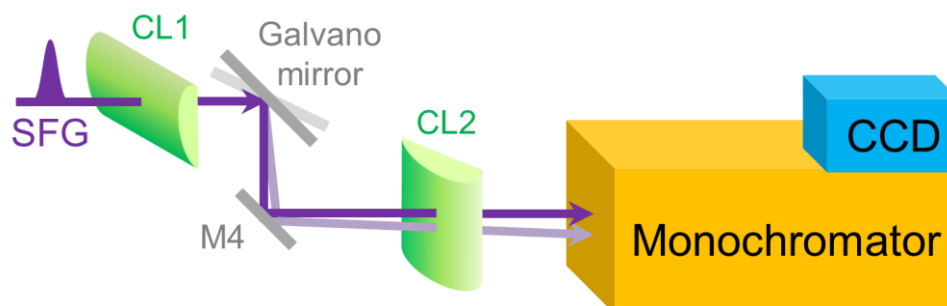


Fig. 2.5 Geometry of the detection optics.

2.3 Data analysis

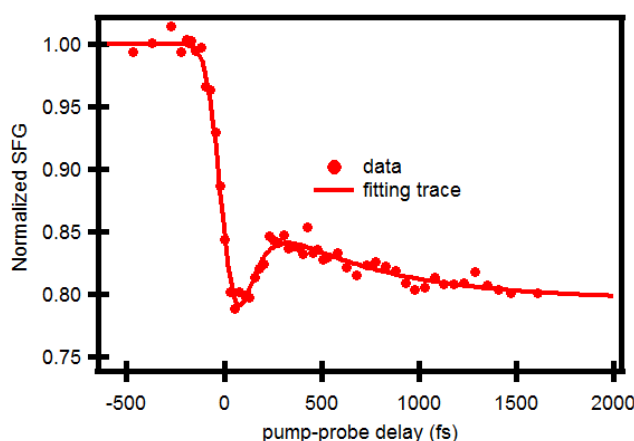


Fig. 2.6 A typical normalized IR-pump/SFG-probe signal of hydrogen-bonded OH groups at the air/water interface.

A typical example of normalized, one-color IR-pump/SFG-probe data recorded from the air/water interface is shown in Fig. 2.6. These data are plotted as the pumped spectra divided by the unpumped spectra with various time delays following Eq. (1.23), therefore at sufficient negative time delays the ratio equals one. For this experiment, the IR pump and IR probe were both centered at 3350 cm^{-1} , with a spectral width of approximately 100 cm^{-1} . The normalized SFG signals show fast recovery after the pump-induced bleach followed by an additional, slower decrease. The shape of the signal reflecting vibrational relaxation of the H-bonded OH groups of interfacial water molecules can be understood in the following manner [42–44]: The initial bleach originates from the pump-induced excitation of the OH

stretching mode from the ground state ($\nu = 0$) to the first excited state ($\nu = 1$). Due to the large anharmonicity of the OH stretching vibration, the SFG signal generated from the excited state is shifted out of the probing window, causing the decrease in the SFG signal. The partial recovery of the signal indicates that the excited population is transferred with a time constant T_1 to an intermediate level ν^* through intramolecular vibrational relaxation (IVR). For pure H_2O , ν^* is composed of the HOH bending mode ($\sim 1650 \text{ cm}^{-1}$) and the O–H \cdots O hydrogen bond stretch mode ($\sim 300 \text{ cm}^{-1}$). Since the overtone of the bending mode is at $\sim 3300 \text{ cm}^{-1}$, it can be the main recipient for the excess vibrational energy [45,46]. The long-time offset after the recovery is due to the sequential relaxation of the intermediate state to the “hot” ground state ($\nu' = 0$), caused by the relaxation of the excess energy from the bending mode to the low frequency libration mode, which leads to a full thermalization of the subensemble of the water molecules. Accordingly, the signal can be reproduced with a four-level cascade system (Fig. 2.7(a)) [24]. T_1 and τ_{eq} denote the sequential relaxation rate from of the excess energy from $\nu = 1$ to ν^* , then to $\nu' = 0$. We describe the dynamics of the population changes of the states by using the following set of differential equations:

$$\begin{aligned}
\frac{\partial N_0}{\partial t} &= -\sigma I(t)[N_0 - N_1] \\
\frac{\partial N_1}{\partial t} &= \sigma I(t)[N_0 - N_1] - N_1/T_1 \\
\frac{\partial N_{\nu^*}}{\partial t} &= N_1/T_1 - N_{\nu^*}/\tau_{eq} \\
\frac{\partial N_{\nu'}}{\partial t} &= N_{\nu^*}/\tau_{eq}
\end{aligned} \tag{2.1}$$

where N_0 , N_1 , N_{ν^*} , and $N_{\nu'}$ denote the population of state $\nu = 0$, $\nu = 1$, ν^* , and $\nu' = 0$, respectively. Here, the exponential decay of the cascading process is assumed for the vibrational relaxation from $\nu = 1$ to ν^* and from ν^* to $\nu' = 0$, while the pumping efficiency is determined by the population difference of the ground and excited states. σ is the absorption cross-section from the $\nu = 0$ to $\nu = 1$ transition and $I(t)$ is the intensity of the time-dependent IR pump pulse. For conventional TR-SFG spectroscopy, the normalized SFG signal can be calculated as:

$$I_{SFG}^N(t) = \frac{\{\chi_0[N_0(t) - N_1(t)] + \chi_{\nu^*}N_{\nu^*}(t) + \chi_{\nu'}N_{\nu'}(t)\}^2}{[\chi_0N_0(t \ll 0)]^2} \tag{2.2}$$

In our analysis, we fit the time trace data by coupling Eqs. (2.1) and (2.2). The values of T_1 , τ_{eq} , χ_0 , χ_{ν^*} , and $\chi_{\nu'}$ are free parameters taken from the fit to the data, where χ_0 , χ_{ν^*} ,

and $\chi_{\nu'}$ are the effective susceptibilities of the OH oscillators in the $\nu = 0$, ν^* , and $\nu' = 0$ states, respectively. The trace that describes the data depicted in figure 2.6 was calculated using equation (2.2) with parameters fit to the data. Clearly, the description works very well, allowing us to extract information on the dynamics of the H-bonded OH stretching mode of interfacial water molecules from the data. However, the time-dependent SFG signal reflects not only the vibrational energy relaxation of molecules with the specific vibrational frequency excited by the pump pulse, but the signals are also affected by the reorientational motion of interfacial molecules: following vibrational excitation with the pump pulse, excited OH groups can reorient away from, and towards, the polarization axis of the probe, making those specific molecules contribute less, respectively more, to the signal.

Inversely, using an appropriate experimental scheme, the molecular reorientation motion can be revealed by time-resolved SFG experiments, specifically using pump pulses with different polarizations (TPR-SFG technique). Differently polarized pump pulses will excite OH groups of specific orientation with orientation-dependent efficiency: if the transition dipole moment of the OH group is oriented along the polarization axis of the pump pulse, excitation will be relatively efficient. Therefore, in addition to the lifetime of the OH groups, the reorientation motion of these OH groups can also be measured by using the time-resolved SFG technique; the recovery of the difference of the signals between SFG signals when IR pump and IR probe pulses are polarized parallel (both p -polarized) and those when IR pump and IR probe pulses are orthogonally polarized (IR pump is s -polarized and IR probe is p -polarized) will reveal the in-plane and out-of-plane motion of these OH groups [47]. The detailed description of how to calculate the TPR-SFG signal has been offered previously [27] and will be discussed in chapter 3.

On the other hand, TR-SFG can be combined with phase-sensitive detection approaches, which we have implemented in our 2D-PS-SFG spectroscopy scheme. 2D-PS-SFG spectroscopy is analogous to the 2D-IR technique, with the additional characteristic of being surface-specific. The differential 2D-PS-SFG signal eliminates the contribution of $\chi_{sample}^{(2)}(\omega_{SFG})$, which is shown in Eq. 1.50. Therefore, for the 2D-PS-SFG experiment, the differential $\text{Im}[\chi^{(2)}]$ calculated from the four-level model is

$$\Delta \text{Im}[\chi^{(2)}](t) = \chi_0[N_0(t) - N_1(t)] + \chi_{\nu^*}N_{\nu^*}(t) + \chi_{\nu'}N_{\nu'}(t) - \chi_0N_0(t \ll 0) \quad (2.3)$$

The details of extracting the time constant of vibrational relaxation and spectral diffusion from the 2D-PS-SFG data will be described in chapter 5.

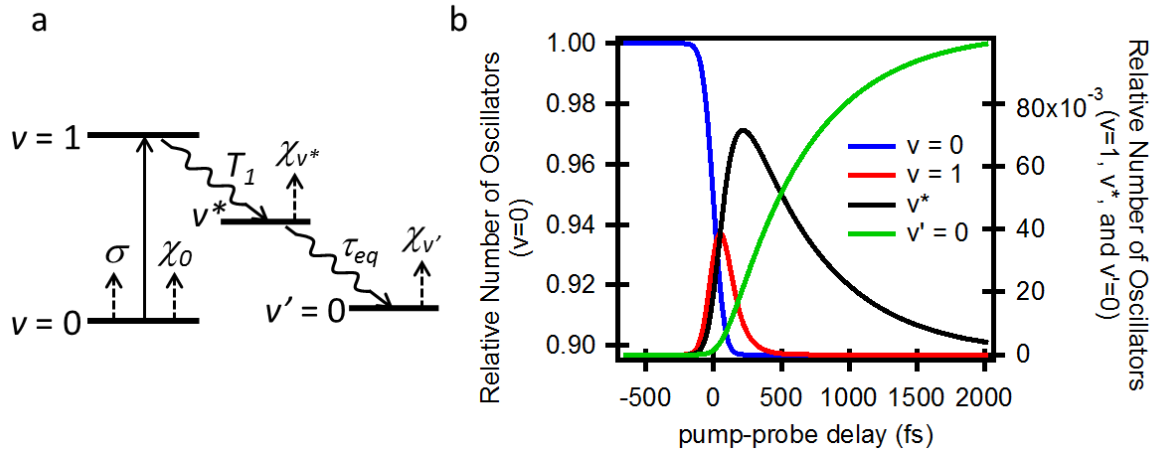


Fig. 2.7 (a) A 4-level system used to describe the energy flow pathway of hydrogen-bonded OH groups. $v = 0$, $v = 1$, v^* , and $v' = 0$ are the ground state, first excited state, intermediate state, and “hot” ground state, respectively. σ is the absorption cross-section from the $v = 0$ to $v = 1$. T_1 and τ_{eq} denote the sequential relaxation rate from of the excess energy from $v = 1$ to v^* , then to $v' = 0$. χ_0 , χ_{v^*} , and $\chi_{v'}$ are the effective susceptibilities of the OH oscillators in the $v = 0$, v^* , and $v' = 0$ states, respectively. (b) Time variations of the populations for each vibrational state obtained from fitting the data in Fig. 2.6 using Eq. (2.1).

The populations of each vibrational state are depicted as a function of pump-probe delay time in Fig. 2.7(b). We can see a decrease in the population in the ground state ($v = 0$) with a rapid increase in the first excited state ($v = 1$). This figure shows that the vibrational lifetime of the OH stretching mode ($T_1 < 100$ fs) is very short, and the population of $v = 1$ is transferred to v^* state followed by the slow relaxation to the heated ground state ($v' = 0$).

Chapter 3

Ultrafast Reorientation of Dangling OH Groups at the Air/Water Interface

In this chapter, we report the real-time measurement of the ultrafast reorientational motion of water molecules at the air/water interface, using femtosecond time- and polarization-resolved vibrational sum-frequency generation (SFG) spectroscopy. Vibrational excitation of dangling OH bonds along a specific polarization axis induces a transient anisotropy that decays due to the reorientation of vibrationally excited OH groups. The reorientation of interfacial water is shown to occur on sub-picosecond time scales, several times faster than in the bulk, which can be attributed to the lower degree of hydrogen bond coordination at the interface. Molecular dynamics simulations of interfacial water dynamics are in quantitative agreement with experimental observations and show that, unlike in the bulk, interfacial reorientation occurs in a largely diffusive manner.

3.1 Introduction

A molecular level understanding of how water meets surfaces is important for many topics in electrochemistry, atmospheric chemistry, and membrane biophysics. These interfaces require the termination of the bulk water hydrogen-bonded network and thus have unique water structure and properties, e.g., water's high surface tension. While always different from bulk, the specific properties of interfacial water depend on the adjoining phase. Of particular interest, both because of its ubiquity and its relationship to the solvation of hydrophobic phases more generally, are the properties of water at the air/water interface.

The structure of water at the air/water interface has been studied extensively both experimentally and theoretically [13,48–51]. These studies have shown that the interfacial width is ~ 1 nm [49–51], and that part of the surface is covered with non-hydrogen-bonded, free OH groups, sticking into the vapor phase [13,48]. However, in analogy to the bulk, interfacial molecules are expected to be structurally dynamic over ps time scales. Insight into these dynamics is essential for a complete understanding of interfacial water and interfacial hydration processes. Because the free OH is the least coordinated of aqueous species and is a general feature of water near hydrophobic surfaces [52], it seems likely that the dynamics of these water species play an important role in determining the air/water interface reactivity

and in the molecular mechanisms of hydrophobic solvation [53,54]. While water near small hydrophobic groups has been shown to slow down relative to bulk water [55–57] in both experiment and simulation, the dynamics of water near extended surfaces are substantially less studied. In the simulation study of an idealized extended hydrophobic surface a population of water molecules was identified with one OH group pointing away from bulk liquid whose dynamics were sped up relative to bulk [58].

In this chapter, the experimental measurement of water structural dynamics at an extended interface is presented. We find that rotation of interfacial free OH is accelerated by $3\times$ relative to bulk water. The experimental results are complemented by MD simulations, which are in quantitative agreement and shed additional light on the mechanism of interfacial reorientation.

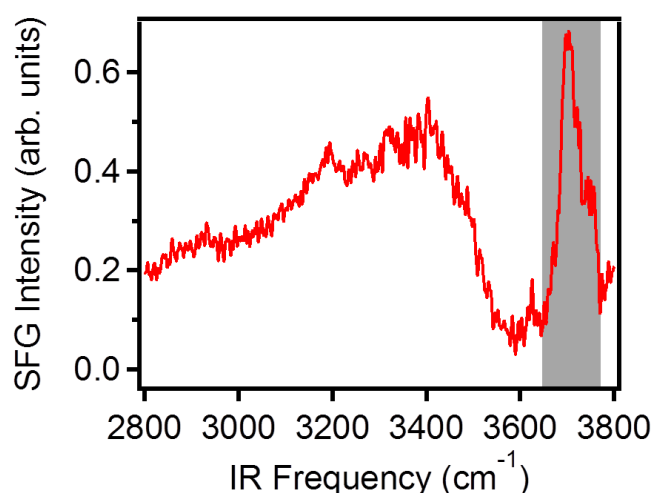


FIG 3.1 Time-averaged SFG spectrum of the air/H₂O interface. In our IR-pump/SFG-probe experiment, only the free OH (grey rectangle) is pumped and probed.

We probe the rotational motion of water at the air/water interface using femtosecond time- and polarization-resolved vibrational SFG spectroscopy, an extension of time-resolved SFG spectroscopy [23,24,41,59]. In a conventional SFG experiment, infrared and visible laser pulses are overlapped in space and time on an aqueous surface, and the sum frequency of the two laser fields generated selectively at the surface is detected. If the infrared light is resonant with the OH stretch vibration of the surface water, this process is resonantly enhanced and the vibrational spectrum of the outermost few layers of water molecules is recorded (i.e., SFG spectroscopy). A time-averaged SFG spectrum of the OH stretch frequency window at the air/water interface is shown in Fig. 3.1. As first shown by Du and

Shen, this spectrum contains a broad feature at lower frequencies that is due to interfacial OH groups that are hydrogen-bonded, and a narrow peak near 3700 cm^{-1} which is the response of OH groups that are non-hydrogen-bonded (i.e., free OH) and point towards the vapor [13,60]. In this study we employ a time- and polarization-resolved IR-pump/SFG-probe scheme in which the frequency of the pump and probe IR pulses is centered on the free OH: we vibrationally excite an orientational subset of free OH groups and track their vibrational and reorientational relaxation. Previous theoretical efforts by Nienhuys *et. al.* and Gengeliczki *et. al.* have shown that such experiments provide insight into interfacial reorientational motion [27,61].

3.2 Experimental section

The one-color TPR-SFG experimental setup is described in detail in chapter 2, section 2.2.1 and 2.2.3. Briefly, the free OH groups are pumped and probed in the experiment. A series of normalized SFG transients ($I_{pump-on}^{SFG} / I_{pump-off}^{SFG}$) are recorded as a function of pump-probe delay time. The sample is distilled Millipore filtered water ($18\text{ M}\Omega\text{-cm}$ resistivity) in a homemade Teflon trough, which is rotated at 7.5 rpm to suppress the effect of heat from successive laser shots. The SFG spectra were recorded under *ssp* (SFG, VIS, IR probe) polarization conditions, with either *s*- or *p*-polarized IR pump, at different delay times between pump and probe. Polarizations are defined relative to the *yz* plane (i.e., the plane of incidence). The polarization of each beam was controlled by a combination of polarizers and $\lambda/2$ wave plates. In this case of the pump beam the $\lambda/2$ wave plate was motorized to allow the collection of alternate polarization pumped spectra. To perform an experiment, the pump pulse was variably delayed with respect to the probe pulse using a mechanical delay line with four spectra -- a *p* pumped, followed by an unpumped, followed by an *s* pumped, followed by an unpumped -- collected at each time point. The normalized IR-pump/SFG-probe signal was computed as the ratio between the integrated intensities with and without the pump for each pump polarization independently.

3.3 Simulation Details

Classical all-atom molecular dynamics simulations of the air/water interface using the molecular dynamics package NAMD and the SPC/E model for water [62,63] were performed by Ana Celia Vila Verde in Prof. Peter Bolhuis' group. Molecular dynamics trajectories were

visualized and analyzed using the package VMD [64]. Van der Waals interactions were smoothly connected to zero by applying the smoothing function for $10 \text{ \AA} < r_{ij} < 12 \text{ \AA}$, where r_{ij} is the interatomic distance between atoms i and j . Electrostatic interactions were calculated in a real space for $r_{ij} < 12 \text{ \AA}$ and using the Particle Mesh Ewald method with a grid spacing of 1 \AA for a reciprocal space. A Verlet algorithm was used for integrating equations of motions. Van der Waals forces were calculated every 2 fs, electrostatic forces every 4 fs and the remaining forces every 1 fs. The SHAKE algorithm was used to fix the lengths of all bonds involving hydrogen. We began the simulations by generating a $30 \text{ \AA} \times 30 \text{ \AA} \times 60 \text{ \AA}$ cell containing 826 water molecules with periodic boundary conditions. This system was next equilibrated for 1 ns in the NVT ensemble (box volume maintained constant and thermostat set to 300 K). Following equilibration all observables were taken from a 2 ns simulation of the same system (resulting in a periodic system with 30 \AA of vacuum between vapor/water interfaces) in the NVE ensemble at an average temperature of 294 K. A snapshot of an equilibrated conformation is shown in Fig. 3.2. Frames for analysis of OH motion were taken every 2 fs.

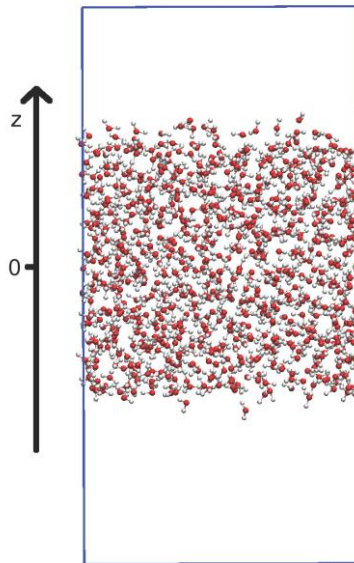


FIG. 3.2 Geometry of the simulated system. The z -axis is perpendicular to the surface of the simulated water slab. At each saved configuration, $z = 0$ is defined as the z position at the center of mass of the water slab.

3.3.1 Coordinate system

The z -axis is defined as the axis perpendicular to the surface of the simulated water slab as shown in Fig. 3.2. The spherical coordinate system (r, θ, ϕ) used here is illustrated in Fig. 3.3. Individual free OH groups are represented with arrows along the O-H bond. In addition to the

azimuthal angle, ϕ , and polar angle, θ , associated with the spherical coordinate system we also use a third angle, ω , which is the angular distance between any two points at the surface of a sphere as shown in Fig. 3.3.

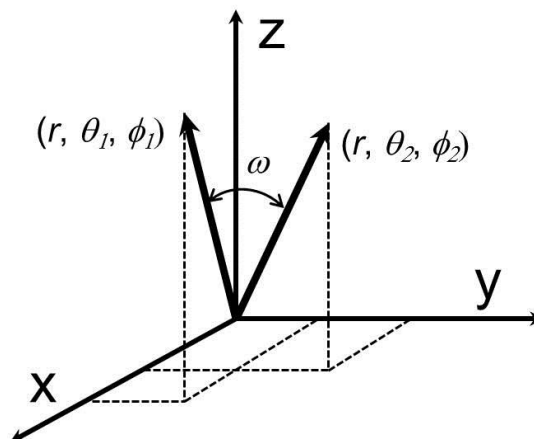


FIG. 3.3 Spherical coordinate system used. The z -axis is perpendicular to the surface of the water slab. ω is the angle formed by two vectors of coordinates (r, θ_1, ϕ_1) and (r, θ_2, ϕ_2) .

In what follows, θ_t and ϕ_t denote the values of the corresponding angles at time t whereas $\theta(t)$, $\phi(t)$ or $\omega(t)$ denote angular differences measured with respect to θ_0 , ϕ_0 , or ω_0 . The angle θ is a bounded quantity, so $\theta(t) = \theta_t - \theta_0$. In contrast, the angles ϕ and ω can vary between $-\infty$ and $+\infty$ and are calculated by unfolding the periodic trajectory described by each free OH group following a procedure described in the references [65,66]. This procedure requires that our free OH groups do not rotate by more than 180° between consecutive configurations. Here we ensure that this condition is met by taking configurations separated by only 4 fs.

3.3.2 Definition of the interface

To define the interfacial region, we first calculated the fraction f of free OH groups as a function of the distance along the z -axis from the center of mass ($z = 0$) of the water slab shown in Fig. 3.4 (see Fig. 3.3 for the definition of the z -axis). Unless otherwise noted, a hydrogen bond exists if $\text{O}-\text{H}\cdots\text{O} > 140^\circ$ and $\text{O}\cdots\text{O} < 3.5 \text{ \AA}$. The average f for SPC/E water in the bulk is taken from the region $0 < |z| < 8 \text{ \AA}$ and is, for our hydrogen bond definition, $f_{bulk} = 0.15$, that is, 85% of the OH groups has a hydrogen bond. In this work the interface is taken to be the region for which $f > 1.1 f_{bulk}$, i.e., the region where $|z| > |z| (f = 1.1 f_{bulk})$. Changing

the definition of the interface to the region for which $f > 1.4 f_{bulk}$ affects our quantitative results (e.g. θ_m changes by 5°) but not our qualitative conclusions.

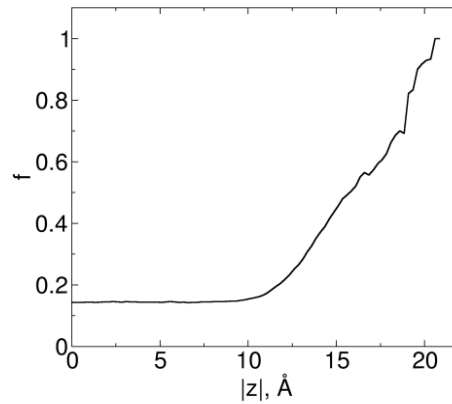


FIG. 3.4 Fraction of free OH groups as a function of the distance from the center of mass of the water slab.

3.4 Results and Discussion

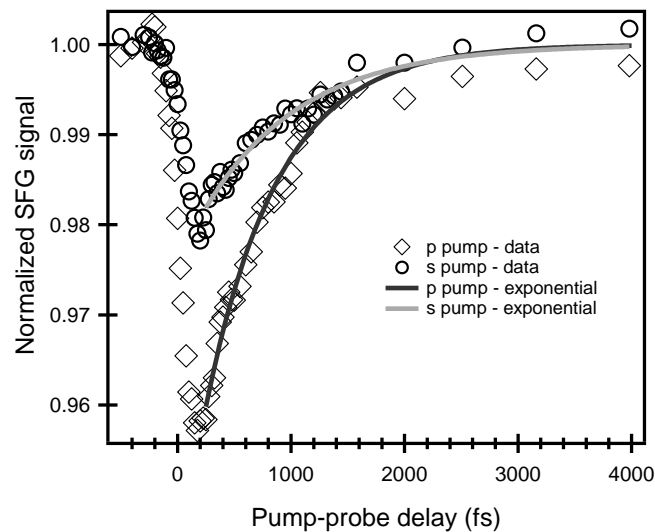


FIG. 3.5 IR-pump/SFG-probe data for free OH groups with two different pump polarizations, along with mono-exponential fits to the data. The extracted time constant for the recovery of the p pumped trace is 640 ± 40 fs and for the s pumped trace 870 ± 100 fs.

A representative IR-pump/SFG-probe result is shown in Fig. 3.5. The normalized IR-pump/SFG-probe signal is computed as the ratio between the integrated intensities (in grey area in Fig. 3.1) with and without the pump. The two traces are recorded in one experimental run. For both pump polarizations excitation of OH groups from the $\nu = 0$ vibrational ground state to the $\nu = 1$ first vibrationally excited state leads to a transient decrease in the SFG

signal (the SFG signal is shifted out of our frequency window due to the anharmonicity of the vibration). Two important observations can be made from the raw data: (i) at zero delay time, significant anisotropy exists between s - and p -polarized pump transients and (ii) the recovery of the normalized SFG signals is significantly faster for the p -polarized pump trace (640 ± 40 fs), than the s -polarized, (870 ± 100 fs; uncertainty is 2σ).

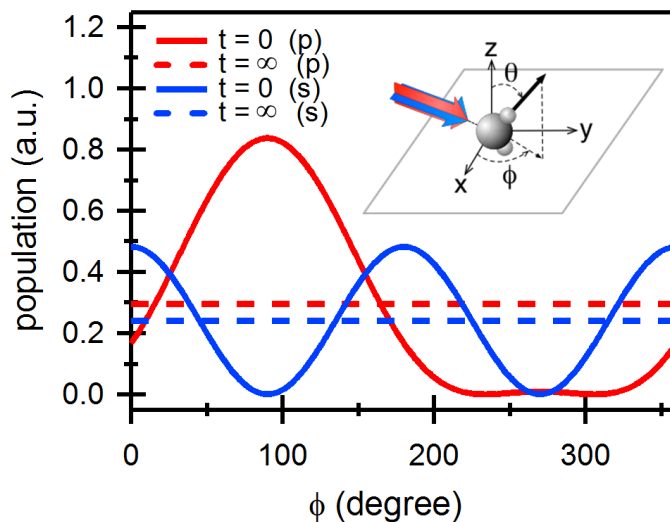


FIG. 3.6 Distribution of excited OH groups as a function of ϕ for s and p polarized IR pump at pump/probe overlap ($t = 0$) and at long pump/probe delays for $\theta_m = 59^\circ$ and $\Delta\theta = 26^\circ$ and the experimental IR pump angle. Inset: Experimental geometry. The p -polarized pump has its E field in the yz plane.

Regarding (i), the initial anisotropy can be understood by noting that when IR pump and IR/SFG probe are polarized parallel (both p polarized), those OH groups that are most efficiently pumped (pump efficiency $\propto |\mu_{\text{OH}} \cdot E_{\text{pump}}|^2$, as shown in section 1.4) are also most efficiently detected; when pump and the IR portion of the SFG probe are orthogonally polarized, the differential signal is smaller. More specifically, Fig. 3.6 shows that, for parameters relevant to our experiment (see discussion below) – angle of incidence of IR pump 50° , and average angle of OH groups with surface normal $\theta_m = 59^\circ$ and full width at half maximum (FWHM) distribution $\Delta\theta = 26^\circ$ – at $t = 0$ the excited state population with p -polarized IR pump is larger and exhibits an angular distribution dramatically different from that for the s -pumped case (the p -pumped distribution peaks at $\phi = 90^\circ$ while the s -pumped peaks at $\phi = 0^\circ$ and $\phi = 180^\circ$, shown in Fig. 1.4). These features will occur for any interfacial moiety that has a preferred distribution with respect to θ and none with respect to ϕ – e.g., any liquid – under excitation by an IR pump in reflection geometry. To actually calculate the

SFG response at $t = 0$ requires additionally accounting for the hyperpolarizability tensor, Fresnel factors and angles of the probe beams. As is shown in Fig. 3.7 and discussed further below, such a calculation reproduces our data quite well and thus tightly constrains the possible average and distribution of θ for the free OH: the larger bleach seen in the p - compared to the s -pumped signals at time zero sensitively depends on free OH orientation.

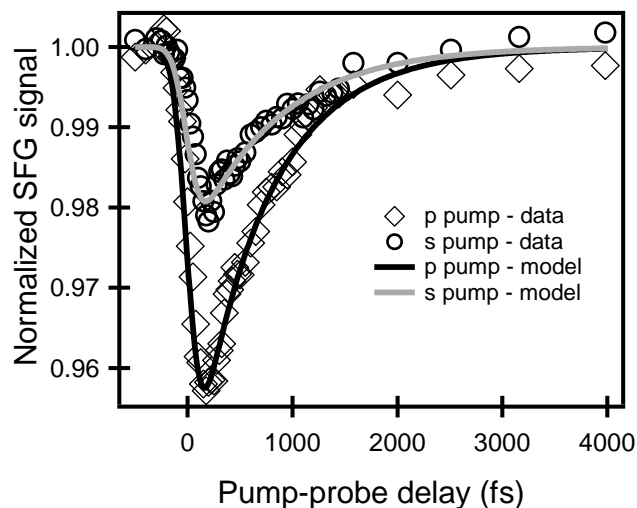


FIG. 3.7 IR-pump/SFG-probe data for free OH at air/water interface with s - and p -polarized pump. The black and grey lines are generated using the numerical model of Nienhuys and Bonn [27] with the parameters independently obtained from the molecular dynamics simulations reported here: $D_\phi = 0.32 \text{ rad}^2/\text{ps}$, $D_\theta = 0.36 \text{ rad}^2/\text{ps}$, $\tau_v = 800 \text{ fs}$, average angle $\theta_m = 59^\circ$ and FWHM of angular distribution $\Delta\theta = 26^\circ$.

Regarding (ii), the differences in rate of signal recovery as a function of pump polarization can be understood as follows. In principle both the p - and s -pumped traces are influenced by reorientational motion and vibrational relaxation (with time scale τ_v). τ_v is expected to be independent of pump pulse polarization. This suggests that the differences in rate of signal recovery are a function of reorientation. Indeed, one would expect the p channel to exhibit substantially more decay due to reorientation than the s channel, in analogy to bulk anisotropy measurements: the p -polarized pump pulse preferentially excites those OH groups that are efficiently detected with the SFG probe pair that also contains a p -polarized IR-SFG probe pulse. As these OH groups reorient away from angles where they are efficiently detected, the signal will decay. In contrast, for the s -polarized pump, reorientation may cause motion towards orientations to which the p -polarized IR-SFG probe pulse is sensitive, effectively slowing down the decay.

In principle, reorientational relaxation can also be due to rapid intermolecular excitation transfer. Such dipole-dipole excitation transfer between differently oriented OH

groups is known to dominate the polarization anisotropy decay, which can be addressed by polarization-resolved ultrafast transient IR absorption experiments for pure H₂O [67,68]. Estimates of its rate (assuming a Förster type dipole-dipole coupling mechanism), however, suggest that the characteristic time scale of excitation transfer for free OH at the air/water interface exceeds 20 ps: our observables are influenced only by reorientation and vibrational relaxation.

Prior theoretical analysis [27] suggests that our signal responds principally to reorientation in the plane of the interface (i.e., change in ϕ), vibrational relaxation (τ_v), and average angle with respect to the surface normal (θ_m). Armed with this insight, we initially quantify reorientation rate of the free OH by assuming that the distribution of θ is a delta function and that there is no out-of-plane reorientation [18,60,61]. The observed difference between the magnitude of the *s*- and *p*-polarized normalized SFG signals is particularly sensitive to the angle θ ; fits of our data with an assumed delta function distribution suggest $\theta = 55^\circ$. If we further assume that the in-plane reorientational motion is diffusive and that vibrational relaxation occurs exponentially with a single time constant, fitting the data following the numerical prescription offered previously [27] suggests that the free OH in-plane angular diffusivity is $D_\phi = 1.25 \pm 0.2 \text{ rad}^2/\text{ps}$ and $\tau_v = 850 \text{ fs}$. The diffusivity of $D_\phi = 1.25 \text{ rad}^2/\text{ps}$ implies the free OH reorients $> 10\times$ faster than that in the bulk (see [66] and below). While one might expect faster reorientation of motion at the interface, a speedup by a factor exceeding 10 seems unphysically fast, casting doubt on the assumption of describing the orientational distribution of free OH groups using a delta function.

Indeed, prior polarization-resolved static SFG studies, and simulation studies have suggested that θ assumes a distribution with a FWHM of at least 10° [60]. Such a distribution suggests that any model of the spectroscopic response should include out-of-plane motion of the dangling OHs. In addition, recent studies of OH reorientation in bulk water have found that the angular motion is nondiffusive [69,70] over picosecond time scales. Because we are interested in free OH motion over the same time scales, our assumption of diffusive reorientation may rightly be questioned.

To investigate both the effect of a finite angular distribution of OH groups and the potential nondiffusive nature of surface reorientation in more detail, we turn to classical all-atom simulation of the air/water interface using the extended simple point charge (SPC/E) water model. The molecular dynamics simulation shows that the histograms of θ for free OH

groups at the interface show a fairly broad angular distribution centered near $\sim 55^\circ$ (Fig. 3.8). This distribution implies that there is an effective potential that restrains the angular motion of the free OH along the surface normal and that physically valid modeling of our experimental results requires both out-of-plane and in-plane motion.

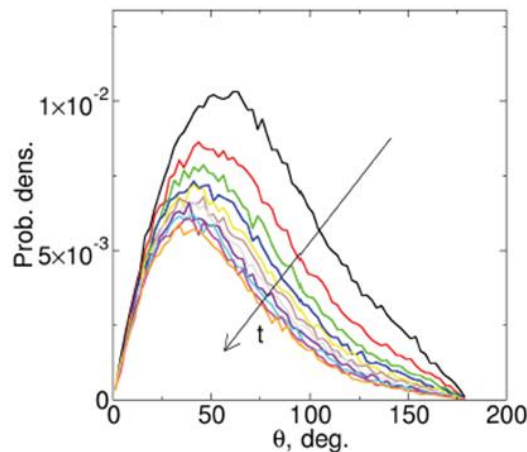


FIG. 3.8 Histograms of out-of-plane angle (θ) of the free OH at the air/water interface as a function of the lifetime of the free OH (no lifetime requirement, 40, 60, 80, 100, 120, 140, 160, 180 and 200 fs, arrow indicates histogram of populations with increasing lifetime.) Clearly, with increasing lifetime the free OH population decreases. Each histogram is normalized to the total population of free OH groups with no lifetime restriction. The plot illustrates that longer-lived free OH groups tend to have a lower value of θ (they point closer to the surface normal) and a narrower distribution.

But is the motion of surface water molecules diffusive? Regardless of mechanism, we expect that in-plane reorientation should be unhindered by a potential. As described by Einstein and Debye [71] and in numerous places subsequently [72], the mean-square angular displacement ($\langle\langle\phi^2\rangle\rangle$) should increase linearly with time for diffusive motion; a log-log plot of ($\langle\langle\phi^2\rangle\rangle$) vs time should produce a line with a slope of one. Fig. 3.9 shows such a plot for both in-plane angular reorientation of free OH and reorientation of OH in bulk water (within the SPC/E model where reorientation in bulk is defined with respect to the angle ω of rotation from time $t = 0$ to $t = \tau$). As illustrated, the in-plane angular motion of the free OH, while not exactly diffusive, is far nearer than that of OH in the bulk. As discussed above, if out-of-plane motion is also diffusive it will be within a potential. In such systems mean square angular displacement approaches a constant value with time [73]. As is shown Fig. 3.10, plots of $\langle\theta^2\rangle$ for the free OH show this behavior.

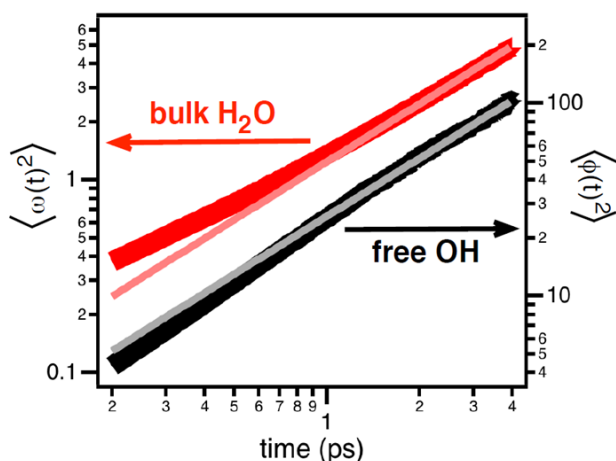


FIG. 3.9 Mean square angular displacement $\langle \phi^2 \rangle$ of the free OH and of OH in bulk water ($\langle \omega^2 \rangle$). Thick lines are simulation results. Thin, lighter colored lines are fits to these results assuming a purely diffusive behavior. The diffusive approximation works well for the free OH.

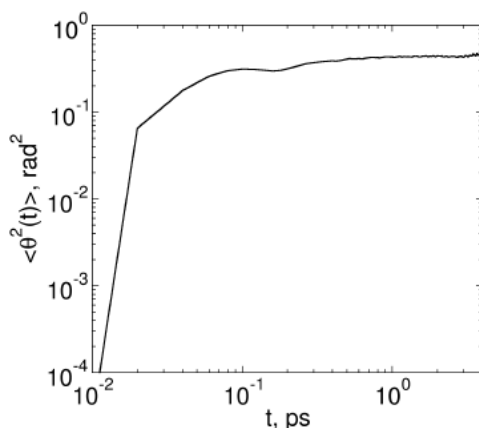


FIG. 3.10 Mean square out-of-plane angular displacement of the free OH ($\langle \theta^2(t) \rangle$).

Reorientation in bulk is known to be non-diffusive over 0.2-1.5 ps timescales because within this time window individual OH groups make large ($\sim 68^\circ$), rapid (each jump takes less than 300 fs [70]), infrequent (every several picoseconds) jumps. To test whether the moment in which a free OH forms a hydrogen bond is similarly rapid, we also examine the in-plane and out-of-plane motion of the free OH when forming a hydrogen bond. While, as expected, there is little correlation between ϕ and hydrogen bond formation (results not shown), trajectories with respect to θ illustrate a different relationship (an average trajectory is shown in Fig. 3.11). Inspection of Fig. 3.11 confirms that the duration of the jump is approximately ~ 0.5 ps marginally longer than that of OH reorientation in bulk. However, for SPC/E water in bulk the characteristic time between jumps has been shown to be 3.3 ps [70] or 4.1 ± 0.5 ps [74] (where the difference depends on the description of the transition state).

For the free OH the relevant timescale in comparison is given by the free OH lifetime, $\tau_v = 800$ fs. The poor separation of timescales between jump duration and inverse jump frequency observed for free OH groups at the interface, and the broad and partially overlapping distributions in θ observed before and after the jump are all consistent with an approximation of the movement of the free OH along θ as diffusive.

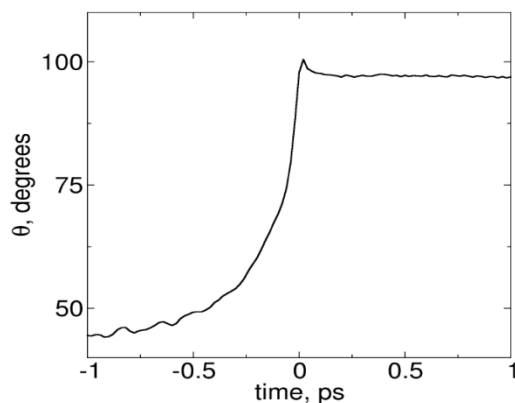


FIG. 3.11 Average trajectory in θ of free OH groups as they establish a hydrogen bond (at $t = 0$).

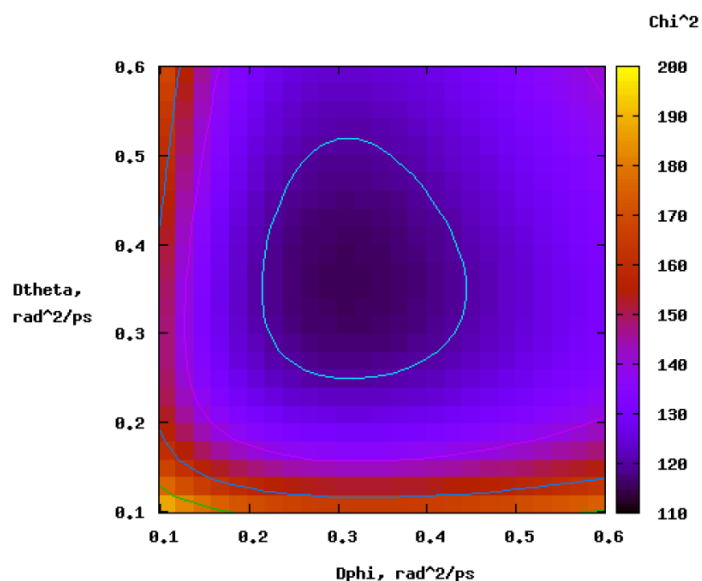


FIG. 3.12 Variation of goodness of fit χ^2 with D_ϕ and D_θ for free OH groups at the interface. The minimum χ^2 is at $D_{\phi,int} = 0.32$ rad²/ps, $D_{\theta,int} = 0.36$ rad²/ps.

To extract D_ϕ and from D_θ simulation, we model the free OH reorientation results from the molecular dynamics simulations as two-dimensional diffusion: reorientation within the plane of the surface (ϕ) and out of the plane of the surface (θ) where a potential exists in the latter coordinate (see Fig. 3.3 for the definition of ϕ and θ). We calculate the resulting goodness of fit metric χ^2 to describe the misfit of the diffusion model and the MD results.

The distribution of χ^2 as a function of D_ϕ and D_θ for free OH groups at the interface is shown in Fig. 3.12. The minimum of this distribution is at $D_{\phi,int} = 0.32 \text{ rad}^2/\text{ps}$, $D_{\theta,int} = 0.36 \text{ rad}^2/\text{ps}$.

To estimate the lifetime of the free OH groups we compute the following autocorrelation function from MD

$$P_{HB}(\tau) = \langle n_{HB}(t)n_{HB}(t+\tau) \rangle \quad (3.1)$$

where $n_{HB}(t) = 1$ ($n_{HB}(t+\tau) = 1$) if the OH group is not donating a hydrogen bond at time t ($t+\tau$) and is zero otherwise, and the average is over all time origins t for which $n_{HB}(t) = 1$. Absorbing boundary conditions are used (i.e., $n_{HB}(t+\tau)$ is set to zero from the instant a hydrogen bond is formed onwards). The resulting curve is then fitted to an exponential of the form $A \exp(-\tau/\tau_v)$ for all values of $\tau > 80$ fs, which avoids most of the initial non-exponential decay. This results in the reported $\tau_v = 850 \pm 100$ fs. The associated uncertainty reflects the dependence of τ_v on the time interval used for the fit.

The five parameters for our model as extracted from SPC/E simulations of free OH are, $D_\phi = 0.32 \frac{\text{rad}^2}{\text{ps}}$, $D_\theta = 0.36 \frac{\text{rad}^2}{\text{ps}}$, $\tau_v = 800$ fs, $\theta_m = 59^\circ$ and $\Delta\theta = 26^\circ$. Since the fitting with $\tau_v = 800$ fs instead of 850 fs provides a better description of the experimental data, we used $\tau_v = 800$ fs, which is within the error bar of the lifetime extracted from the simulation. Armed with these parameters, a detailed description of how to calculate the signal has been offered previously [27]. Fig. 3.7 shows the application of this model to the data. As is clear from inspection, the physical characteristics of the free OH from the simulation allow a quantitative description of the free OH dynamics with no adjustable parameters.

Direct comparison of our experimental data to polarization-resolved transient infrared absorbance of water in bulk is difficult as IR-pump/SFG-probe measurements in our experimental geometry sample a sum of correlation functions not equivalent to that measured in the former technique [61]. Similarly, comparison of our extracted D_ϕ and D_θ for the free OH to bulk are difficult because the motion of bulk water is known to be non-diffusive over our experimentally probable time window [69,70]. Taking advantage of the ability of the SPC/E potential to simulate reorientational dynamics of bulk water in quantitative agreement with experiment, we can impose an arbitrary reference frame on bulk water and extract a D_ϕ and D_θ consistent with simulation that reproduces known experimental constraints. The distribution of χ^2 with D_ϕ and D_θ is shown in Fig. 3.13. The minimum is found at $D_\phi = 0.11 \text{ rad}^2/\text{ps}$ and $D_\theta = 0.09 \text{ rad}^2/\text{ps}$: the free OH reorients $\sim 3\times$ faster than does water in bulk. This

speed up of water rotation near the air/water interface is in direct contrast to the slowdown of the rotation observed near small hydrophobic solutes and in qualitative agreement with a prior computational study of water near an idealized hydrophobic surface [58].

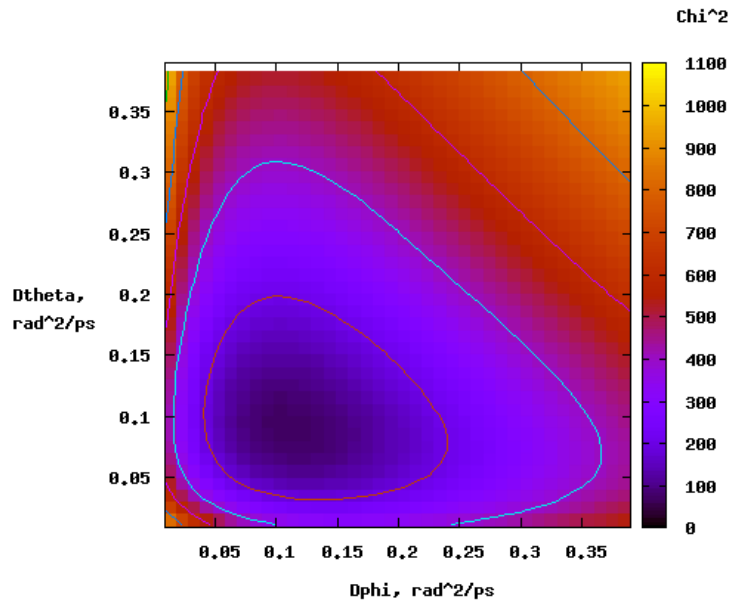


FIG. 3.13 Variation of χ^2 with D_ϕ and D_θ for water in the bulk. The minimum χ^2 is at $D_{\phi,bulk} = 0.11$ rad²/ps, $D_{\theta,bulk} = 0.09$ rad²/ps.

3.5 Conclusion

Prior work has shown that increasing free energy of wetting (for an increasingly hydrophobic surface) correlates with the creation of a population of increasingly dynamically labile interfacial water molecules. To this point only dynamical properties averaged over long times or many water molecules have been described: there has been no insight into how individual water molecules might contribute to this behavior. Here we show, for the first time experimentally, that these macroscopic time-averaged changes are also accompanied by a change in molecular reorientation: the air/water interface is characterized by a population of dangling OH groups that, in contrast to water near both small hydrophobic and hydrophilic solutes, rotates dramatically faster than bulk.

Chapter 4

Mechanism of Vibrational Energy Dissipation of Free OH Groups at the Air/Water Interface

In chapter 3 we show that the dangling OH groups reorient $3\times$ faster than the H-bonded OH groups in the bulk water. Furthermore, we find that the lifetime of these dangling OH groups is ~ 800 fs, which is slower than the bulk. In this chapter we elucidate the rate and mechanism of vibrational energy dissipation of water molecules at the air/water interface using femtosecond two-color time-resolved vibrational sum-frequency generation (SFG) spectroscopy. Vibrational relaxation of non-hydrogen bonded OH groups occurs on a sub-picosecond time scale in a manner fundamentally different from hydrogen-bonded OH groups in bulk, through two competing mechanisms: intramolecular energy transfer (IET) and ultrafast reorientational motion that leads to free OH groups becoming hydrogen-bonded. Both pathways effectively lead to the transfer of the vibrationally excited modes from free to hydrogen-bonded OH groups, from which relaxation readily occurs. Of the overall relaxation rate of interfacial free OH groups at the air/H₂O interface two-thirds are contributed by IET, while the remaining one-third is dominated by the reorientational motion.

4.1 Introduction

Knowledge of the rates and mechanisms of the relaxation of excess vibrational energy is indispensable to fully understand physical and chemical processes of water and aqueous solutions, such as chemical reactions rates and pathways, proton transfer, and hydrogen bond dynamics. Much prior work has therefore focused on characterizing vibrational energy relaxation of the OH and OD bond stretch vibration in water and its isotopologues [14,75–78]. This energy relaxation in bulk water has been studied using time-resolved transient infrared (IR) vibrational spectroscopy, revealing that both intra- and intermolecular energy transfer due to dipole and multipole couplings [68] and relaxation through the overtone of the HOH bending mode (intramolecular coupling) followed by sequential energy dissipation to the libration modes occur [46,79].

In contrast to the depth of understanding obtained for vibrational energy relaxation in bulk water, a limited number of studies have been carried out for aqueous interfaces [23,35,80], despite their relevance for chemical processes, e.g., atmospheric

chemistry [81], water splitting [82], and membrane function [83]. Interfacial water differs from bulk water due to the disruption of the water hydrogen-bonded (H-bonded) network. Previous works [23,24,35,84,85] have focused primarily on the energy relaxation dynamics of H-bonded interfacial water molecules. However, hydrophobic interfaces such as the prototypical air/water interface are enriched with free OH groups pointing towards the air [8,13,60,86–90]. These water molecules lead to distinct structural orientation, reorientational motion (chapter 3), and intra-/intermolecular energy coupling due to the differences in the density of water at the interface and the bending and stretching mode frequencies with respect to bulk water [80,91]. A central question is how the vibrational relaxation mechanisms of free OH groups at the interface differ from H-bonded interfacial OH groups, and those in the bulk.

In an SFG experiment, an IR pulse is overlapped at the surface in both time and space with a visible (VIS) pulse and the output at the sum of the frequencies of the two incident fields monitored. This SFG emission is, within the dipole approximation, interface specific in media with bulk inversion symmetry and is a spectroscopy because it increases in intensity by $> 10^4$ when the frequency of the incident IR is tuned into resonance with a normal mode of the molecules at an interface [39]. As initially shown by Shen and coworkers, and subsequently a variety of others, because the quadrupole response from liquid water is relatively low, SFG spectroscopy can furnish the OH stretch response of just the water molecules within 1-2 layers of an interface [92–94].

Because of its environmental ubiquity, experimental simplicity and its relevance to understand hydrophobic solvation more generally, much work has focused on the spectral response of interfacial water at the air/water interface [80,87,95]. A SFG spectrum (Fig. 4.1) for the air/water interface shows a broad band at lower frequency (3100 - 3500 cm^{-1}), attributed to H-bonded OH groups, and a narrow peak at higher frequency ($\sim 3700 \text{ cm}^{-1}$), attributed to free OH groups [8,13,87,88]. While it is clear that these spectral features report on the structure of interfacial water, extracting this structural information from the measured response has proven extremely challenging. This challenge is not unique to the SFG spectral response of interfacial water. It can be straightforwardly demonstrated that, for a particular resonance apparent in any one-dimensional (frequency) vibrational spectrum, the extent to which inhomogeneous broadening, anharmonic coupling to other modes, and chromophore motion influence the observed spectral response cannot be unambiguously determined [96]. As a consequence the extent to which a spectrum is influenced by molecular structure cannot

be unambiguously defined. Much prior work has shown that all of these factors influence the SFG spectral response of interfacial water. In particular, significant inter- and intramolecular coupling is known to dominate the hydrogen bonded portion of the spectrum and water molecule motion is known to occur on sub ps time scales [46,68,79]. The fact that multiple possible effects may explain the observed spectral response of interfacial water has been clearly demonstrated, for the low frequency portion ($\sim 3100\text{ cm}^{-1}$) of the hydrogen bonded OH at the air/H₂O interface, by the Morita and Skinner groups, who have shown that the experimental spectral response can be equally well reproduced by computational models with quite different underlying physics [93,97].

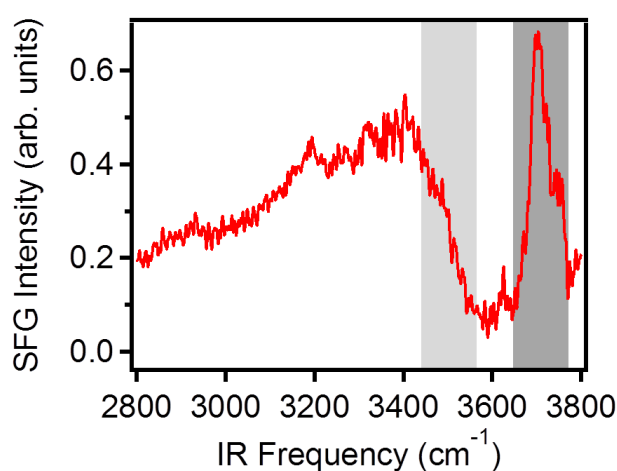


FIG. 4.1 Static SFG spectrum of the air-H₂O interface. Dark grey and light grey rectangles mark the spectral region of free and H-bonded OH, respectively, that are excited and detected in the pump-probe experiments.

Because it is particularly important in understanding hydrophobic solvation and because, as discussed above, prior work strongly suggests it should be simpler, we focus initially on understanding the influence of interfacial water structure and structural dynamics on the free OH peak shown in Fig. 4.1. Changes in the free OH resonance peak amplitude or width are routinely observed with changes in aqueous solution composition [8,88]. To correctly interpret and understand these changes evidently requires understanding the physical factors determining the line width, that is, the degree to which the measured free OH spectral response is controlled by pure dephasing (elastic interactions typically with low-frequency mode that modulate the free OH frequency) and the free OH vibrational energy lifetime.

To deconvolute the relative influence of vibrational lifetime and pure dephasing on the lineshape, a method of directly measuring one of these two quantities with interfacial

specificity is required. We and others have recently applied a time-resolved ultrafast IR-pump/SFG-probe scheme to elucidate vibrational energy relaxation dynamics of OH groups at a variety of interfaces [23,24,26,33,35]. In these experiments, an IR pump pulse excites OH groups at a specific vibrational frequency, and the effect of that excitation is followed in time with the SFG probe pulse pair. For the excited OH groups, the SFG intensity is temporarily decreased ('bleach'), and the recovery of the signal is a result of vibrational relaxation. For the free OH both at the air/water and hydrophobic self-assembled monolayer/water interface, slow relaxation (0.85 – 1.2 ps) has been reported [23,26]. As the homogenous dephasing time (T_2) of the free OH is 221 fs (given the measured FWHM in Fig. 4.1 and assuming inhomogeneous contributions to the line width are negligibly small) it is clear that the line width of the free OH spectral response is influenced by vibrational lifetime and thus that revealing changes in free OH spectral response with aqueous phase composition or with the composition of the adjoining phase, requires understanding of the free OH vibrational relaxation mechanism.

Three possible relaxation pathways can be identified. Previously we have shown that free OH groups reorient on a timescale (~ 1 ps) very similar to vibrational relaxation [26,98]. This observation suggests that one possible relaxation mechanism is the rotation of excited OH groups towards the bulk and formation of a hydrogen bond after which energy dissipation occurs rapidly as a result of the increased anharmonicity of the O-H vibrational potential. In what follows we term this mechanism the REOR vibrational relaxation pathway. A second relaxation mechanism has been proposed from the appearance of the cross peaks in two-dimensional SFG spectra of D₂O at the air-D₂O interface: the vibrational energy of the free OD is transferred to the H-bonded OD in the same D₂O molecule, which is weakly H-bonded, on sub-picosecond timescales [33]. Hereafter we describe this as the intramolecular energy transfer (IET) relaxation pathway. Finally, in liquid water much prior experimental and computational work has shown that the vibrational relaxation of the OH stretch proceeds through the overtone of the bending mode, to the bend fundamental, to whole molecule librations [46]. Without additional information, it seems plausible that relaxation of the excited free OH might occur in a similar manner; in what follows we term this mechanism the intramolecular vibrational relaxation (IVR) pathway. These mechanisms are schematically illustrated in Fig. 4.2.

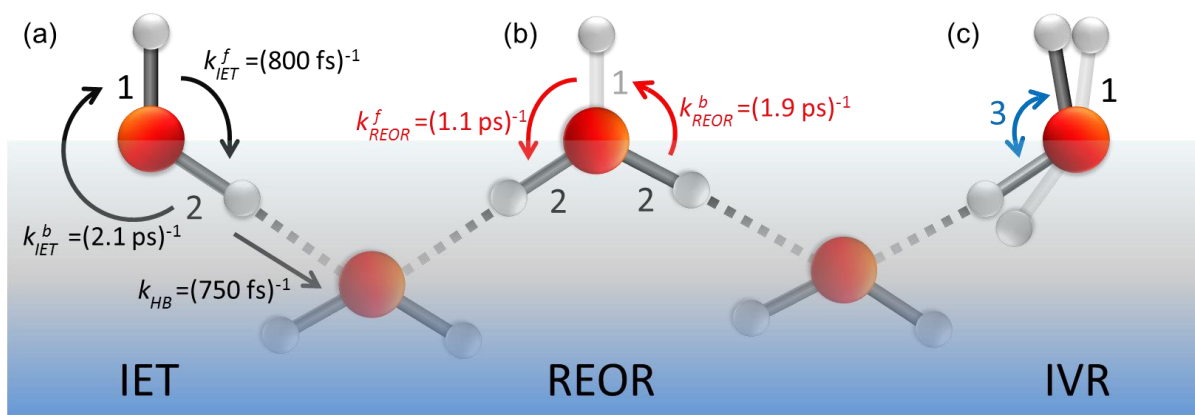


FIG. 4.2 Schematic of the pathways for vibrational relaxation of free OH groups. (a) Intramolecular energy transfer (IET), which indicates the energy coupling between free OH (label 1) and H-bonded OH (label 2). (b) Reorientational motion of the free OH (label 1) which rotates into the bulk and forms a hydrogen bond (REOR). (c) Intramolecular vibrational relaxation (IVR), which represents the coupling between the free OH stretching (label 1) and the bending modes (label 3) of the water molecules.

In this chapter, we resolve the relative roles of these mechanisms in the vibrational relaxation of interfacial free OH groups at the air/water interface. By analyzing two-color TR-SFG signals we show that the exchange of excited vibrational energy between free OH and H-bonded OH occurs on a sub-picosecond timescale. Using isotopically diluted water, we suppress intra- and intermolecular coupling while leaving structural relaxation processes relatively unaffected. Our results show that IET explains two-thirds of the vibrational relaxation of the free OH groups in pure H₂O while the remaining one-third is the result of REOR.

As noted above, SFG spectra of interfacial water do not uniquely determine interfacial structure. Our quantification of vibrational lifetime and relaxation mechanism provides an important additional piece of information to evaluate otherwise equally plausible descriptions of the physical mechanisms underlying the spectral response. More generally, as alluded to above, much prior work seems to suggest that the free OH plays an important role in the free energy of solvation of objects ranging from small hydrophobic moieties, to large amphiphilic macromolecules (such as proteins) to extended hydrophobic and amphiphilic surfaces [53]. Since this free energy of solvation is thought to be an important driving force in processes as diverse as protein folding, colloidal aggregation and hydrophobic collapse, the quantitative understanding we here gain of what, exactly, controls the interfacial free OH spectral response, and what we probe when we probe the free OH, seems likely to be of interest to a wide community of bio- and soft matter chemists and physicists.

4.2 Experimental section

The two-color TR-SFG experimental setup is described in detail in chapter 2, section 2.2.2 and 2.2.3. Briefly, the free OH and weakly H-bonded groups are pumped and probed in the experiment. A series of normalized SFG transients ($I_{pump-on}^{SFG} / I_{pump-off}^{SFG}$) are recorded as a function of pump-probe delay time. The samples were distilled Millipore filtered H₂O (18M Ω -cm resistivity) mixed with D₂O (Cambridge Isotope Laboratories, Inc., 99.93 % purity, used without further purification) and placed in a homemade Teflon trough which was rotated at 8 rpm to reduce cumulative heating. The IR-pump/SFG-probe spectra were recorded under *p/ssp* (IR pump/SFG, VIS probe, IR probe) polarization. The differential IR-pump/SFG-probe signal was computed as the ratio between the integrated intensities with and without the pump.

4.3 Results and discussion

To study the vibrational energy dynamics of the free OH group (dark grey area in Fig. 4.1), we excite these OH groups at $\sim 3700 \text{ cm}^{-1}$ with an IR pump pulse and probe the response with SFG probe pulse pair as a function of delay time. The data, after integrating the measured SFG intensity from 3650 to 3750 cm^{-1} (with respect to the IR probe frequency, red curve in Fig. 4.3), show a 10% bleach which recovers on a sub-ps timescale. A single-exponential fit to the data gives a time constant for the recovery of the SFG signal of $T_{H_2O} = 840 \pm 50 \text{ fs}$ for the free OH in pure H₂O. This timescale can of course be a result of a combination of the three prospective relaxation pathways: IET, REOR, and IVR. Put in more formal notation, we expect that $k_{VR}^{(H_2O)} = k_{IET/IVR}^{(H_2O)} + k_{REOR}^{(H_2O)} = (0.84 \text{ ps})^{-1}$, where k is the rate constant associated with the energy relaxation process and we have lumped together the IET and IVR pathways into a single term for reasons that will become clear below.

To help us quantify the contribution of each of these pathways we require an experiment that allows us to selectively switch one (or more) off. To do so we next performed a similar IR-pump/VSF-probe experiment probing the free OH of HDO at the air/water interface. Because of the large energy mismatch between the free OH ($\sim 3700 \text{ cm}^{-1}$) and H-bonded OD ($\sim 2600 \text{ cm}^{-1}$) stretch and the HDO, H₂O and D₂O bend frequencies [99–101], neither near resonant energy transfer between the OD and OH stretch on the same water molecule nor relaxation from the OH stretch through the overtone of the bend is probable in

HDO [14,79]. Put another way, in HDO we expect the IET and IVR pathways to be shut down ($k_{IET}^{(HDO)} = k_{NR}^{(HDO)} = 0$) and vibrational relaxation to be therefore dominated by REOR.

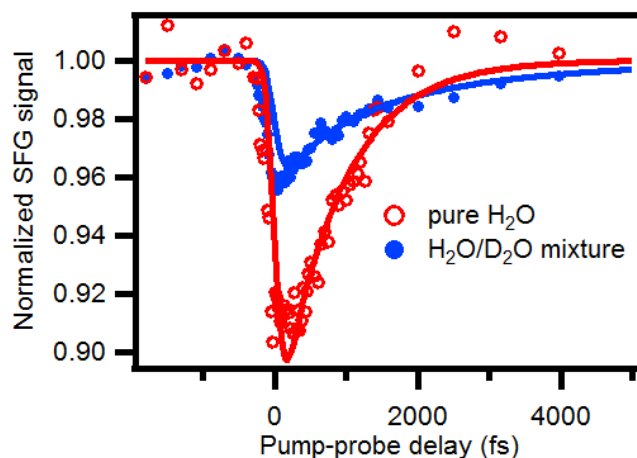


FIG. 4.3 IR-pump/SFG-probe data for excitation and detection of free OH groups at the air/water interface for pure (red, open circles) and isotopically diluted H₂O (H₂O:D₂O = 1:1, blue, filled circles). The red curve is the monoexponential fitting of the pure H₂O sample and the blue curve is the biexponential fitting of the H₂O-D₂O mixture, which shows that the time constant of the vibrational relaxation of free OH for H₂O and HDO are 840 fs and 2.6 ps, respectively. Both fit curves are convoluted with the system response.

The blue curve in Fig. 4.3 displays the IR-pump/SFG-probe result for exciting and probing the free OH stretching mode at the air/water interface for a H₂O-D₂O mixture (1:1 molar ratio). As is clear from inspection, the timescale of SFG signal recovery is much slower for the mixture than pure H₂O (the red curve). This qualitative observation strongly suggests that both the IET and/or IVR pathways are important in describing the vibrational relaxation of the free OH of H₂O. To quantify the importance of IET/IVR relative to REOR we need to fit the data. For the H₂O-D₂O mixture (given a small interfacial isotope fractionation [86]), half of the free OH groups in our excitation volume are part of an H₂O molecule; the other half are part of HDO [48]. Assuming these two types of free OH groups contribute equally to the measured signal from the mixture, and therefore fitting this data using a biexponential with two equal amplitudes and taking $T_{H_2O} = 840$ fs for free OH in H₂O, we find that the timescale of signal recovery of the free OH in HDO, T_{HDO} , is 2.6 ± 0.3 ps: three times slower than that of the free OH in H₂O. Taking, $k_{IET}^{(HDO)} = k_{NR}^{(HDO)} = 0$, and assuming that the reorientation rate of an OH group in HDO is similar to that of an OH group in H₂O,

we thus have $k_{REOR}^{(HDO)} = k_{REOR}^{(H_2O)} = (2.6 \text{ ps})^{-1}$. Recalling that, $k_{VR}^{(H_2O)} = 1/T_{H_2O} = (0.84 \text{ ps})^{-1}$, we obtain $k_{IET/IVR}^{(H_2O)} = k_{VR}^{(H_2O)} - k_{REOR}^{(H_2O)} = (1.24 \text{ ps})^{-1}$.

Because both IET and IVR are suppressed in HOD, quantifying the relative importance of these two pathways requires different types of experiments. Here we do so by performing an IR-pump/SFG-probe experiment in which we excite the free OH (i.e. the frequency range shown in the dark grey rectangle) and probe the blue side (weakly hydrogen bonded) of the hydrogen bonded OH spectral response (i.e. the light grey rectangle in Fig. 4.1). Prior work has shown that this frequency range corresponds to the OH stretch of the hydrogen bonded half of a water molecule that contains a free OH [102].

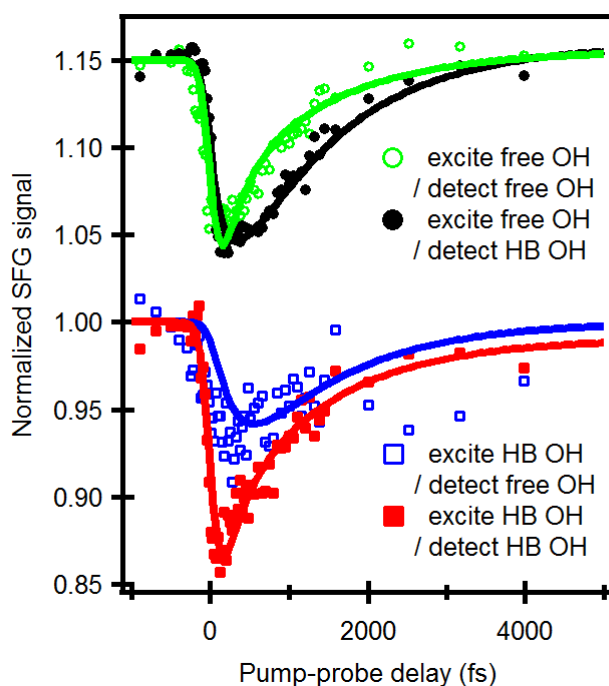


FIG. 4.4 IR-pump/SFG-probe data for free OH and H-bonded (HB) OH groups at the air/water interface. The upper two traces are data with 3700 cm^{-1} IR pump/ 3700 cm^{-1} (green, open circles) and 3500 cm^{-1} (black, filled circles) probes, while the lower two traces are data with 3500 cm^{-1} IR pump/ 3700 cm^{-1} (blue, open squares) and 3500 cm^{-1} (red, filled squares) probes. Solid lines are fits with a vibrational relaxation model (for details, see supplemental material). The green and black curves have an offset of 0.15.

The IR (free OH) pump/SFG (weakly hydrogen bonded) trace, with probe intensities integrated from 3450 cm^{-1} to 3550 cm^{-1} , is shown in black in Fig. 4.4. For comparison the free OH IR pump and free OH SFG probe is shown as a green curve in Fig. 4.4 (same data as red curve in Fig. 4.3). Three qualitative features of the comparison are readily apparent: there is a $\sim 300 \text{ fs}$ delay between the directly free OH pumped signal (green trace) and the coupling

signal (black trace), the bleach magnitudes (the signal size) are similar for both experiments and both traces have an initial bleach followed by a monotonic recovery. This relatively small delay between the pumped and coupling traces is consistent with a scenario in which vibrational energy is effectively transferred from the free OH to weakly H-bonded OH populations by energy transfer and/or reorientation of free OH groups to become H-bonded. Similarly, the nearly identical size of the bleach for both signals suggests that no energy is lost from the system in this transfer: the great majority of the vibrational excitation deposited in the free OH is transferred to the bond stretch modes of OH groups that are weak hydrogen bond donors. Because vibrational relaxation of the free OH through IVR would require energy to leave the free OH stretch and move rapidly into the bend fundamental (i.e. well outside of our probe window) both of these observations thus suggest that IVR is relatively unimportant in describing free OH relaxation. Finally, we note that prior works have shown that the interfacial hydrogen bonded OH stretch shifts to higher frequencies when heated [13]. If vibrational relaxation and subsequent thermalization of the free OH excitation were sufficiently rapid we would expect to see a transient increase, rather than decrease and recovery, in the coupling trace. Clearly the data are inconsistent with such rapid thermalization.

This comparison between the free OH pump/free OH probe and free OH pump/weakly H-bonded OH probe traces thus suggests a picture in which a free OH group is initially excited and this excitation is either transferred to the hydrogen bonded OH group on the other half of the same molecule or the excited OH group rotates down and forms a hydrogen bond. Clearly, however, this is only the first part of the vibrational relaxation pathway. To investigate what happens next we performed two additional IR-pump/SFG-probe experiments: one in which weakly H-bonded OH groups are pumped and the free OH probed (blue trace in Fig. 4.4) and one in which weakly H-bonded OH groups are both pumped and probed (red trace in Fig. 4.4). Interestingly, these two signals (the two bleach amplitudes) are notably different: the bleach for the free OH is appreciably smaller than for the H-bonded OH probe. This difference suggests that, on excitation of weakly H-bonded OH groups some energy transfer likely occurs via IET or REOR to the higher energy free OH group while the rest, possibly through rapid intermolecular energy transfer to more strongly H-bonded OH stretches on other water molecules or IVR, dissipates through other channels.

Taken as a whole the data discussed thus far suggests that free OH vibrational relaxation proceeds by IET and REOR (but not IVR) and that there is an effective time

constant of $(1.24 \text{ ps})^{-1}$ associated with the IET pathway and $(2.6 \text{ ps})^{-1}$ with the REOR. As discussed above, these data further suggest that these time constants are a combination of forward and backward rates for both processes: an initially excited free OH group that has either reoriented to form a hydrogen bond or transferred its excitation to the hydrogen bonded OH group on the same molecule can either rotate back to become free or transfer its excitation back to the free OH on ultrafast time scales. We have previously shown in experiment and simulation that the characteristic time for a free OH to rotate towards bulk liquid and form a hydrogen bond is $\sim 1 \text{ ps}$ [26,98]. On the face of it the $(2.6 \text{ ps})^{-1}$ time constant associated with the REOR pathway appears to conflict with this previous observation. To explore whether the $(2.6 \text{ ps})^{-1}$ could be the result of this observable convoluting both forward and backward rates, we developed a model to account explicitly for the possibility of a return of the excitation to the free OH either because the newly hydrogen bond OH is once again free or because of excitation transfer back from a hydrogen bonded OH to the free OH on the same molecule.

To do so we first assume free OH vibrational relaxation occurs in two stages: a first step that is reversible and leads to an initially excited free OH group either becoming (through REOR) or transferring its excitation to (through IET) a weakly hydrogen bonded OH group, and a second step that describes the relaxation of the weakly hydrogen bonded OH group (with rate constant k_{HB}) and is non-reversible. The rate equation accounting for this vibrational relaxation processes is described as follows with the definition presented before [33]. The free OH groups are denoted as F , the hydrogen-bonded counterparts are denoted as HB , and the subsequent relaxation process from the hydrogen-bonded state into a state at somewhat elevated temperature is denoted as T . The vibrational mode transfer from free OH to H-bonded OH occurs at rate k_{VR}^f , while k_{VR}^b is the vibrational modes transfer rate for the inverse process (from H-bonded OH to free OH). “ f ” denotes the forward process and “ b ” denotes the backward process, respectively. We assume that vibrational relaxation with rate k_{HB} occurs from the HB state, rather than from the F state, into the T state. The occupation of each of the states is denoted as $N_X^{0,1}$, where $X=F, HB$ or T , and the superscript denotes ground (‘0’) or excited (‘1’) state.

When the free OH groups are excited, the excitation pulse, characterized by the time-dependent intensity $I(t)$, gives rise to population of N_F^1 , and the time dependent occupation numbers of states N_X follows the rate equations:

$$\begin{aligned}\frac{\partial N_F^1}{\partial t} &= \sigma_{01} I(t) [N_F^0 - N_F^1] - k_{VR}^f N_F^1 + k_{VR}^b N_{HB}^1 \\ \frac{\partial N_{HB}^1}{\partial t} &= k_{VR}^f N_F^1 - k_{VR}^b N_{HB}^1 - k_{HB} N_{HB}^1 \\ \frac{\partial N_T^0}{\partial t} &= k_{HB} N_{HB}^1\end{aligned}\quad (4.1)$$

When the H-bonded OH groups are excited, the equation leads to

$$\begin{aligned}\frac{\partial N_F^1}{\partial t} &= -k_{VR}^f N_F^1 + k_{VR}^b N_{HB}^1 \\ \frac{\partial N_{HB}^1}{\partial t} &= \sigma'_{01} I(t) [N_{HB}^0 - N_{HB}^1] + k_{VR}^f N_F^1 - k_{VR}^b N_{HB}^1 - k_{HB} N_{HB}^1 \\ \frac{\partial N_T^0}{\partial t} &= k_{HB} N_{HB}^1\end{aligned}\quad (4.2)$$

where σ_{01} and σ'_{01} represent the absorption cross-sections for the 0 to 1 transition of free OH and H-bonded OH stretching mode, respectively. Given such equations, we wish to ask whether the model can describe all data in Figure 4.4 simultaneously. The solid lines in Fig. 4.4 are the results of the model with transfer rate $k_{VR}^f = (460 \pm 50 \text{ fs})^{-1}$, $k_{VR}^b = (980 \pm 100 \text{ fs})^{-1}$, and $k_{HB} = (750 \text{ fs} \pm 80 \text{ fs})^{-1}$. The superscript “ f ” denotes the forward process (the excited vibrational stretching mode changes from the free OH to the H-bonded OH) and “ b ” denotes the backward process (the excited vibrational stretching mode changes from the H-bonded OH to the free OH).

As shown above, the excitation transfer from free to H-bonded OH groups, with the rate constant $k_{VR}^f = (460 \text{ fs})^{-1}$, is the sum of relaxation via IET (k_{IET}^f) and REOR (k_{REOR}^f): $k_{VR}^f = k_{IET}^f + k_{REOR}^f$. To solve for the backward rates of both processes, we assume that there is no energy barrier and the system is at equilibrium with respect to intramolecular energy transfer, i.e. the ratio of forward to backward rates of IET is related to the frequency difference between these modes, as described in an Arrhenius equation, and is $k_{IET}^f / k_{IET}^b = \exp[\hbar(3700 - 3500)/k_B T] = 2.6$ at $T = 300 \text{ K}$. To determine the ratio of the rate for the reorientational motion (REOR) of free OH to rotate down to the bulk and become hydrogen bonded (k_{REOR}^f)

and the H-bonded OH to break the hydrogen bond and become free OH (k_{REOR}^b), the relative populations of the free OH and H-bonded OH groups must be estimated. Figure 4.5 shows the axial distributions of water molecules at the water-vapor interface from the molecular dynamics simulation [99]. The 0-, 1-, and 2-DH water denote that the water with two free O-H groups, one free O-H group and one H-bonded donating H (DH) atom, and 2 DH atoms, respectively. The hydrogen bond definition is based on the electronic structure [103]. The grey rectangle represents the area we defined as interfacial water, starting from 10% to 90% of the bulk density. By integrating the amount of OH groups in this area, we get the ratio of 1.7 between the H-bonded OH and free OH groups. So if we assume that the relative number of interfacial hydrogen bonded OH groups does not change as a result of the IR pump, and given that the population of H-bonded OHs is 1.7 times larger than the population of free OHs, the reorientation rate for the H-bonded OH to break the hydrogen bond and become a free OH must be 1.7 times slower than the converse: $k_{REOR}^b = k_{REOR}^f / 1.7$. Substituting we find, for the free OH to H-bonded OH transition, $k_{VR}^f = k_{IET}^f + k_{REOR}^f = (460 \text{ fs})^{-1}$, and for the H-bonded OH to free OH $k_{VR}^b = k_{IET}^b + k_{REOR}^b = k_{IET}^f / 2.6 + k_{REOR}^f / 1.7 = (980 \text{ fs})^{-1}$. Rearranging terms leads to $k_{IET}^f = (800 \text{ fs})^{-1}$ and $k_{REOR}^f = (1.1 \text{ ps})^{-1}$. These time constants are summarized in Fig. 4.2. The 1.1-ps time constant for the reorientational motion of the free OH group and formation of a hydrogen bond thus appears to be consistent with our earlier estimates for the rate of this process [26,98].

To summarize, we have thus calculated the characteristic rate constant for free OH vibrational relaxation in two ways: a simple exponential fit and a rate model that solves the system of coupled differential equations describing population transfer in a three state model. Summing the forward and backward time constants for each process extracted from the rate model allows direct comparison to the exponential analysis offered above. We find that the time constant of vibrational relaxation of the free OH due to IET calculated using the rate model is $k_{IET}^f - k_{IET}^b = k_{IET}^f - k_{IET}^f / 2.6 = (1.3 \text{ ps})^{-1}$ and that due to REOR $k_{REOR}^f - k_{REOR}^b = k_{REOR}^f - k_{REOR}^f / 1.7 = (2.67 \text{ ps})^{-1}$. Clearly both time constants are in good agreement with the exponential description, in which $k_{REOR}^{(H_2O)} = (2.6 \text{ ps})^{-1}$ and $k_{IET}^{(H_2O)} = (1.24 \text{ ps})^{-1}$, offered above. Both ways of analyzing the data thus appear to reach a similar conclusion: about one-third of the vibrational relaxation of the free OHs in H₂O is due to structural relaxation with and the remaining two-thirds to intramolecular energy transfer.

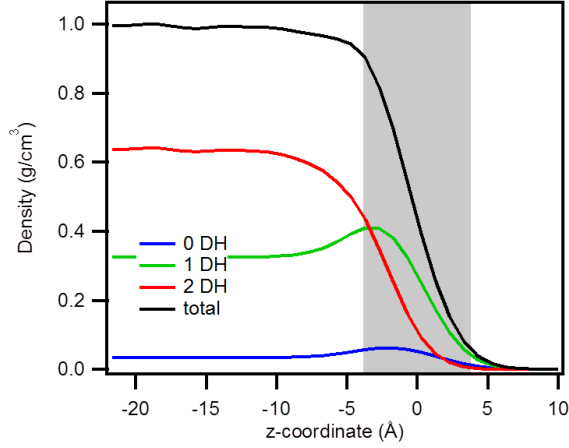


FIG. 4.5 Axial distribution for the density of water with different numbers of donor hydrogen atoms. The blue, green, red, and black traces denotes the axial distributions of water molecules with two free O-H groups, one free O-H group and one DH atom, 2 DH atoms, and the total water molecules, respectively.

As noted above, prior work suggests that, while inhomogeneous broadening is important in determining the hydrogen bonded OH spectral response at the air/water interface, it is relatively unimportant in understanding the free OH. This then implies that we are justified in describing the SFG spectral response of the free OH at both the air/H₂O and air/H₂O:HOD:D₂O interface using Eq. 1.18:

$$I_{SFG} \propto |\chi^{(2)}|^2 = \left| A_{NR} e^{i\phi_{NR}} + \sum_n \frac{A_n}{\omega_{IR} - \omega_n + i\Gamma_n} \right|^2 \quad (4.1)$$

where A_n , ω_n , and $2\Gamma_n$ are the amplitude, frequency, and full-width-at-half-maximum (FWHM), respectively, of mode n . Γ is related to the decay rate ($1/T_2$) of the polarization (induced by the IR pulse), $2\pi\Gamma = 1/T_2$, where T_2 is the homogeneous dephasing time. This homogeneous dephasing time can be decomposed into two contributions, $1/T_2 = 1/(2T_1) + 1/T_2^*$, where T_1 is the population lifetime and T_2^* is the pure dephasing time. The spectral fits in Fig. 4.6 indicate that the FWHM of the free OH is 48 cm^{-1} ($\Gamma = 24 \text{ cm}^{-1}$) for H₂O and 40 cm^{-1} ($\Gamma = 20 \text{ cm}^{-1}$) for HDO, i.e. a difference of 4 cm^{-1} in Γ . For H₂O the lifetime $T_1 = T_{H_2O} = 840 \text{ fs}$ results in a contribution of 3.2 cm^{-1} to Γ , while for HDO $T_1 = T_{HDO} = 2.6 \text{ ps}$ results in a contribution of only 1.0 cm^{-1} . Changes in T_1 thus explain only 2.2 cm^{-1} of the 4 cm^{-1} difference in Γ between the spectral response of the interfacial free OH of H₂O and that of HOD, the remaining 1.8 cm^{-1} must be due to differences in the pure dephasing time, T_2^* , of the two systems, presumably due to subtle differences in low frequency modes of the H-bonded network for the isotopologues. As expected, the pure dephasing times, T_2^* , of free OH

groups both for H₂O, ~ 250 fs, and HDO, ~ 280 fs, are 3 times longer than the H-bonded OH of HDO in bulk D₂O (~ 90 fs) [104], presumably due to the absence of the frequency modulation of free OH groups by the surrounding water molecules at the air/water interface.

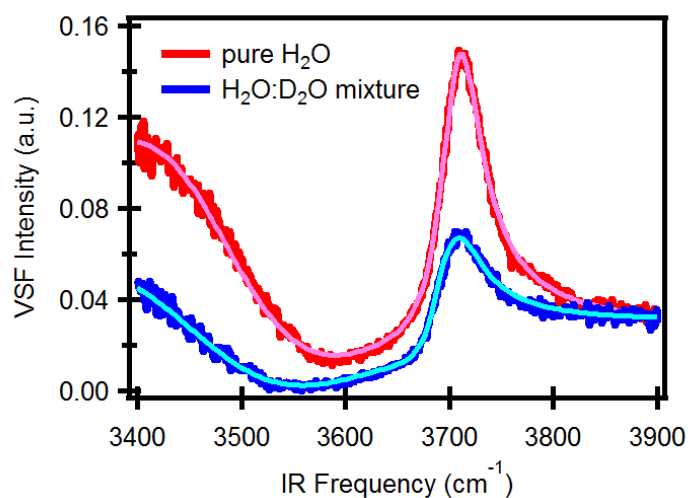


FIG. 4.6 SFG spectrum of pure (red) and isotopically diluted H₂O (H₂O:D₂O=1:1, blue) and their spectral fitting curves (pink and light blue).

4.4 Conclusion

In this study we show that free OH groups at the air/water interface have a vibrational lifetime of ~ 850 fs. Two color IR-pump/SFG-probe measurements of both the free OH of H₂O at the air/H₂O interface and of HOD at the air/H₂O:D₂O mixture interface allow us to clarify that one-third of this energy relaxation happens via structural relaxation, with the free OH rotating towards the bulk liquid at which point it forms a hydrogen bond, while two-thirds are the result of intramolecular energy transfer – excitation transfer from the excited free OH to the hydrogen bonded OH on the other half of the same molecule. Given this knowledge of lifetimes for both species, we further calculate pure dephasing times of 250 fs for free OHs in H₂O and 280 fs for HDO. Taken together this work allows us full insight into the SFG free OH spectral response at the air/water interface: we can now completely specify the factors that control the spectral line shape. Such insight, and similar experiments to those described here for other aqueous solutions, should be invaluable in quantitative description of the SFG OH stretch spectral response and, therefore, in understanding hydrophobic solvation.

Chapter 5

Ultrafast Vibrational Energy Transfer between Hydrogen-bonded OH groups at the Air/Water Interface Revealed by Two-Dimensional Phase-sensitive Surface Vibrational Spectroscopy

In chapters 3 and 4 we discussed the dynamics of the free OH groups at the air/water interface, including the reorientational motion and the mechanism of the vibrational relaxation. In the SFG spectrum of the air/water interface, the free OH corresponds to a peak centered at 3700 cm^{-1} with a homogeneous linewidth of 48 cm^{-1} . The presence of this free OH peak in the interfacial vibrational spectrum is very specific to the air/water interface (or other hydrophobic water interfaces), as it cannot be found in the IR spectrum of bulk water. In contrast, the broad band ranging from 3000 to 3600 cm^{-1} is caused by hydrogen-bonded (H-bonded) OH groups, which can be found in both the SFG spectra of the air/water interface and the IR spectra of bulk water [67,105]. Does this mean that the structure and dynamics of the H-bonded OH groups are similar between interfacial water and bulk water? While the vibrational spectra that reflect the linear vibrational response of the H-bonded OH groups of the interfacial water molecules (through SFG) and bulk water molecules (through linear IR absorption) are very similar, the underlying water structures as well as the dynamics may be very different. A specifically important quantity regarding the water dynamics that cannot be accessed with linear spectroscopic methods is spectral diffusion. Spectral diffusion is the phenomenon in which the vibrational frequency of an O-H group changes in the course of time. Spectral diffusion may be caused by rearrangement of the hydrogen bond network and/or vibrational energy transfer between O-H groups. These processes of interfacial water molecules can be characterized by combining two-dimensional (2D) vibrational approaches with surface specific spectroscopy.

In this chapter, we elucidate the vibrational relaxation and spectral diffusion of the H-bonded OH groups at the air/H₂O interface by using ultrafast 2D phase-sensitive vibrational sum-frequency generation spectroscopy (2D-PS-SFG). The measured 2D spectra reveal that the spectral diffusion of the strongly H-bonded OH groups ($< 3400\text{ cm}^{-1}$) occurs on a ~ 280 fs time scale. More weakly H-bonded OH groups at 3500 cm^{-1} (part of which are the hydrogen-

bonded parts of the water molecules that have an OH group sticking out) [97] show slower dynamics due to the decoupling of the intra-/intermolecular energy transfer.

5.1 Introduction

Since the first SFG spectra of aqueous interfaces were reported alongside the presence of the free OH groups at the air/water interface [13], many efforts have been made to extract microscopic structures of the interfacial water from the spectra. SFG measurements have been performed for several water/hydrophobic interfaces such as water/oil [52] and water/OTS [106] interfaces, where, compared to the air/water interface, the free OH peak is slightly red-shifted ($\sim 10 \text{ cm}^{-1}$ in the case of oil) due to the van der Waals interactions between the water free OH groups and the oil molecules. In addition to the free OH peak, the SFG spectra of the air/water interface contain the $3000 - 3500 \text{ cm}^{-1}$ OH stretch response from the H-bonded OH groups. This H-bonded OH stretch response also exists in the bulk water. However, since the breaking of the hydrogen bonds leads to different structures of the interfacial water from the bulk, where some H-bonded OH groups may share the same molecules with the free OH groups, these H-bonded OH groups may have distinct structural and energetic dynamics from those in the bulk.

In particular, it is still under debate whether the lower frequency part of the H-bonded OH response at $\sim 3100 \text{ cm}^{-1}$ in the IR absorption spectrum of bulk water has the same molecular origin as the $\sim 3100 \text{ cm}^{-1}$ feature of the SFG spectrum at the air/water interface. Since the IR absorption and SFG spectra are composed of the auto-correlation function of the transition dipole moment and the correlation function of the transition dipole moment and polarizability, respectively, the frequency dependence of the transition dipole moment and polarizability affects the IR and SFG signals in a different way. Molecular dynamics simulations have been carried out to reproduce the low frequency OH stretch peak by modifying the force field models and optical responses such as the electric dipole moment and polarizability. Morita and Ishiyama reexamined the effect of the short-range electrostatic interactions on the induced dipole moment and found that the anisotropic component of the polarizability affects the $\sim 3100 \text{ cm}^{-1}$ frequency mode [93], while Skinner and co-worker developed a novel robust three-body potential additive to the pairwise potential and showed that the three-body interaction is crucial for reproducing the interface structure [97]. Although these studies pointed out different molecular origins of the $\sim 3100 \text{ cm}^{-1}$ feature in the SFG spectra, both theories successfully reproduced the static SFG spectrum of the

air/water interface. Hence, it is apparent that additional spectroscopic observables may help differentiate between the different physical phenomena that have been predicted to give rise to the overall spectral response. The situation of a rather indistinct linear spectral response is reminiscent of the situation in bulk water, where linear infrared and Raman studies have revealed a very broad and featureless response. Higher-order nonlinear vibrational spectroscopies, and specifically two-dimensional infrared spectroscopy, have, for bulk water, provided much more insight into the origin of the vibrational spectrum, and how the spectral response is related to the structure and the structural dynamics of water. Clearly, the application of two-dimensional vibrational spectroscopy to the water interface would be very helpful in elucidating structure and dynamics of interfacial water.

With 2D-SFG spectroscopy, which enables us to selectively excite specific vibrational modes and probe others, the energy coupling between different modes and the homogeneity and heterogeneity of the interfacial molecules can be quantified. The first 2D-SFG experiment at the water/dodecanol interface probed the coupling between the CH₂ and CH₃ stretching modes of the dodecanol molecules [31]. Later this technique was applied to the air/D₂O interface, which clarified the rapid inter-/intramolecular vibrational energy transfer of the OD stretching mode of interfacial D₂O molecules [33]. The fourth-order optical response in the 2D-SFG process includes two vibrational transitions; the transitions from the vibrational ground state to the first excited state ($\nu = 0 \rightarrow 1$) and from the first excited state to the second excited state ($\nu = 1 \rightarrow 2$). For conventional 2D-SFG experiments however, the contribution of the $0 \rightarrow 1$ transition cannot be distinguished from that of the $1 \rightarrow 2$ transition due to the interference of $\chi^{(4)}$ and $\chi^{(2)}$, as discussed in chapter 1, resulting in substantial ambiguity in the slope analysis. In addition, the non-resonant background gives additional contribution to the 2D spectra, which complicates quantitative analysis. In contrast, the 2D-PS-SFG can overcome these difficulties. Since the peaks in 2D-PS spectra for the $0 \rightarrow 1$ and $1 \rightarrow 2$ transitions show opposite signs, these peaks interfere and a nodal line appears between these peaks, providing a well-defined slope as shown in 2D-IR spectra [107]. Also the non-resonant contribution is removed from the 2D-PS-SFG spectra. Zanni and coworkers reported the first 2D-PS-SFG spectra [34], and sequentially Tahara and coworkers conducted the 2D-PS-SFG experiment at the air/water interface with a positively charged surfactant [35]. On the simulation side, Nagata *et.al.* performed the first simulation of 2D-SFG spectra at the lipid/water interface [108], and Skinner and coworkers demonstrated that the reorientational motion and hydrogen bond dynamics of the air/HDO interface can be extracted from 2D-SFG

spectroscopy and showed that the hydrogen bond rearranges within a few picoseconds [80]. However, the 2D-PS-SFG spectra of the air/water interface have not been obtained experimentally, presumably due to the challenges associated with the small SFG signal at the air/water interface.

In this chapter, we present 2D-PS-SFG experiments at the air/H₂O interface in the 3000-3600 cm⁻¹ range. The 2D spectra of the H-bonded OH stretching mode show that the weakly H-bonded OH groups (3500 cm⁻¹) shows slower spectral diffusion, while the OH stretching mode with strongly H-bonded OH groups (3000-3400 cm⁻¹) shows faster spectral diffusion. This spectral feature is different from the 2DIR spectra in neat H₂O in which the spectral diffusion was concluded to be uniform in the frequency region of <3500 cm⁻¹ [67]. Our results clearly illustrate that interfacial water is rather heterogeneous at the air/water interface, which provides further evidence that the 3500 cm⁻¹ peak originates from the H-bonded OH groups which share the same water molecule with the free OH groups. Therefore these OH groups are decoupled from the bending overtone which terminates the intramolecular coupling. Also, the intermolecular coupling slows down due to the lower degree of hydrogen bond coordination at the interface, resulting in a slower dynamics than other H-bonded OH groups.

5.2 Experimental section

The 2D-PS-SFG experimental setup is described in detail in sections 2.2.2 and 2.2.3 of chapter 2. The narrow-band IR pump pulse with a bandwidth of 100 cm⁻¹ was tuned from 3100, 3200, 3300, 3400 to 3500 cm⁻¹ by changing the angle of the KTP crystal to excite H-bonded OH groups and create the 2D plot. The broad-band IR probe pulse ranging from 3000 to 3600 cm⁻¹ was used to probe the response of the OH stretching modes within this frequency region. The samples were distilled Millipore filtered H₂O (18MΩ-cm resistivity). The IR-pump/SFG-probe data were recorded under *pssp* (IR pump/VSF, VIS probe, IR probe) polarization. The interference fringes were computed to obtain Im[χ⁽²⁾] at each delay, which was described in section 1.5. The Im[χ⁽²⁾] spectra were normalized to that of quartz, which was recorded under the same experimental condition as the samples. The differential PS-SFG signal Im[χ⁽²⁾] (Δ Im[χ⁽²⁾]) was computed as the difference between the normalized Im[χ⁽²⁾] spectra with and without the pump.

5.3 Results and discussion

5.3.1 Differential $\text{Im}[\chi^{(2)}]$ spectra

Figure 5.1(a) shows the $\text{Im}[\chi^{(2)}]$ spectrum of the H-bonded OH stretching mode at the air/H₂O interface (red curve). The spectrum shows a broad negative peak from 3150 to 3500 cm^{-1} and a small positive peak below 3150 cm^{-1} as reported [109,110]. The positive (negative) sign of $\text{Im}[\chi^{(2)}]$ indicates the transition dipole moment associated with the OH stretching vibrations [97] and/or the induced dipole moment via anisotropic component of the polarizability [110] pointing up (down) towards the air (the bulk water), respectively.

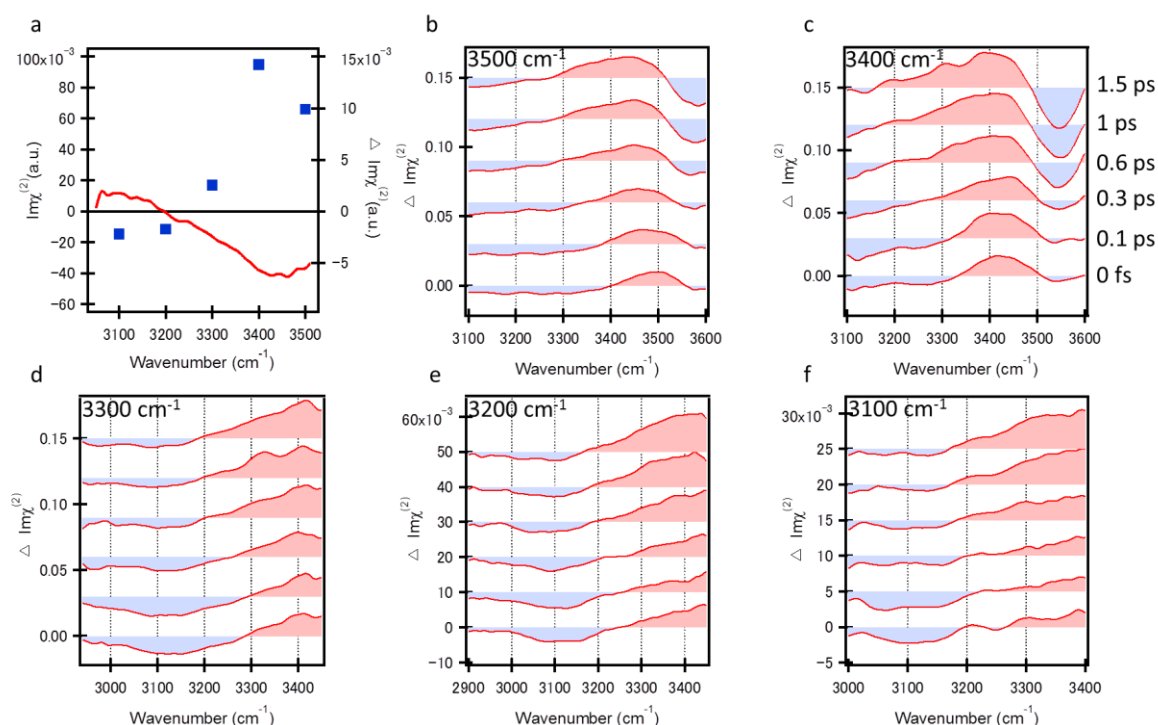


FIG. 5.1 (a) Steady-state $\text{Im}[\chi^{(2)}]$ spectrum (red curve) and the $\Delta \text{Im}[\chi^{(2)}]$ at 0 fs with the excitation frequency equal to the detection frequency (blue dots) of the air/water interface. (b)-(f) Femtosecond time-resolved $\Delta \text{Im}[\chi^{(2)}]$ spectra of the OH stretching modes at the air/water interface. Delay times after excitation are 0, 100, 300, 600, 1000, and 1500 fs and the pump frequencies are (b) 3500, (c) 3400, (d) 3300, (e) 3200, and (f) 3100 cm^{-1} .

Figures 5.1(b) - (f) show the femtosecond time-resolved differential PS-SFG signal $\Delta \text{Im}[\chi^{(2)}(t)]$ (where $\Delta \text{Im}[\chi^{(2)}(t)] = \text{Im}[\chi_{\text{pump-on}}^{(2)}(t)] - \text{Im}[\chi_{\text{pump-off}}^{(2)}(t)]$) spectra of the air/water interface which were measured at $t = 0, 100, 300, 600, 1000,$ and 1500 fs with five different IR pump frequencies of 3500, 3400, 3300, 3200, and 3100 cm^{-1} , where t is the time delay between the IR pump pulse and the SFG probe pulse. When the IR pump excites the OH

stretching mode from the ground state ($\nu_{\text{OH}} = 0$) to the first vibrationally excited state ($\nu_{\text{OH}} = 1$), we can observe a bleach in the PS-SFG signal at the $0 \rightarrow 1$ transition frequency and an induced increase in the signal at the $1 \rightarrow 2$ transition frequency, where $\nu_{\text{OH}} = 2$ denotes the second vibrationally excited state. For the OH stretching mode, the $1 \rightarrow 2$ transition frequency is $\sim 200 - 250 \text{ cm}^{-1}$ lower than the $0 \rightarrow 1$ transition frequency due to its large anharmonicity. However, PS-SFG spectra contain both negative and positive peaks in contrast to the IR spectra, complicating the signs of $\Delta \text{Im}[\chi^{(2)}]$ for the $0 \rightarrow 1$ and $1 \rightarrow 2$ transitions; when the $\text{Im}[\chi^{(2)}]$ spectrum is positive (negative), a negative (positive) sign of the $\Delta \text{Im}[\chi^{(2)}]$ spectrum represents a bleach and positive (negative) sign represents an increase in the signals. For example, Fig. 5.1(b) ($\Delta \text{Im}[\chi^{(2)}(t = 0)]$ with the IR pump frequency of 3500 cm^{-1}) shows a positive band in the region of 3400 cm^{-1} to 3550 cm^{-1} and a negative band below 3400 cm^{-1} . This can be accounted for as follows: Since the steady-state $\text{Im}[\chi^{(2)}]$ shows a negative feature at $\sim 3500 \text{ cm}^{-1}$, the positive band in the $\Delta \text{Im}[\chi^{(2)}]$ corresponds to the induced bleach of the excited vibration from the ground state to the first excited state ($\nu_{\text{OH}} = 0 \rightarrow 1$ transition). Since the orientation of OH transition dipole moment from $\nu_{\text{OH}} = 1$ to $\nu_{\text{OH}} = 2$ is approximately the same as that from $\nu_{\text{OH}} = 0$ to $\nu_{\text{OH}} = 1$, the negative band below 3400 cm^{-1} can be assigned to be the resonance of the broad hot band ($\nu_{\text{OH}} = 1 \rightarrow 2$ transition). In this manner, we can clearly separate the $0 \rightarrow 1$ and $1 \rightarrow 2$ transitions by using 2D-PS-SFG, enabling us to extract the dynamics of the interfacial molecules from the 2D spectra. As the time evolves from 0 to 1.5 ps, the positive band shifts from 3500 cm^{-1} to 3400 cm^{-1} with a broader bandwidth, which arises from the spectral diffusion and heating of the water molecules. The spectrum at 1.5 ps with negative bands in the blue and red wings (above 3500 cm^{-1} and below 3300 cm^{-1}) and a positive band in between indicates a blueshift from the original steady-state $\text{Im}[\chi^{(2)}]$ spectrum, which can be attributed to the thermalized ground state. The pump energy has been transferred into heat and leads to the thermalization of the water, which weakens the hydrogen bond and causes the blueshift of the SFG signal [13]. Figures 5.1(c) - (f) show the $\Delta \text{Im}[\chi^{(2)}]$ spectra pumped at the other frequencies. Among the five different pump frequencies, the $\Delta \text{Im}[\chi^{(2)}]$ signal of the bleach at 0 fs and the heated ground state at 1.5 ps are the largest for pumping at 3400 cm^{-1} and smallest for pumping at 3100 cm^{-1} , which originates from the different population intensities of each frequency and leads to different absorption efficiency of the IR pump power. For the data pumped at 3400 cm^{-1} and 3100 cm^{-1} , we can

see a bleach at the pumped frequency at 0 fs. Note here that the negative band below 3300 cm^{-1} in Fig. 5.1(c) is attributed to the $\nu_{\text{OH}} = 1 \rightarrow 2$ transition, while for Fig. 5.1(f) it originates from $\nu_{\text{OH}} = 0 \rightarrow 1$ transition. However, as seen in Fig. 5.1(d) and 5.1(e), the frequency where the maximum bleach is observed does not coincide with the pump frequency of 3200 cm^{-1} and 3300 cm^{-1} , and is centered at $\sim 3100 - 3150 \text{ cm}^{-1}$ at 0 fs. This may be due to the fact that the zero crossing of the $\text{Im}[\chi^{(4)}]$ spectrum of the air/water interface is at $\sim 3200 - 3300 \text{ cm}^{-1}$, as shown with the blue dots in Fig. 5.1(a). Also, as we can see in Fig. 5.1, the heated ground state at 1.5 ps shows the similar feature for each pump frequency except for 3500 cm^{-1} . This different thermalization dynamics originates from the different spectral diffusion mechanism of the H-bonded OH groups. While the lower frequencies show a more homogeneous behavior for spectral diffusion, the 3500 cm^{-1} OH stretch mode, which originates from the OH groups that share the same water molecules with the free OHs, displays slower dynamics.

5.3.2 2D-PS-SFG spectra

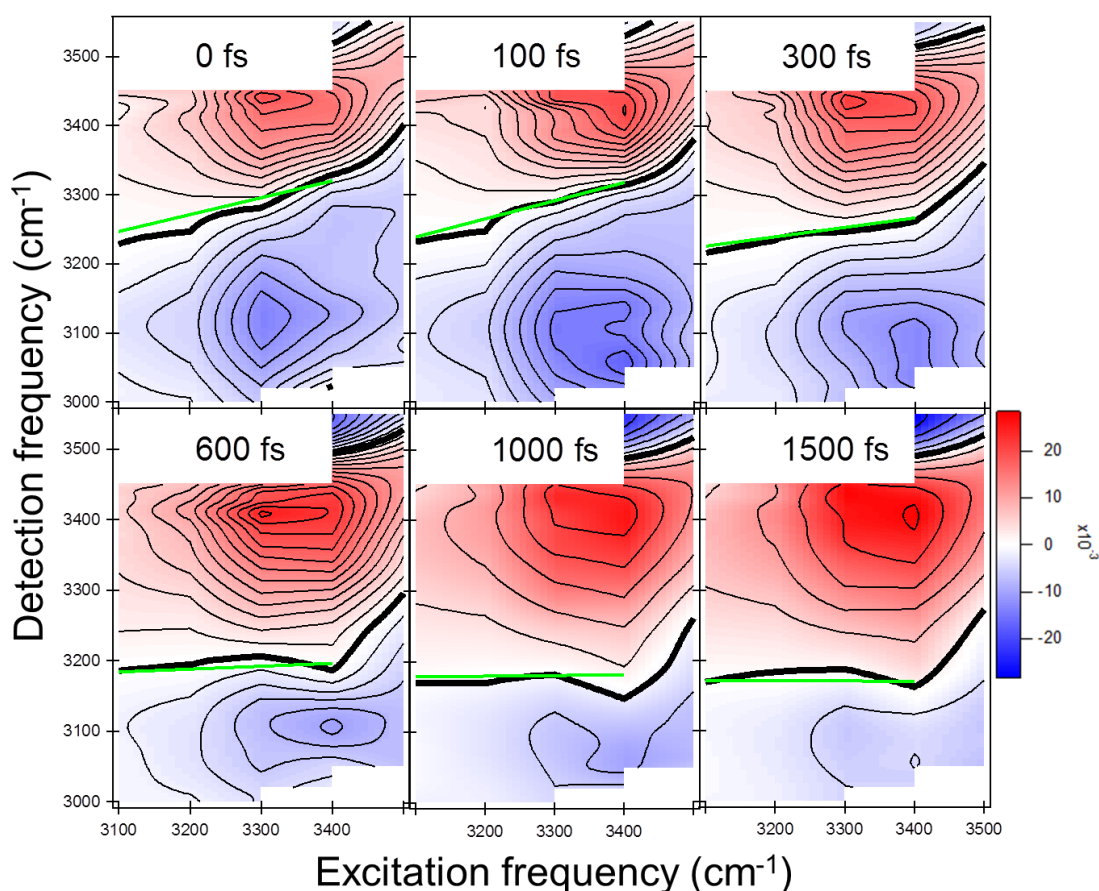


FIG. 5.2 2D-PS-SFG spectra of the air/water interface which corresponds to the pump-probe delay time of 0, 100, 300, 600, 1000, and 1500 fs.

This heterogeneity of interfacial water molecules at the air/water interface can be addressed in the 2D-PS-SFG plots. Figure 5.2 displays the 2D-PS-SFG spectra of interfacial H₂O molecules for waiting times of $t = 0, 100, 300, 600, 1000, 1500$ fs. First we consider the 2D plot at $t = 0$ fs. The diagonal intensities (excitation frequency = detection frequency) for the 2D plot $\Delta \text{Im}[\chi^{(2)}]$ are plotted as blue dots in Fig. 5.1(a). The sign of the diagonal cuts is roughly opposite to the steady-state $\text{Im}[\chi^{(2)}]$ spectrum, which indicates the bleach indeed originates from the 0 \rightarrow 1 excitation [80]. The thick black curves in Fig. 5.2 indicate the nodal curves separating the positive and negative peaks in the 2D contour plots. Note that in the 2D-PS-SFG, the nodal curves arise from not only the interference between the 0 \rightarrow 1 and 1 \rightarrow 2 transitions as in the 2D-IR spectra, but also from the interference of the positive and negative bands of the $\Delta \text{Im}[\chi^{(2)}]$ spectra. Nevertheless, we can still evaluate the heterogeneity of the OH stretching modes at the air/H₂O interface with the slope of the nodal curves. The slope of the nodal line decreasing to zero in time reflects that the system “forgot” at which frequency the initial excitation occurred; when the slope approaches zero, the excitation has been completely scrambled in frequency space. This relaxation can occur through either the structural rearrangement of the H-bonded OH groups (causing OH groups to change their vibrational frequencies), and/or energy transfer between O-H groups with different vibrational frequencies. The green lines in Fig. 5.2 represent linear fits to the nodal curves in the $\Delta \text{Im}[\chi^{(2)}]$ signals at excitation frequencies ranging from 3100 to 3400 cm⁻¹ extracted from the nodal points of Fig. 5.1, while the time evolution of the gradient of the nodal curve (slope) is plotted in Fig. 5.3. The time variation of the slope exhibits the slope decay with a time constant of 280 ± 80 fs. This decay of the slope is caused by spectral diffusion and/or thermalization of the water molecules. As will be shown in the next section, the thermalization of the water molecules which originates from the excess energy of the 3300 cm⁻¹ pump pulse occurs on a 460-fs time scale, which means that the spectral diffusion of the H-bonded OH stretch with frequency < 3400 cm⁻¹ occurs at roughly the same time scale. Compared to bulk water, the spectral diffusion of the H-bonded OH stretching mode at the air/H₂O interface is slower than in pure bulk H₂O (~ 180 fs) [67,105,111], but faster than for HDO in D₂O (0.5 - 1 ps) [112–115]. Since less density of the OH chromophores leads to the slower spectral diffusion, the density of water molecules at the air/water interface is lower than the bulk, slowing down the spectral diffusion. It is worth mentioning that the spectral diffusion of the OH stretch at the air/H₂O interface is much faster than that of the OD stretch at the air/D₂O interface [33]. In contrast, the time evolution of the nodal slopes between 3400

and 3500 cm^{-1} shows a significantly slower decay. This clearly illustrates that different spectral diffusion mechanisms govern the OH stretching modes at 3500 cm^{-1} and at $3000\text{--}3400\text{ cm}^{-1}$, which will be discussed below.

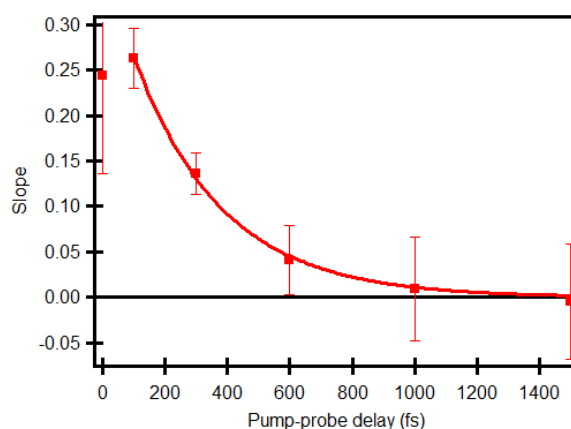


FIG. 5.3 The slopes of the green line in Fig. 5.2 as a function of pump-probe delay. The fitting curve shows a decay time of 280 ± 80 fs.

5.3.3 Vibrational relaxation of H-bonded OH groups

The vibrational energy relaxation of the H-bonded OH groups and the ingrowth of the signal due to heating the air/water interface can be readily extracted from the time evolution of the $\Delta \text{Im}[\chi^{(2)}]$ signals. Figure 5.4 shows the IR-pump/PS-SFG probe data for the excitation at (a) 3500 cm^{-1} , and (b) 3300 cm^{-1} and 3100 cm^{-1} . In Fig. 5.4(a), three traces represent the data with different detection frequencies. The red trace shows the dynamics of the $0 \rightarrow 1$ transition (probing at 3500 cm^{-1}) and the blue one shows that of the $1 \rightarrow 2$ transition (probing at 3200 cm^{-1}). With a monoexponential fitting, the two traces show time constants of 700 ± 50 fs for the $0 \rightarrow 1$ transition and 750 ± 70 fs for the $1 \rightarrow 2$ transition. These time constants are indistinguishable within the experimental error, which strongly suggests that the time constant of the vibrational relaxation (T_1) of the 3500 cm^{-1} OH stretching mode is ~ 750 fs. The green trace with the probing frequency of 3400 cm^{-1} shows no bleach at 0 fs, which indicates that the ingrowth of the signal originates solely from the thermalization of water molecules with a time constant (τ_{eq}) of 880 ± 30 fs. For H-bonded OH groups with a vibrational frequency lower than 3500 cm^{-1} , the dynamics is significantly accelerated. Figure 5.4(b) shows the data for excitation of strongly H-bonded OH stretching mode. The red and green traces are the data with pump pulses centered at 3300 cm^{-1} . The red trace represents the time evolution when probing at 3300 cm^{-1} , but instead of the vibrational energy relaxation of the $0 \rightarrow 1$ transition, these data show the heat ingrowth with a time constant of 460 ± 30 fs.

The reason is that at 3300 cm^{-1} no bleach occurs due to the cancellation of the positive and negative bands. On the other hand, the green curve (pump at 3300 cm^{-1} and probe at 3100 cm^{-1}) does reflect vibrational relaxation, as it represents the time evolution of the $1\rightarrow 2$ transition of the 3300 cm^{-1} H-bonded OH groups with a time constant of 240 ± 20 fs. The blue trace with a recovery rate of 160 ± 30 fs indicates the vibrational relaxation of the 3100 cm^{-1} H-bonded OH groups. These time constants are summarized in table 5.1, from which one can see that vibrational energy relaxation strongly depends on the pump frequency. Hereafter, the time traces of the 3100 , 3300 , and 3500 cm^{-1} are individually discussed and the molecular origin of the dynamics is clarified.

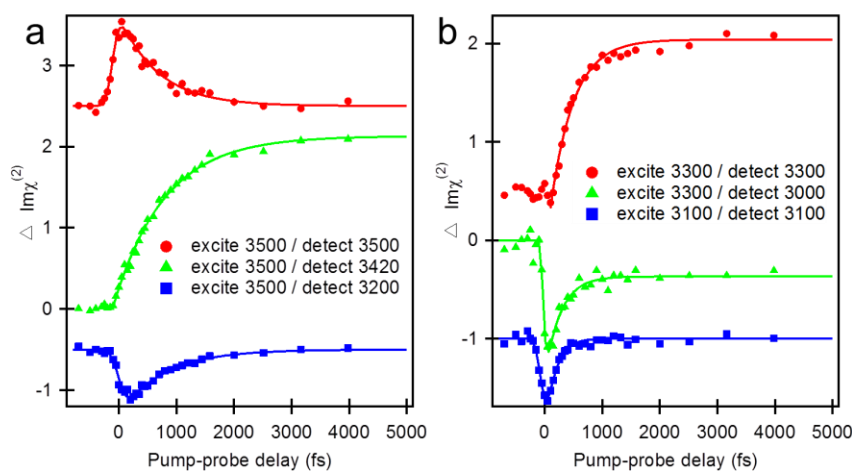


FIG. 5.4 Dynamics of the resonance of the H-bonded OH groups of interfacial water molecules. (a) Excitation at 3500 cm^{-1} , detection at 3500 cm^{-1} ($0\rightarrow 1$ transition, red), 3400 cm^{-1} (green), and 3200 cm^{-1} ($1\rightarrow 2$ transition, blue). (b) Excitation at 3300 cm^{-1} , detection at 3300 cm^{-1} ($0\rightarrow 1$ transition, red) and 3000 cm^{-1} ($1\rightarrow 2$ transition, green). Excitation at 3100 cm^{-1} , detection at 3100 cm^{-1} ($0\rightarrow 1$ transition, blue).

TABLE. 5.1 The time constant of the vibrational relaxation and thermalization in pure H_2O of H-bonded OH groups with frequencies at 3500 , 3300 , and 3100 cm^{-1} .

Pump wavelength (cm^{-1})	Lifetime for pure H_2O T_1 (fs)	Thermalization time constant in pure H_2O τ_{eq} (fs)
3500	750 ± 70	880 ± 30
3300	240 ± 20	460 ± 30
3100	160 ± 30	

First we consider the OH stretch at 3500 cm^{-1} . This OH stretch mode shows slower dynamics for vibrational relaxation and thermal ingrowth compared with the H-bonded OH groups with lower frequencies. Prior work has shown that this frequency range corresponds

to the OH stretch of the hydrogen bonded half of a water molecule that contains a free OH group [102]. Therefore this OH stretching mode has a reduced number of hydrogen bond coordinates, which slows down the dissipating of energy through the intermolecular energy transfer. Also there is large energy mismatch between this OH stretch and the bending overtone, whose fundamental frequency is $\sim 1660 \text{ cm}^{-1}$ [99]. Therefore the slowing down of the intra-/intermolecular energy transfer leads to the longer lifetime of the 3500 cm^{-1} OH stretch. Remarkably, the lifetime of the 3500 cm^{-1} OH stretch mode is the same as that of the O-H stretch of HDO molecules in bulk D_2O solution (740 fs) [44,47]. This indicates that the OH stretch at 3500 cm^{-1} is largely decoupled from the vibrational modes of other water molecules.

Second we consider the H-bonded OH groups with lower frequencies (3300 and 3100 cm^{-1}). The 3300 cm^{-1} OH stretch has a similar lifetime as bulk water (260 fs) [42], presumably because of the predominance of the intramolecular vibrational relaxation channel of the excited population to the intermediate level for both cases: The 3300 cm^{-1} OH stretch overlaps with the overtone of the bending mode whose fundamental frequency is ~ 1650 - 1690 cm^{-1} [99,116] at the air/water interface in a similar manner to the bulk water.

On the other hand, this intramolecular coupling mechanism is insufficient to explain the ultrafast vibrational relaxation of the 3100 cm^{-1} OH stretch, since the frequency of the 3100 cm^{-1} OH stretch mode does not match the frequency of the bending mode overtone at $\sim 3300 \text{ cm}^{-1}$. Surprisingly, the 160-fs lifetime of the 3100 cm^{-1} OH groups of the interfacial water molecules is faster than that in the bulk H_2O [42]. The molecular origin of the 3100 cm^{-1} SFG peak has been discussed in the theoretical/simulation approaches; Morita and co-workers have attributed the peak's origin to the induced dipole moment via the off-diagonal element of the molecular anisotropy [93], while Skinner and co-workers state that many-body interactions, that is, more than pairwise interactions, produce the positive 3100 cm^{-1} feature [97]. In other words, the Morita interpretation implies that the optical response from the collective motion is essential for the 3100 cm^{-1} peak, unlike bulk water, while the Skinner interpretation implies that the 3100 cm^{-1} peak is caused by strongly hydrogen bonded OH groups, which are also present in bulk water. Our data shows that the relaxation of the water molecules at 3100 cm^{-1} occurs appreciably faster than in the bulk. This 'non-bulk-like' behavior of interfacial water molecules at 3100 cm^{-1} can (in part) be due to the reduced spectral diffusion at the interface [33]. Spectral diffusion leads to excursions of the excited OH group to higher frequencies, where relaxation is slowed down, and back to lower

frequencies where relaxation is more efficient. Alternatively, if spectral diffusion is less important, our data tentatively supports the Morita interpretation for the 3100 cm^{-1} SFG peak. From the dynamics first observed in this report, thus, it is unveiled that water molecules at the interface are inhomogeneous, reflecting the inhomogeneity of the hydrogen-bonding network.

Besides the vibrational relaxation, the manner in which thermalization of interfacial water molecules occurs is also different from that in the bulk. As shown in Table 5.1, $\tau_{\text{eq}} = 880 \pm 30$ for the 3500 cm^{-1} OH stretch mode is faster than that of energetically isolated OH groups in water, namely of HDO molecules in D_2O , for which $\tau_{\text{eq}} = 1\text{ ps}$ [44], while the 460 ± 30 timescale observed for the 3300 cm^{-1} OH stretch mode is also faster than bulk H_2O at that frequency (550 fs) [42]. We tentatively attribute the faster thermalization of interfacial water to the relative ease with which water can expand at the interface, compared to the bulk: heating resulting from thermalization extends the average distance between molecules and increases the volume of the water. Whereas in the bulk expansion requires displacing water on all sides, the interfacial water can readily expand in the direction of the air, leading to a faster thermalization process.

5.4 Conclusion

In summary, by using a novel 2D-PS-SFG setup we investigate the vibrational energy relaxation and spectral diffusion of the H-bonded OH stretching modes at the air/water interface. The 2D-PS-SFG ($\Delta \text{Im}[\chi^{(2)}]$) spectra, which contain the orientation information of the interfacial OH groups, reveal the very different behavior of the 3500 cm^{-1} OH stretching mode compared with the strongly H-bonded OH stretching modes with frequencies $< 3400\text{ cm}^{-1}$. This difference is not obvious from static $\text{Im}[\chi^{(2)}]$ spectra, illustrating the strength of the approach presented here. Our results clearly indicate that the weakly H-bonded OH stretching mode is more heterogeneous at the air/water interface than in the bulk. This heterogeneous nature of the 3500 cm^{-1} OH stretching mode originates from the structural difference between the interfacial water and bulk water, where the 3500 cm^{-1} OH groups share the same water molecule with the free OH while the other H-bonded OH groups are more bulk like. Due to the decoupling of the intra-/intermolecular energy transfer, the 3500 cm^{-1} OH groups show slower spectral diffusion and vibrational relaxation behavior than other OH groups.

Chapter 6

Probing the Generation and Propagation of Shock Waves at the Air/Liquid Interface Using Sum Frequency Generation Spectroscopy

In the previous chapters, we employed time-resolved SFG experiments to survey the microscopic structure and ultrafast dynamics of water. The IR pump pulses were used to excite the molecular vibrations and the probe pulse was used to detect the response of the system to this perturbation. On the other hand, pump pulses can also be used to excite a quasi-instantaneous decrease in water density through a temperature jump, resulting in a shockwave that can propagate into the bulk. Here, we investigate the generation and propagation of shock waves at the air-aqueous solution interface using time-resolved SFG spectroscopy. The SFG field radiated away from the air/liquid interface interferes with the field transmitted into the bulk, which is partially reflected from the IR pump-induced shock wave front. Because the effective path length of the reflected beam increases with time, the interference leads to time-dependent sinusoidal oscillations of the SFG signals. The oscillation periods of the SFG signals provide information on the sound velocity in the liquid. Interestingly, depending on the details of the aqueous solution under study, we observe large variations in the phase difference between the directly reflected SFG light and that reflected from the wave front. These different phase shifts are tentatively attributed to the different interfacial water structures which originate from different surface activities of halide ions at the interface.

6.1 Introduction

Shock waves are fast mechanical transients generated by sudden compression of the material, causing a weak leading edge followed by a stronger, faster trailing edge, which constitutes the shock front [117]. The investigation of shock waves provides information on the hydrodynamic properties of the bulk medium such as the flow of pressure, temperature, and density. Pulsed lasers provide not only a simple means to initiate the shock wave at a well-defined moment, they also allow one to control its momentum and to synchronize the shock wave with a wide variety of optical and electronic diagnostics, enabling, e.g. the detailed

study of the mechanism of shock wave generation. There are several mechanisms by which shock waves can be generated using laser pulses [118], but in all cases the surface plays a pivotal role. Hence the chemical and physical properties of the surface in steady state and during the generation and evolution of the shock wave are particularly important. Owing to its surface specificity, femtosecond time resolution, and molecular sensitivity, SFG spectroscopy [13] has proven to be a very useful and valuable tool for detecting the molecular structures at interfaces during shock wave generation. For example, it has been used to demonstrate that hydrocarbon chains at a metal surface tilt as a result of shock waves being launched from that surface [119].

In addition to the purpose of investigating the effects of the shock wave on the orientation of molecules, time-resolved SFG has been used to track the vibrational energy relaxation at interfaces, where intense pulses are employed to excite a significant fraction (typically $\sim 10\%$) of specific molecular vibrations at the interface, to follow interfacial vibrational relaxation in real time, as shown in chapters 3, 4, and 5. The vibrational relaxation is then monitored by (weaker) probe pulses, which are generally sensitive to the ground state population of the molecular vibrations. Since the SFG signal typically originates specifically from surface molecules, SFG spectroscopy is frequently used to probe the vibrational dynamics in the outermost molecular layer of the bulk material [23,24,26,84]. Clearly, if the lifetimes of the relevant vibrational states are short-lived (which is typically the case for condensed phase materials), the excess vibrational energy will be converted to low-frequency vibrations and ultimately heat will be released at the interface on very short timescales, which is precisely the requirement for launching a shock wave. Although the shock wave can create an asymmetric dielectric environment, and SFG is sensitive to broken symmetry, it has not yet been determined how the generation of the shock wave may affect the time-dependent SFG signals. Here, we investigate the generation and propagation of shock waves using IR-pump/SFG-probe spectroscopy at different air-aqueous sodium halide solutions interfaces. The surface activities of the different halide ions and their effect on the orientation of interfacial water molecules are known to depend on the size and polarizability of the halide ion. The modulation of the microscopic structure of the water interface by ions has been addressed previously: Theoretically, MD simulations have shown that larger anions with larger polarizabilities are enriched at the air-water interface [120]. Experimentally, SFG spectra show that large anions cause significant distortion of the surface hydrogen-bonding network [121]. However it is unclear whether, and to what extent, these different surface

activities of ions will affect the generation and detection of shock waves from the different aqueous interfaces.

In this chapter, we discuss the experimental observation of shock waves launched at aqueous surfaces, detected by large time-dependent, oscillatory variations in the SFG signals generated from these interfaces following vibrational excitation. These oscillations are characterized by their amplitude, phase and oscillation time. The phase is found to be a function of the solute, and is presumably related to the different interfacial water structures for different solutes; the period of the oscillation of the IR-pump/SFG-probe signals is determined by the speed with which the shock wave propagates from the surface into the bulk, which in turn is determined by the bulk density [122,123] .

6.2 Experimental section

The one-color TR-SFG experimental setup is described in detail in chapter 2, section 2.2.2 and 2.2.3. The samples were NaI, NaBr, NaCl, and NaF dissolved in distilled Millipore filtered water (18M Ω -cm resistivity) or D₂O (Cambridge Isotope Laboratories, Inc., 99.93% purity, used without further purification) with a mole fraction of 0.036x (corresponding to a molarity of 2.07M) for NaI, NaBr, and NaCl and 0.015x (0.84M) for NaF. The samples were placed in a homemade Teflon trough which was rotated at 8 rpm to reduce cumulative heating. The IR-pump/SFG-probe spectra were recorded under *p/ssp* (IR pump/SFG, VIS probe, IR probe) polarization conditions. The IR pump pulse was variably delayed with respect to the SFG probe signal using a mechanical delay line. The normalized IR-pump/SFG-probe is defined as the ratio between the integrated intensities with and without the pump.

6.3 Results and discussion

To investigate the generation and propagation of the shock wave from the surface into the bulk phase, IR-pump/SFG-probe experiments with different sodium halide solutions have been performed. The results are shown in Fig. 6.1, from pure H₂O, NaF, NaCl, NaBr, to NaI solution, in the order of increasing size of halide anions. In the experiments, the O-H stretch vibrations of water are excited at 3350 cm⁻¹ with an intense excitation pulse, and the effect of the excitation is probed with the time-delayed SFG probe pair, probing the O-H stretch vibrations, also at 3350 cm⁻¹. On very short time scales (within 2 ps), the normalized SFG

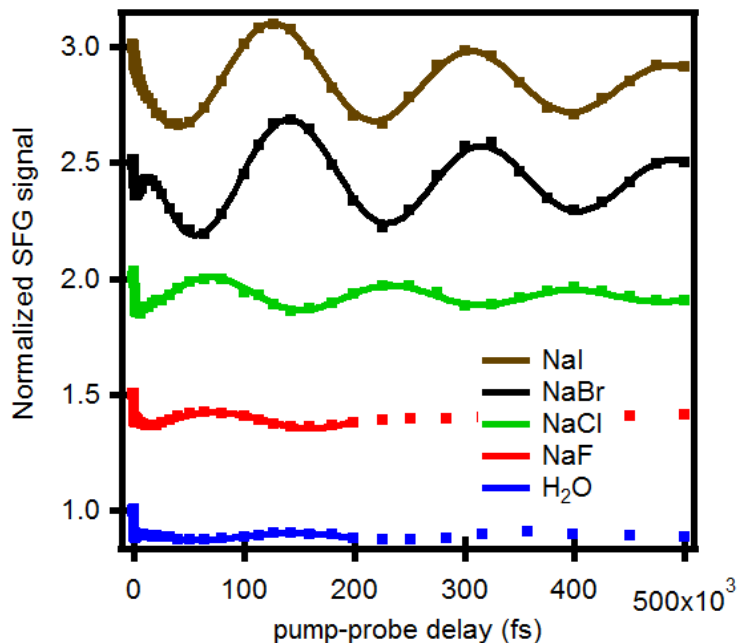


FIG. 6.1 IR-pump/SFG-probe data for hydrogen-bonded OH at air/water interface for various sodium halide solutions, from pure H₂O, NaF, NaCl, NaBr, to NaI solution, in the order of the size of halide anions. The IR pump and IR probe are both at 3350cm⁻¹. The solid lines are the fitting curves with a damped sinusoidal oscillation model. Data are offset by multiples of 0.5 for clarity.

TABLE 6.1 The period of oscillation (τ) and the phase shift ($\Delta\phi$) of IR-pump/SFG-probe data for different sodium halide solutes in H₂O solvents. The phase shift is defined relative to the negative sine wave.

solution	Period of oscillation τ (ps)	Phase shift $\Delta\phi$ (rad)
0.036x-NaI	179±1	0.18±0.02
0.036x-NaBr	174±1	-0.45±0.03
0.036x-NaCl	164±2	1.96±0.05
0.015x-NaF	174±4	2.05±0.09
Pure H ₂ O	182±3	-0.36±0.06

signals show transient bleaches, due to the excitation of the population from the ground to the first excited state. After 10 ps, these data show oscillatory features which are damped on a timescale of several nanoseconds. The solid traces are fitting curves with a damped sinusoidal oscillation model, i.e. $I(t) = -e^{-(t/T)} \sin(t/\tau + \Delta\phi) + A$, where T is a time constant of the exponential decay function, τ is the oscillation period, $\Delta\phi$ is the phase shift related to the negative sine wave, and A is the offset of the signal. The fit parameters are listed in Table 6.1. The oscillation periods τ of these traces are nearly the same (~ 175 ps), which are not sensitive to

the halide ion species, while the phase shift differs from solution to solution. The amplitude of the oscillation increases as the size of the anions increases. This is attributed to the fact that NaBr and NaI aqueous solutions have strong enrichment of halide anions at the interfaces compared to the bulk, causing significant amount of charge to be present at the surface with a corresponding distortion of the H-bonding network and an enhancement of the SFG signals, while the interfacial water structures for NaF and NaCl aqueous solutions are roughly the same as the air-water interface [121]. To elucidate the origin of the observed oscillations, we investigated several properties of these oscillatory SFG signals.

Figure 6.2(a) shows the result of a power-dependent experiment, where Fig. 6.2(b) displays the amplitude of the oscillation versus IR pump power. As the IR pump energy is reduced from 21 through 14 to 7 μJ per pulse, the amplitudes of the oscillations decrease proportionally, while the periods remain unchanged. This indicates that the density change of the shock wave front, which is roughly proportional to the refractive index change [124], is proportional to the incident IR pump power. However, as we changed the concentration of NaI solutions from 0.012x, 0.025x, to 0.036x, the properties of the oscillations remain unchanged, both for the amplitudes and the periods, which implies that at these ion concentrations, the surface is saturated with halide ions (Fig. 6.3).

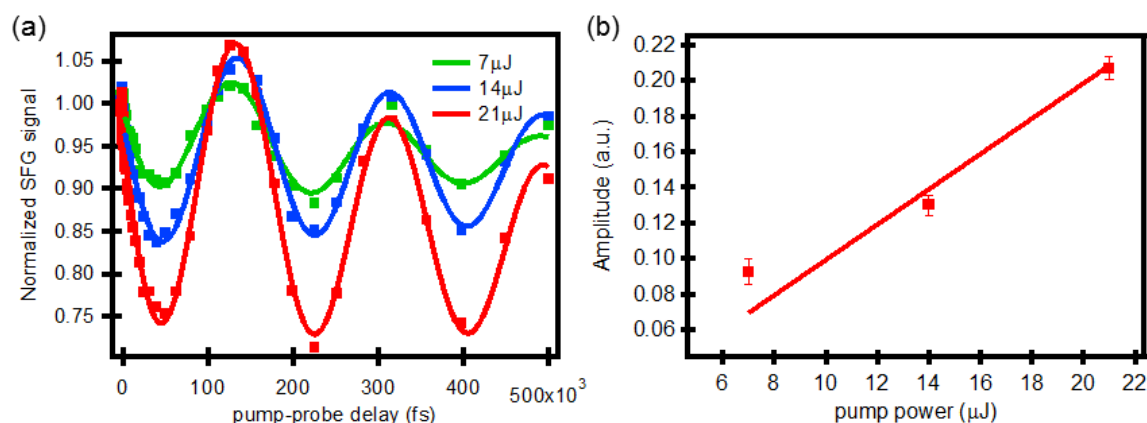


FIG. 6.2 (a) Pump-probe data with pump power of 21, 14, and 7 μJ , respectively. (b) The amplitudes of the oscillations versus the IR pump power. The amplitude of the oscillation is proportional to the pump power.

The oscillation period is also influenced by the incident angle of the IR probe and VIS probe beams. Figure 6.4 shows the IR-pump/SFG-probe traces of 0.036x NaI solution with two different incident angles for the probe pulse pair. The red data are obtained with incident angles of IR probe = 37.0° and VIS probe = 42.9° , which leads to a reflective angle of 41.7° and a refractive angle of 30.1° of the SFG signal. The blue data are obtained with the incident

angles of IR probe = 44.6° and VIS probe = 50.4° , which leads to a reflective angle of 49.2° and a refractive angle of 34.8° of the SFG signal. The oscillation period for the red trace is 175 ± 1 ps, and for the blue one is 183 ± 1 ps. The ratio of the periods of the two traces (0.956) is close to the ratio of $\sec \theta$ (0.949), where θ is the refractive angle of the SFG signal.

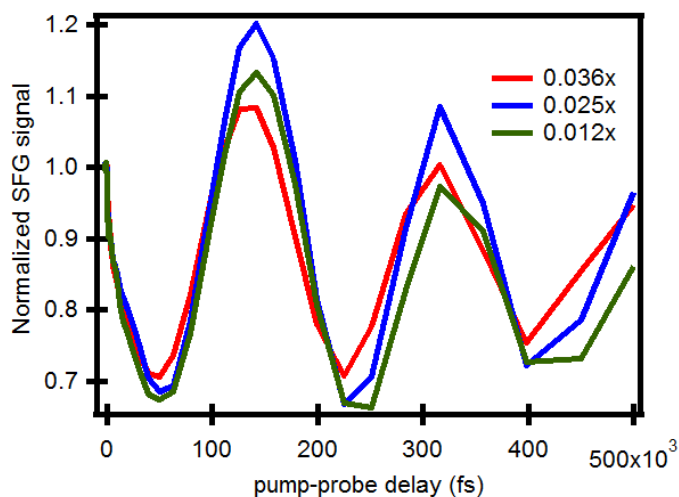


FIG. 6.3 Pump-probe data with different concentrations of NaI solution. The amplitude and the oscillation period are roughly the same for 0.036x, 0.024x, and 0.012x NaI solutions.

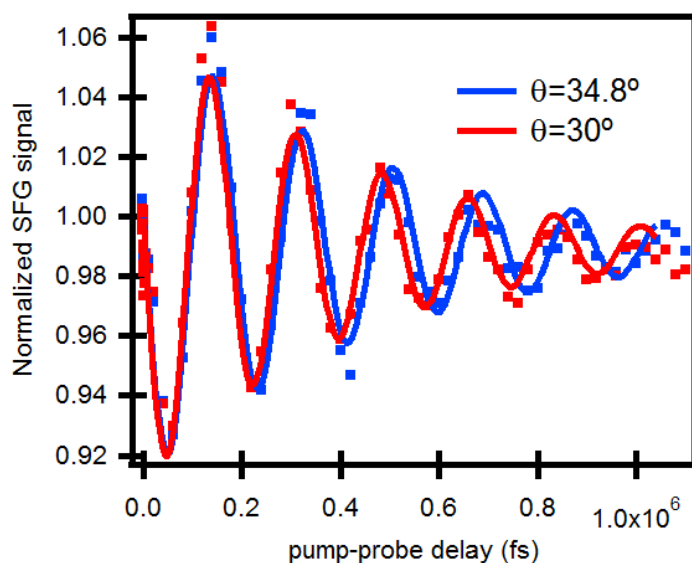


FIG. 6.4 Pump-probe data with different incident angles of IR/VIS probe. The period of the oscillation is proportional to $\sec \theta$, where θ is the refractive angle of the SFG signal.

The oscillation is also affected by the properties of the solvent. Figure 6.5 shows the IR-pump/SFG-probe traces of 0.036x NaI solution in H_2O (red curve) and D_2O (blue curve). For NaI in H_2O solution, the IR pump and probe are both at 3350 cm^{-1} , which leads to a 634.6

nm SFG signal. For NaI in D₂O solution, the IR pump and probe are both at 2500 cm⁻¹, which generates the SFG signal at 670.5 nm. The acoustic velocities are 1498 m/s for H₂O and 1400 m/s for D₂O, while the oscillation periods are 177±1 ps for H₂O (denoted by red curve) and 193±2 ps for D₂O (denoted by blue curves). This indicates that the oscillation period is roughly proportional to the probe SFG wavelength over the acoustic velocity of the liquid.

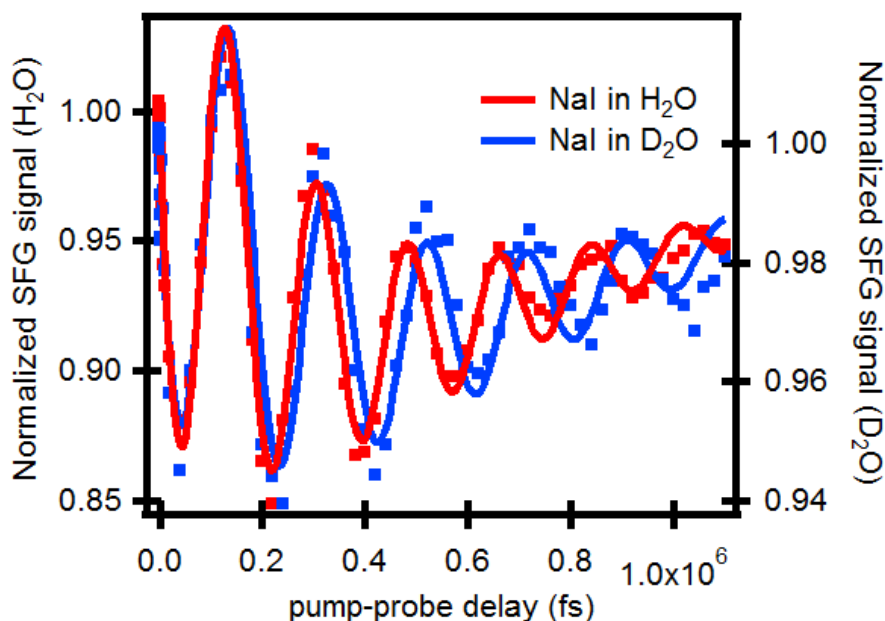


FIG. 6.5 Pump-probe data for NaI in H₂O and D₂O solvents. The period of the oscillation is proportional to the acoustic velocity of the solution.

As shown above, the amplitude of the oscillation is influenced by the intensity of the pump pulse, while the period is affected by the incident angle of the incoming beam, the wavelength of the SFG signal, and the sound velocity of the aqueous solutions. We conclude from these properties that the oscillation of the IR-pump/SFG-probe signal originates from the following mechanism. As shown in Figure 6.6, the IR pump pulse ramps up, heats the solution and creates a gradual shock front. The compression wave front propagates into the bulk solution and travels with acoustic velocity v . The VIS/IR probe pulses generate the probe SFG signal at the air/solution interface. Due to the refractive index mismatch, part of the SFG signal directly reflects from the surface (d-SFG) while the rest is transmitted into the bulk phase. The transmitted SFG signal is partially reflected from the compression pulse wave front (r-SFG) due to the density difference between the wave front and the surrounding environment. The oscillations in the SFG signal intensity can therefore be attributed to the interference of two SFG signals: the SFG signal directly originating from the interface (d-

SFG) and the one reflected from the compression wave (r-SFG). While theoretically an SFG signal could also be generated at the wavefront interface, this mechanism can be excluded, since the penetration depth of the infrared radiation into the bulk is very limited; in that case much stronger damping would be observed.

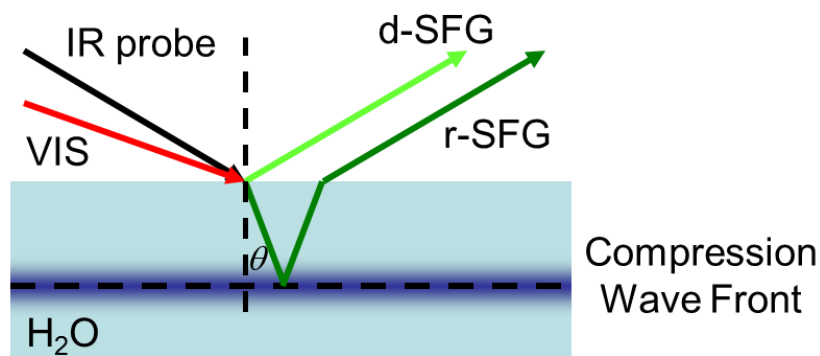


FIG. 6.6 Schematic diagram of the experiment. The compression wave front in the liquid is produced by the IR pump pulse. The SFG signal generated by the VIS and IR probe pulses partially reflects from the surface (d-SFG) while the rest transmits into the bulk and reflects from the compression wave front (r-SFG). The oscillation originates from the interference between d-SFG and r-SFG.

The optical path difference between d-SFG and r-SFG is $2Ln(\omega)\cos\theta$, where L is the distance between the air/water interface and the shock wave front, $n(\omega)$ is the refractive index of water at frequency ω , and θ is the angle of refraction of the SFG signal. $L = v \times t$, where v is the acoustic velocity of the solution and t is the time interval after the shock wave is launched. During one period of the acoustic oscillation, the optical path change of the probe SFG signal reflected by the sound pulse is equal to the wavelength of the probe SFG signal, so $\tau = \lambda / 2vncos\theta$, where τ is the period of the oscillation signal and λ is the wavelength of the SFG signal. With our experimental geometry, where the incident angles of IR probe = 44.6° and VIS probe = 50.4° , which leads to 34.8° of refractive angle of the SFG signal, and the wavelength of IR probe = 3350 cm^{-1} and VIS probe = 806 nm , which leads to the SFG signal of 634.6 nm , and the acoustic velocity and the refractive index of H_2O are 1496 m/s and 1.33 , respectively, the oscillation period of H_2O is calculated to be 194 ps . From Table 6.1 it is apparent that the period of each solution is approximately the same as calculated, while the phase shift differs from solution to solution. This phase shift is due to the initial phase difference between d-SFG and r-SFG at 0 fs , when the shock wave is launched. The NaI, NaBr, and pure water have phase shift around 0 rad , while the NaCl and NaF are around 2 rads . One possible explanation is that due to the higher surface activity of larger halide anions,

the local electric field created by layers of cations and anions is enhanced, and the bulk contribution (electric-quadrupole and magnetic-dipole contributions) is enlarged. Since the reflected and transmitted SFG signals are influenced by the electric-quadrupole and magnetic-dipole contributions [125], this could explain the phase shift differences between solutions.

6.4 Conclusion

We have shown that, with IR-pump/SFG-probe spectroscopy, we can elucidate the generation and propagation of shock waves at the interface. The oscillations of the normalized SFG signals originate from the interference of the reflective SFG signals from the air-liquid interface and the shock wave front. The period of these oscillations are proportional to the sound velocity of the aqueous solution, which is roughly the same for H₂O, NaF, NaCl, NaBr, and NaI solutions. The phase shift of the oscillation is attributed to originate from the electric-quadrupole and magnetic-dipole contributions of the bulk phase.

Bibliography

- [1] K. B. Eisenthal, *Chem. Rev.* **106**, 1462 (2006).
- [2] H. Arnolds and M. Bonn, *Surf. Sci. Rep.* **65**, 45 (2010).
- [3] A. Fujishima and K. Honda, *Nature* **238**, 37 (1972).
- [4] R. Imbihl and G. Ertl, *Chem. Rev.* **95**, 697 (1995).
- [5] B. Meyer and D. Marx, *Phys. Rev. B* **67**, 035403 (2003).
- [6] N. Erdman, K. R. Poeppelmeier, M. Asta, O. Warschkow, D. E. Ellis, and L. D. Marks, *Nature* **419**, 55 (2002).
- [7] J. Kim and G. A. Somorjai, *J. Am. Chem. Soc* **125**, 3150 (2003).
- [8] S. Gopalakrishnan, D. Liu, H. C. Allen, M. Kuo, and M. J. Shultz, *Chem. Rev.* **106**, 1155 (2006).
- [9] A. M. Jubb, W. Hua, and H. C. Allen, *Annu. Rev. Phys. Chem.* **63**, 107 (2012).
- [10] L. Fu, J. Liu, and E. C. Y. Yan, *J. Am. Chem. Soc* **133**, 8094 (2011).
- [11] J. Wang, X. Chen, M. L. Clarke, and Z. Chen, *Proc. Natl. Acad. Sci. U.S.A.* **102**, 4978 (2005).
- [12] W. Michalak, J. Krier, K. Komvopoulos, and G. A. Somorjai, *J. Phys. Chem. C* **117**, 1809 (2013).
- [13] Q. Du, R. Superfine, E. Freysz, and Y. R. Shen, *Phys. Rev. Lett.* **70**, 2313 (1993).
- [14] H. J. Bakker and J. L. Skinner, *Chem. Rev.* **110**, 1498 (2010).
- [15] J. J. Gilijamse, A. J. Lock, and H. J. Bakker, *Proc. Natl. Acad. Sci. U.S.A.* **102**, 3202 (2005).
- [16] Y. L. A. Rezus and H. J. Bakker, *Proc. Natl. Acad. Sci. U.S.A.* **103**, 18417 (2006).
- [17] R. W. Boyd, *Nonlinear Optics*, third (Academic Press, New York, 2008).
- [18] X. Zhuang, P. Miranda, D. Kim, and Y. Shen, *Phys. Rev. B* **59**, 12632 (1999).
- [19] T. F. Heinz, *Nonlinear Surface Electromagnetic Phenomena* (North-Holland, 1991), pp. 353–416.

- [20] B. Busson and A. Tadjeddine, *J. Phys. Chem. C* **113**, 21895 (2009).
- [21] X. Wei and Y. Shen, *Phys. Rev. Lett.* **86**, 4799 (2001).
- [22] P. Guyot-Sionnest, *Phys. Rev. Lett.* **66**, 1489 (1991).
- [23] J. A. McGuire and Y. R. Shen, *Science* **313**, 1945 (2006).
- [24] M. Smits, A. Ghosh, M. Sterrer, M. Müller, and M. Bonn, *Phys. Rev. Lett.* **98**, 098302 (2007).
- [25] J. R. Schmidt, S. A. Corcelli, and J. L. Skinner, *J. Chem. Phys.* **123**, 044513 (2005).
- [26] C.-S. Hsieh, R. K. Campen, A. C. Vila Verde, P. Bolhuis, H.-K. Nienhuys, and M. Bonn, *Phys. Rev. Lett.* **107**, 116102 (2011).
- [27] H.-K. Nienhuys and M. Bonn, *J. Phys. Chem. B* **113**, 7564 (2009).
- [28] A. Ghosh, M. Smits, M. Sovago, J. Bredenbeck, M. Muller, and M. Bonn, *Chem. Phys.* **350**, 23 (2008).
- [29] A. Ghosh, M. Smits, J. Bredenbeck, and M. Bonn, *J. Am. Chem. Soc* **129**, 9608 (2007).
- [30] A. Ghosh, R. K. Campen, M. Sovago, and M. Bonn, *Faraday Discuss.* **141**, 145 (2009).
- [31] J. Bredenbeck, A. Ghosh, M. Smits, and M. Bonn, *J. Am. Chem. Soc* **130**, 2152 (2008).
- [32] A. Ghosh, M. Smits, J. Bredenbeck, N. Dijkhuizen, and M. Bonn, *Rev. Sci. Instrum.* **79**, 093907 (2008).
- [33] Z. Zhang, L. Piatkowski, H. J. Bakker, and M. Bonn, *Nat. Chem.* **3**, 888 (2011).
- [34] W. Xiong, J. E. Laaser, R. D. Mehlenbacher, and M. T. Zanni, *Proc. Natl. Acad. Sci. U.S.A.* **108**, 20902 (2011).
- [35] P. C. Singh, S. Nihonyanagi, S. Yamaguchi, and T. Tahara, *J. Chem. Phys.* **137**, 094706 (2012).
- [36] N. Bloembergen and P. S. Pershan, *Phys. Rev.* **128**, 606 (1962).
- [37] K. Kemnitz, K. Bhattacharyya, J. Hicks, G. Pinto, K. Eissenthal, and T. Heinz, *Chem. Phys. Lett.* **131**, 285 (1986).
- [38] Q. Du, E. Freysz, and Y. R. Shen, *Science* **264**, 826 (1994).
- [39] Y. Shen, *Nature* **337**, 519 (1989).
- [40] S. Yamamoto, A. Ghosh, H.-K. Nienhuys, and M. Bonn, *Phys. Chem. Chem. Phys.* **12**, 12909 (2010).

- [41] M. Bonn, H. J. Bakker, A. Ghosh, S. Yamamoto, M. Sovago, and R. K. Campen, *J. Am. Chem. Soc.* **107**, 1 (2010).
- [42] A. J. Lock and H. J. Bakker, *J. Chem. Phys.* **117**, 1708 (2002).
- [43] A. Lock, S. Woutersen, and H. Bakker, *J. Phys. Chem. A* **105**, 1238 (2001).
- [44] H.-K. Nienhuys, S. Woutersen, R. A. van Santen, and H. J. Bakker, *J. Chem. Phys.* **111**, 1494 (1999).
- [45] N. Huse, S. Ashihara, E. T. J. Nibbering, and T. Elsaesser, *Chem. Phys. Lett.* **404**, 389 (2005).
- [46] S. Ashihara, N. Huse, A. Espagne, E. Nibbering, and T. Elsaesser, *Chem. Phys. Lett.* **424**, 66 (2006).
- [47] S. Woutersen, U. Emmerichs, and H. Bakker, *Science* **278**, 658 (1997).
- [48] I. V. Stiopkin, C. Weeraman, P. A. Pieniazek, F. Y. Shalhout, J. L. Skinner, and A. V. Benderskii, *Nature* **474**, 1 (2011).
- [49] G. Richmond, *Annu. Rev. Phys. Chem.* **52**, 357 (2001).
- [50] J. Penfold, *Rep. Prog. Phys.* **64**, 777 (2001).
- [51] T. D. Kühne, T. a. Pascal, E. Kaxiras, and Y. Jung, *J. Phys. Chem. Lett.* **2**, 105 (2011).
- [52] L. F. Scatena, M. G. Brown, and G. L. Richmond, *Science* **292**, 908 (2001).
- [53] D. Chandler, *Nature* **437**, 640 (2005).
- [54] R. Godawat, S. N. Jamadagni, and S. Garde, *Proc. Natl. Acad. Sci. U.S.A.* **106**, 15119 (2009).
- [55] J. Qvist and B. Halle, *J. Am. Chem. Soc.* 10345 (2008).
- [56] D. Laage, G. Stirnemann, and J. T. Hynes, *J. Phys. Chem. B* **113**, 2428 (2009).
- [57] K.-J. Tielrooij, J. Hunger, R. Buchner, M. Bonn, and H. J. Bakker, *J. Am. Chem. Soc.* **132**, 15671 (2010).
- [58] G. Stirnemann, P. Rossky, J. Hynes, and D. Laage, *Faraday Discuss.* **146**, 263 (2010).
- [59] A. Eftekhari-Bafrooei and E. Borguet, *J. Am. Chem. Soc.* **131**, 12034 (2009).
- [60] W. Gan, D. Wu, Z. Zhang, R. Feng, and H. Wang, *J. Chem. Phys.* **124**, 114705 (2006).
- [61] Z. Gengeliczki, D. E. Rosenfeld, and M. Fayer, *J. Chem. Phys.* **132**, 244703 (2010).

- [62] H. J. C. Berendsen, J. R. Grigera, and T. P. Straatsma, *J. Phys. Chem.* **91**, 6269 (1987).
- [63] J. C. Phillips, R. Braun, W. Wang, J. Gumbart, E. Tajkhorshid, E. Villa, C. Chipot, R. D. Skeel, L. Kalé, and K. Schulten, *J. Comput. Chem.* **26**, 1781 (2005).
- [64] W. Humphrey, A. Dalke, and K. Schulten, *J. Mol. Graph.* **14**, 33 (1996).
- [65] M. Mazza, N. Giovambattista, H. Stanley, and F. Starr, *Phys. Rev. E* **76**, 031203 (2007).
- [66] M. Mazza, N. Giovambattista, F. Starr, and H. Stanley, *Phys. Rev. Lett.* **96**, 057803 (2006).
- [67] D. Kraemer, M. L. Cowan, A. Paarmann, N. Huse, E. T. J. Nibbering, T. Elsaesser, and R. J. D. Miller, *Proc. Natl. Acad. Sci. U.S.A.* **105**, 437 (2008).
- [68] S. Woutersen and H. J. Bakker, *Nature* **402**, 507 (1999).
- [69] D. Laage and J. T. Hynes, *Science* **311**, 832 (2006).
- [70] D. Laage and J. T. Hynes, *J. Phys. Chem. B* **112**, 14230 (2008).
- [71] P. Debye, *Polar Molecules* (Dover Publications, Inc., New York, NY, 1929).
- [72] H. C. Berg, *Random Walks in Biology* (Princeton University Press, Princeton, New Jersey, 1993).
- [73] R. Metzler and J. Klafter, *Phys. Rep.* **339**, 1 (2000).
- [74] A. Vila Verde and R. K. Campen, *J. Phys. Chem. B* **115**, 7069 (2011).
- [75] L. Piatkowski, K. B. Eisenthal, and H. J. Bakker, *Phys. Chem. Chem. Phys.* **11**, 9033 (2009).
- [76] K. Ramasesha, S. T. Roberts, R. A. Nicodemus, A. Mandal, and A. Tokmakoff, *J. Chem. Phys.* **135**, 054509 (2011).
- [77] J. B. Asbury, T. Steinle, K. Kwak, S. A. Corcelli, C. P. Lawrence, J. L. Skinner, and M. D. Fayer, *J. Chem. Phys.* **121**, 12431 (2004).
- [78] E. T. J. Nibbering and T. Elsaesser, *Chem. Rev.* **104**, 1887 (2004).
- [79] R. Rey, K. B. Møller, and J. T. Hynes, *Chem. Rev.* **104**, 1915 (2004).
- [80] Y. Ni, S. M. Gruenbaum, and J. L. Skinner, *Proc. Natl. Acad. Sci. U.S.A.* **110**, 1992 (2013).
- [81] B. J. Finlayson-Pitts and J. James N. Pitts, *Chemistry of the Upper and Lower Atmosphere: Theory, Experiments, and Applications* (Academic Press, 1999).

- [82] J. J. H. Pijpers, M. T. Winkler, Y. Surendranath, T. Buonassisi, and D. G. Nocera, *Proc. Natl. Acad. Sci. U.S.A.* **108**, 10056 (2011).
- [83] M. Smits, A. Ghosh, J. Bredenbeck, S. Yamamoto, M. Müller, and M. Bonn, *New J. Phys.* **9**, 390 (2007).
- [84] A. Eftekhari-Bafrooei and E. Borguet, *J. Am. Chem. Soc.* **132**, 3756 (2010).
- [85] Z. Zhang, L. Piatkowski, H. Bakker, and M. Bonn, *Nat. Chem.* **3**, 1 (2011).
- [86] Y. Nagata, R. E. Pool, E. H. G. Backus, and M. Bonn, *Phys. Rev. Lett.* **109**, 226101 (2012).
- [87] E. A. Raymond, T. L. Tarbuck, M. G. Brown, and G. L. Richmond, *J. Phys. Chem. B* **107**, 546 (2003).
- [88] G. L. Richmond, *Chem. Rev.* **102**, 2693 (2002).
- [89] R. S. Taylor, L. X. Dang, and B. C. Garrett, *J. Phys. Chem.* **100**, 11720 (1996).
- [90] M. D. Baer, C. J. Mundy, M. J. McGrath, I.-F. W. Kuo, J. I. Siepmann, and D. J. Tobias, *J. Chem. Phys.* **135**, 124712 (2011).
- [91] T. Ishiyama, H. Takahashi, and A. Morita, *Phys. Rev. B* **86**, 035408 (2012).
- [92] S. J. Byrnes, P. L. Geissler, and Y. R. Shen, *Chem. Phys. Lett.* **516**, 115 (2011).
- [93] T. Ishiyama and A. Morita, *J. Phys. Chem. C* **113**, 16299 (2009).
- [94] W.-K. Zhang, D.-S. Zheng, Y.-Y. Xu, H.-T. Bian, Y. Guo, and H.-F. Wang, *J. Chem. Phys.* **123**, 224713 (2005).
- [95] M. Sovago, R. K. Campen, G. W. H. Wurpel, M. Müller, H. J. Bakker, and M. Bonn, *Phys. Rev. Lett.* **100**, 173901 (2008).
- [96] S. T. Roberts, K. Ramasesha, and A. Tokmakoff, *Accounts Chem. Res.* **42**, 1239 (2009).
- [97] P. A. Pieniazek, C. J. Tainter, and J. L. Skinner, *J. Am. Chem. Soc.* **133**, 10360 (2011).
- [98] A. Vila Verde, P. G. Bolhuis, and R. K. Campen, *J. Phys. Chem. B* **116**, 9467 (2012).
- [99] Y. Nagata, C.-S. Hsieh, T. Hasegawa, J. Voll, E. H. G. Backus, and M. Bonn, *J. Phys. Chem. Lett.* **4**, 1872 (2013).
- [100] O. F. A. Larsen and S. Woutersen, *J. Chem. Phys.* **121**, 12143 (2004).
- [101] P. Bodis, O. F. A. Larsen, and S. Woutersen, *J. Phys. Chem. A* **109**, 5303 (2005).

- [102] P. A. Pieniazek, C. J. Tainter, and J. L. Skinner, *J. Chem. Phys.* **135**, 044701 (2011).
- [103] R. Kumar, J. R. Schmidt, and J. L. Skinner, *J. Chem. Phys.* **126**, 204107 (2007).
- [104] J. Stenger, D. Madsen, P. Hamm, E. Nibbering, and T. Elsaesser, *Phys. Rev. Lett.* **87**, 027401 (2001).
- [105] M. L. Cowan, B. D. Bruner, N. Huse, J. R. Dwyer, B. Chugh, E. T. J. Nibbering, T. Elsaesser, and R. J. D. Miller, *Nature* **434**, 199 (2005).
- [106] C. S. Tian and Y. R. Shen, *Proc. Natl. Acad. Sci. U.S.A.* **106**, 15148 (2009).
- [107] M. Koziński, S. Garrett-Roe, and P. Hamm, *Chem. Phys.* **341**, 5 (2007).
- [108] Y. Nagata and S. Mukamel, *J. Am. Chem. Soc.* **133**, 3276 (2011).
- [109] C. S. Tian and Y. R. Shen, *J. Am. Chem. Soc.* **131**, 2790 (2009).
- [110] S. Nihonyanagi, T. Ishiyama, T.-K. Lee, S. Yamaguchi, M. Bonn, A. Morita, and T. Tahara, *J. Am. Chem. Soc.* **133**, 16875 (2011).
- [111] K. Ramasesha, L. De Marco, A. Mandal, and A. Tokmakoff, *Nat. Chem.* **5**, 935 (2013).
- [112] G. Gale, G. Gallot, F. Hache, N. Lascoux, S. Bratos, and J. C. Leicknam, *Phys. Rev. Lett.* **82**, 1068 (1999).
- [113] C. P. Lawrence and J. L. Skinner, *J. Chem. Phys.* **118**, 264 (2003).
- [114] G. Gallot, N. Lascoux, and G. Gale, *Chem. Phys. Lett.* **341**, 535 (2001).
- [115] C. Fecko, J. Eaves, J. Loparo, A. Tokmakoff, and P. Geissler, *Science* **301**, 1698 (2003).
- [116] M. Vinaykin and A. Benderskii, *J. Phys. Chem. Lett.* **3**, 3348 (2012).
- [117] D. D. Dlott, *Annu. Rev. Phys. Chem.* **62**, 575 (2011).
- [118] S. Panchatsharam, B. Tan, and K. Venkatakrisnan, *J. App. Phys.* **105**, 093103 (2009).
- [119] J. Patterson, A. Lagutchev, W. Huang, and D. Dlott, *Phys. Rev. Lett.* **94**, 14 (2005).
- [120] P. Jungwirth and D. J. Tobias, *J. Phys. Chem. B* **106**, 6361 (2002).
- [121] D. Liu, G. Ma, L. M. Levering, and H. C. Allen, *J. Phys. Chem. B* **108**, 2252 (2004).
- [122] M. Koenig, E. Henry, G. Huser, a Benuzzi-Mounaix, B. Faral, E. Martinolli, S. Lepape, T. Vinci, D. Batani, M. Tomasini, B. Telaro, P. Loubeyre, T. Hall, P. Celliers, G. Collins, L. DaSilva, R. Cauble, D. Hicks, D. Bradley, a MacKinnon, P. Patel, J. Eggert,

- J. Pasley, O. Willi, D. Neely, M. Notley, C. Danson, M. Borghesi, L. Romagnani, T. Boehly, and K. Lee, *Nucl. Fusion* **44**, S208 (2004).
- [123] T. Pezeril, G. Saini, D. Veysset, S. Kooi, P. Fidkowski, R. Radovitzky, and K. Nelson, *Phys. Rev. Lett.* **106**, 214503 (2011).
- [124] P. Schiebener, J. Straub, J. Sengers, and J. Gallagher, *J. Phys. Chem. Ref. Data* **19**, 677 (1990).
- [125] Y. Shen, *J. Phys. Chem. C* **116**, 15505 (2012).

Summary

In this thesis, we focus on the structure, structural dynamics, and the energy relaxation of interfacial water molecules at the air/water interface using time-resolved sum-frequency generation (TR-SFG) spectroscopy. Aqueous interfaces exist everywhere and play important roles in our daily life: The gas/water interface covers 70% of our planet; oil on top of water is a common example of liquid/water interface; and solid/water interface like electrodes in electrolytes can be seen in batteries. Insights into the mechanism of the chemical reactions and physical processes at aqueous interfaces can be obtained through studies of the molecular structures and dynamics of these interfaces. Among these interfaces, the air/water interface is one of the simplest aqueous interfaces as well as a model hydrophobic interface.

A noninvasive way of investigating the molecular properties of the air/water interface is to use surface-sensitive vibrational spectroscopy, which selectively probes the net non-zero transition dipole moment along the surface normal, due to symmetry breaking at the interface. Thanks to the high sensitivity of the vibrational frequency to the interactions with the surrounding molecules, the vibrational spectra reflect the local molecular structures in condensed phases. For instance, the water OH stretching mode frequency is lowered with increasing hydrogen bond strength, so that the frequency and lineshape of this mode can be used as a reporter for the microscopic structures around the water molecules. The remaining challenge is then to obtain the vibrational spectrum of specifically those water molecules located at the interface.

The surface-sensitive vibrational spectroscopy we propose here is sum-frequency generation (SFG) spectroscopy. As described in chapter 1, the SFG spectroscopy is an even-order nonlinear spectroscopy, whose selection rules result in the suppression of the signal from isotropic media such as the bulk water. In SFG spectroscopy, an infrared (IR) and a visible (VIS) beam are overlap temporarily and spatially at the interface to generate a signal whose frequency is the sum of the IR and VIS pulse frequencies. If the IR frequency is resonant with the molecular vibrations, the SFG signal will be strongly enhanced, thereby providing the vibrational spectrum of specifically the surface molecules. Thus, the SFG spectra provide us the information on the interfacial water structures, through the central frequencies and linewidths of the vibrational transitions.

The linewidth of the O-H stretch spectra in principle has two contributions: Firstly, quasi-static differences in the local environment of the OH groups can cause inhomogeneous broadening. Secondly, homogeneous broadening effects arise from dynamic, time-dependent changes in the instantaneous vibrational frequency due to several possible processes: structural rearrangements leads to variations in hydrogen bonding strength; anharmonic coupling to thermally excited low frequency modes (such as the hydrogen bond mode); intermolecular dipole-dipole coupling, leading to near-resonant energy transfer, and finally the finite energy lifetime of the vibration contributes to the linewidth. It is not possible to determine the magnitude of these separate contributions to the linewidth using conventional one-dimensional SFG spectroscopy. In contrast, higher-order, time-resolved techniques are capable of distinguishing homogeneous broadening from inhomogeneous broadening. By exciting the interfacial molecules with a resonant IR pump pulse and probe the population decay with the SFG probe signal, we can reveal the lifetimes of these molecular vibrations. The polarization-resolved technique enables us to extract the reorientational motion (i.e. structural dynamics) and vibrational relaxation of water molecules, while the two-dimensional (2D) technique shows the spectral diffusion and the energy coupling between different modes. The experimental setups of these techniques are presented in chapter 2.

In chapter 3 we investigate the reorientational motion of non-hydrogen-bonded ‘free’ (also called ‘dangling’) OH groups that point towards the vapor phase. Vibrational excitation of the dangling OH bonds along a specific polarization axis induces a transient anisotropy of excited OH groups on the surface. The decay of this anisotropy arises from both the reorientation and vibrational relaxation of vibrationally excited free OH groups. By using time- and polarization-resolved SFG spectroscopy with the help of the MD simulation, we found that the in-plane diffusivity is $D_\phi = 0.32 \text{ rad}^2/\text{ps}$, while the out-of-plane diffusivity $D_\theta = 0.36 \text{ rad}^2/\text{ps}$, which is ~ 3 times faster than the H-bonded OH groups in the bulk water. Moreover, in contrast to the bulk, where a jump-like mechanism dictates reorientation, the reorientation dynamics of the interfacial water occurs in a largely diffusive manner. It is also shown that the vibrational relaxation of the free OH groups occurs with a time constant of $\sim 800 \text{ fs}$, which is slower than the H-bonded OH groups in the bulk water.

The mechanism of this vibrational relaxation has been studied in chapter 4. The dissipation of the excess energy of a free OH can be through the reorientation of the free OH into the bulk phase, thereby forming a hydrogen bond (REOR), or through intramolecular energy coupling from the free OH to the hydrogen OH within the same water molecules

(IET). In both cases, the resulting hydrogen-bonded OH groups can release its excess vibrational energy quickly. IR-pump/SFG-probe measurements of both the free OH of H₂O at the air/H₂O interface and of HOD at the air/H₂O:D₂O mixture interface allow us to clarify that REOR contributes to one third of this energy relaxation while two thirds is the result of IET. Two-color time-resolved experiments allow us to determine the timescales of the forward (from free OH to H-bonded OH) and backward (from H-bonded OH to free OH) processes of IET and REOR. These properties typically occur on a ~ 1 ps timescale. In this chapter we also unravel the factors that control the spectral line shape of the free OH groups at the air/water interface.

Interfacial water consists of the dangling OH groups as well as the H-bonded OH groups. The H-bonded OH groups show an infrared spectral response similar to that of bulk water. Although these OH groups exhibit a similar spectral response as in the bulk water, their structure and dynamics are distinctly different. This is demonstrated in chapter 5, where we study the spectral diffusion and vibration relaxation of the H-bonded OH groups of hydrogen-bonded interfacial water molecules using 2D phase-sensitive SFG spectroscopy. The measured 2D spectra reveal that the spectral diffusion of the strongly H-bonded OH groups ($< 3400 \text{ cm}^{-1}$) occurs on a ~ 280 fs time scale, approximately 1.5 times slower than in bulk water. Weakly H-bonded OH groups contributing the spectra at 3500 cm^{-1} (part of which are the hydrogen-bonded parts of the water molecules that have an OH group sticking out) show slower dynamics due to the decoupling of the intra-/intermolecular energy transfer. These results clearly demonstrate that the interruption of the hydrogen bond at the water-vapor interface slows down the water dynamics in contrast with bulk water.

In chapter 6 we employ TR-SFG experiments to survey the propagation of the shock wave generated at the air/water interface into the bulk phase. We study different air/aqueous sodium halide solutions interfaces that exhibit different surface activities of the halide ions. The SFG field radiated away from the air/liquid interface, interferes with the field transmitted into the bulk, which is partially reflected from the IR pump-induced shock wave front. Because the effective path length of the reflected beam increases with time, the interference of the optical responses leads to time-dependent sinusoidal oscillations of the SFG signals, whose periods provide information on the velocity of the propagation of the shock waves in the liquid. Our results show that the acoustic velocities of different sodium halide solutions are similar, although the phase shift of the oscillations are different. The different phase shift

of the oscillation is attributed to originate from the electric-quadrupole and magnetic-dipole contributions of the bulk phase of different sodium halide solutions.

In summary, we survey the dynamics of the interfacial water at the air/water interface. We reveal that the ultrafast vibrational energy transfer dynamics and spectral diffusion of the OH stretch mode at the interface differs from those in the bulk significantly; the rotational motion is 3 times faster than in the bulk and energy relaxation is dominated by the rotational dynamics as well as the vibrational energy transfer from the free OH group to the H-bonded OH groups of a water molecule with the free OH group. These insights can only be obtained by conducting the time-resolved surface-specific spectroscopic studies presented in this thesis.

Samenvatting

In dit proefschrift richten we ons op de structuur, structurele dynamica, en energie-relaxatie van watermoleculen aan het lucht/water-oppervlak met behulp van tijdsopgeloste som-frequentie generatie (TR-SFG) spectroscopie. Grensvlakken met water zijn overal aanwezig en spelen een belangrijke rol in ons dagelijks leven: 70% van onze planeet is bedekt met water, waarbij het water/lucht-grensvlak ontstaat; olie op water is een bekend voorbeeld van een vloeistof/water-oppervlak, en in batterijen is het grensvlak tussen elektroden en elektrolyten een vaste stof/water-oppervlak. Inzichten in de mechanismen van de chemische reacties en fysische processen die plaatsvinden aan deze grensvlakken kunnen worden verkregen door de moleculaire structuur en dynamica van deze grensvlakken te bestuderen. Het lucht/water-oppervlak is een van de eenvoudigste grensvlakken met water en dient als model voor hydrofobe grensvlakken.

Oppervlakte-gevoelige vibratiespectroscopie is een niet-invasieve manier om de moleculaire eigenschappen van het lucht/water-oppervlak te onderzoeken, gebruikmakend van de gebroken symmetrie aan het oppervlak. De vibratiefrequentie van de watermoleculen hangt sterk af van interacties met de omringende moleculen. De vibratie spectra bevatten daarom informatie over de moleculaire structuren in de gecondenseerde fase, en aan het oppervlak. Zo is de frequentie van de water OH strek vibratie lager bij een sterkere waterstofbrug, zodat de frequentie en lijnvorm van deze vibratie kan worden gebruikt om de microscopische structuren rond de watermoleculen op te helderen. De uitdaging is om het vibratiespectrum te meten van specifiek die watermoleculen, die zich op het grensvlak bevinden.

De oppervlakte-gevoelige vibratiespectroscopie die we hier voorstellen is som-frequentie generatie (SFG) spectroscopie. Zoals beschreven in hoofdstuk 1 is SFG spectroscopie een even-orde niet-lineaire spectroscopie, wiens selectieregels leiden tot de onderdrukking van het signaal van isotrope media zoals het bulkwater. Tijdens SFG spectroscopie overlappen een infrarode (IR) en een zichtbare (VIS) laserpulsen in tijd en ruimte op het grensvlak om een signaal te genereren waarvan de frequentie de som van de IR en VIS pulsfrequenties is. Als de IR frequentie resoneert met de moleculaire vibraties zal het SFG signaal versterkt worden, waardoor het vibratiespectrum van specifiek de oppervlakttemoleculen kan worden gemeten. De SFG spectra geven ons dus informatie over

de waterstructuren op het grensvlak, door de centrale frequenties en lijnbreedtes van de vibrationele overgangen.

De lijnbreedte van de O-H stretch spectra heeft in principe twee bijdragen: Ten eerste kunnen quasi-statische verschillen in de lokale omgeving van de OH-groepen inhomogene verbreding veroorzaken. Ten tweede ontstaan uit dynamische tijdsafhankelijke veranderingen in de instantane trillingsfrequentie homogene verbredingseffecten, als gevolg van verschillende processen: structurele herschikkingen leiden tot variaties in de waterstof bindingssterkte; anharmonische koppeling aan thermisch geëxciteerde laagfrequente vibraties (zoals de waterstofbrug vibratie); intermoleculaire dipool-dipool koppeling kan leiden tot energieoverdracht tussen OH groepen met net iets andere frequentie, en tenslotte draagt de eindige energie levensduur van de vibratie bij tot de lijnbreedte. Het is niet mogelijk de omvang van deze afzonderlijke bijdragen aan de lijnbreedte te bepalen met conventionele eendimensionale SFG spectroscopie. Hogere orde, tijdsopgeloste technieken, daarentegen, kunnen homogene verbreding onderscheiden van inhomogene verbreding. Door de grensvlak-moleculen met een resonante IR pomppuls vibrationeel aan te slaan en het populatie verval met het SFG signaal te meten, kunnen we de levensduur van deze moleculaire vibraties onthullen. De polarisatie-opgeloste techniek stelt ons in staat de reoriëntatie (d.w.z. structuurdynamica) en vibrationele relaxatie van watermoleculen af te leiden, terwijl de tweedimensionale (2D) techniek de spectrale diffusie en energie koppeling tussen verschillende moleculen toont. De experimentele opstellingen behorende bij deze technieken worden beschreven in hoofdstuk 2.

In hoofdstuk 3 onderzoeken we de reoriëntatie beweging van niet-waterstof-gebonden 'vrije' (ook wel 'dangling') OH-groepen die wijzen in de richting van de gasfase. Vibrationele excitatie van de vrije OH verbindingen langs een specifieke polarisatie-as veroorzaakt een tijdelijke anisotropie van de verdeling van OH-groepen aan het oppervlak. Het verval van deze anisotropie wordt veroorzaakt door zowel de reoriëntatie alsook vibratie-relaxatie van geëxciteerde vrije OH-groepen. Met behulp van tijds- en polarisatie-opgeloste SFG spectroscopie in combinatie met MD simulaties, hebben we een in-plane diffusiviteit gevonden van $D_\phi = 0.32 \text{ rad}^2/\text{ps}$, terwijl de out-of-plane diffusiviteit $D_\theta = 0.36 \text{ rad}^2/\text{ps}$ bedraagt, hetgeen ~ 3 keer sneller dan de waterstofgebrugde OH-groepen in bulkwater. Bovendien verloopt de reoriëntatie beweging van het oppervlaktewater via een diffusief proces, in tegenstelling tot de bulk, waar reoriëntatie van water moleculen volgens discrete sprongetjes plaatsvindt. Wij tonen ook aan dat de vibratie relaxatie van de vrije OH-groepen

plaatsvindt met een tijdconstante van ~ 800 fs, hetgeen trager is dan de H-gebonden OH-groepen in bulkwater.

Het mechanisme van deze vibrationele relaxatie is onderzocht in hoofdstuk 4. De dissipatie van de overtollige energie van een vrije OH kan plaatsvinden door de reoriëntatie van de vrije OH naar de bulk fase, waardoor een waterstofbrug gevormd wordt (dit proces noemen we ‘REOR’), of via intramoleculaire energie koppeling van de vrije OH naar de waterstof OH binnen hetzelfde watermolecuul (‘IET’). In beide gevallen kunnen de resulterende waterstof-gebonden OH-groepen hun overtollige trillingsenergie snel kwijt. IR-pomp/SFG-probe metingen van zowel de vrije OH van H₂O aan het lucht/ H₂O grensvlak en van HOD aan het lucht/H₂O:D₂O mengsel grensvlak laten zien dat REOR voor 1/3 aan deze energie relaxatie bijdraagt, terwijl 2/3 het gevolg is van IET. Het twee-kleuren tijdsopgeloste experiment geeft ons de mogelijkheid de tijdschalen te bepalen van de voorwaartse (van vrije OH tot H-gebonden OH) en achterwaartse (van H-gebonden OH tot vrije OH) processen van IET en REOR – deze processen vinden alle typisch op ~ 1 ps tijdschaal plaats. In dit hoofdstuk ontrafelen we ook de factoren die de spectrale lijnvorm van de vrije OH-groepen aan het lucht/water-grensvlak bepalen.

Oppervlaktewater bestaat uit vrije OH-groepen en waterstofgebrugde OH-groepen. De waterstofgebrugde OH-groepen aan het oppervlak vertonen een infrarode respons vergelijkbaar met die van bulkwater. Hoewel deze OH-groepen een soortgelijke spectrale respons vertonen als bulkwater, is hun structuur en dynamiek duidelijk verschillend. Dit wordt aangetoond in hoofdstuk 5, waar we de spectrale diffusie en vibratie relaxatie van de waterstofgebrugde OH-groepen van grensvlak-watermoleculen bestuderen met behulp van fasegevoelige 2D-SFG spectroscopie. De gemeten 2D spectra tonen aan dat de spectrale diffusie van de sterk waterstofgebrugde OH-groepen (< 3400 cm⁻¹) gebeurt op een tijdschaal van ~ 280 fs, ongeveer anderhalf keer langzamer dan in bulkwater. Zwak waterstofgebrugde OH-groepen die bijdragen aan de spectra bij 3500 cm⁻¹ (gedeeltelijk veroorzaakt door waterstofgebrugde OH groepen die onderdeel zijn van hetzelfde water molecuul als de vrije OH groep) vertonen een langzamere dynamiek als gevolg van de ontkoppeling van de intra-/intermoleculaire energie overdracht. Deze resultaten tonen duidelijk aan dat de onderbreking van het waterstofbrugnetwerk aan het water-lucht grensvlak de waterdynamiek vertraagt vergeleken met bulk water.

In hoofdstuk 6 gebruiken we TR-SFG experimenten om de voortplanting van de schokgolf, gegenereerd aan het lucht/water-grensvlak, naar de bulk fase te onderzoeken. We

bestuderen grensvlakken van verschillende lucht/waterige natriumhalogenide oplossingen waarbij de halogeen-ionen verschillende oppervlakte-activiteiten vertonen. Het SFG veld dat van het lucht/vloeistof-grensvlak afstraalt richting detector, interfereert daar met het veld dat richting bulk uitgestraald is, maar dat gedeeltelijk wordt gereflecteerd aan het door de IR-pump veroorzaakte schokgolffront. Omdat het schokgolffront propageert, neemt de effectieve weglengte van de gereflecteerde bundel toe met de tijd. Dit leidt tot tijds-afhankelijke interferentie van de SFG signalen (de signalen raken respectievelijk in en uit fase). De periode van de intensiteitsschommelingen verschaffen informatie over de snelheid van de propagatie van de schokgolven in de vloeistof. Onze resultaten tonen aan dat de akoestische snelheden van verschillende natriumhalogenide oplossingen vergelijkbaar zijn, hoewel de faseverschuivingen van de oscillaties verschillend zijn. De verschillende faseverschuiving van de trilling wordt toegeschreven aan de verschillen in de elektrische-quadrupool en magnetische-dipool bijdragen van de bulkfase van verschillende natriumhalogenide oplossingen.

Samengevat hebben wij de dynamiek van oppervlaktewater bij het lucht/water-grensvlak bestudeerd. We laten zien dat de structuurdynamica, de ultrasnelle vibrationele energieoverdracht en spectrale diffusie van de OH strek vibratie aan het oppervlak duidelijk verschilt van die in de bulk; de rotatiebeweging is 3 keer sneller dan in de bulk. De energie relaxatie wordt gedomineerd door de rotatie dynamiek en de trillingsenergie overdracht van de vrije OH-groep naar de H-gebonden OH-groepen van een watermolecuul met een vrije OH-groep. Deze inzichten zijn mogelijk gemaakt door de ontwikkeling van nieuwe tijd-opgeloste oppervlak-specifieke spectroscopische technieken.

Acknowledgement

Thanks to all those who have contributed to this thesis.